



**TECHNISCHE
UNIVERSITÄT
WIEN**

Vienna University of Technology

DISSERTATION

SURFACE DEFECTS AND ADSORPTION ON STRONTIUM RUTHENATES

Ausgeführt zum Zwecke der Erlangung des akademischen Grades eines
Doktors der technischen Wissenschaften unter der Leitung von

Univ.Prof. Dr.techn. Ulrike Diebold

E134

Institut für Angewandte Physik

und mitbetreut von

Ao.Univ.Prof. Dr.techn. Michael Schmid

E134

Institut für Angewandte Physik

eingereicht an der Technischen Universität Wien
Physik

von

Bernhard Stöger

e0526132

Jagdgasse 27/22, 1100 Wien

Wien, November 2014

Acknowledgment

I would like to express my gratitude and appreciation to my supervisor Ulrike Diebold, who supported me during my Ph.D thesis and enabled me to work on such an interesting topic. My four years working in her surface science group has been a fantastic experience. Many thanks also go to my co-workers Michael Schmid, Zhiming Wang, Gareth S. Parkinson, Martin Setvin and Daniel Halwidl and our theoretical collaborators Josef Redinger, Florian Mittendorfer, Marcel Hieckel and Wernfried Mayr-Schmölzer.

In addition, I want to thank my parents, Karoline and Josef, and my wife Maria, who supported me during my entire studies.

Finally, I would like to express my gratitude the Austrian Science Fund for funding my Ph.D thesis (FWF Project No. F45).

Abstract

Complex perovskite oxides are increasingly used in solid oxide fuel cells and catalysis and in devices based on superconductivity, ferroelectricity, magnetoresistance and other properties, which can be tuned by external parameters. In view of these applications, it is highly desirable to better understand the surface properties of perovskite oxides. However, at this point very little is known about their surface properties, due to the difficulty to create a clean, well-defined surface layer. Preferential sputtering, surface segregation and polarity effects often cause surface reconstruction.

This study focuses on Sr_2RuO_4 and $\text{Sr}_3\text{Ru}_2\text{O}_7$, which are the one and the two-layered members of the ruthenate Ruddlesden-Popper series $\text{Sr}_{n+1}\text{Ru}_n\text{O}_{3n+1}$, respectively. We created a well-defined surface SrO surface layer by cleaving the single crystals *in-situ*. My main task was to characterize this as-cleaved surfaces by identifying defects and common adsorbates. Low-temperature scanning tunneling microscopy (STM) shows different point defects at the as-cleaved surface. It had been conjectured previously that these could be oxygen vacancies formed during the cleaving process or during the crystal growth; however, according to density functional theory (DFT) calculations and STM simulations this is not likely. Electron-bombardment of the SrO surface layer revealed that oxygen vacancies can be created artificially and that oxygen vacancies are definitely not present at the as-cleaved surface. Rather we attribute the observed defects to a few bulk impurities and adsorbates from the residual gas.

Exposing Sr_2RuO_4 and $\text{Sr}_3\text{Ru}_2\text{O}_7$ to CO, CO_2 , O_2 and H_2O shows that the SrO surface layer is very reactive. At 78 K CO first populates impurities and then adsorbs above surface O atoms with a binding energy E_{ads} of -0.7 eV. Above 100 K this physisorbed CO replaces the surface O, forming a bent CO_2 with its C end bound to the Ru underneath. The resulting metal carboxylate (Ru-COO) can be desorbed by STM manipulation. A low activation energy ($E_{\text{act}} = 0.17$ eV) and high adsorption energy ($E_{\text{ads}} = -2.2$ eV) confirm a strong reaction between CO and regular surface sites of $\text{Sr}_3\text{Ru}_2\text{O}_7$. CO_2 behaves similar to CO, as it adsorbs also on top of an apical oxygen atom and cannot be removed by annealing to room temperature. Water dissociates on the clean surface forming a surface hydroxyl $\text{O}_s\text{H}_{\text{ads}}$ and an $(\text{OH})_{\text{ads}}$ positioned

on a Sr-Sr bridge. These two hydroxyls still interact with each other and form “dynamic ion pairs”, as the $(\text{OH})_{\text{ads}}$ can move around the $\text{O}_s\text{H}_{\text{ads}}$ from one Sr-Sr bridge site to another. If two water molecules find each other they form a stable aggregate. By adding more water molecules to this aggregate stable water chains can be formed.

Kurzfassung

Im Zuge dieser Dissertation, wurden die Oberflächen von Materialien der Ruddelsden-Popper-Serie $A_{n+1}B_nO_{3n+1}$ untersucht. Hierbei handelt es sich um gemischte Metalloxide. A steht für ein Metall der Seltenen Erden und/oder Erdalkalimetalle, wie Strontium, Calcium oder Lanthan und B steht für ein Übergangsmetall wie Eisen, Titan, oder Ruthenium. In meinen Versuchen habe ich vor allem Sr_2RuO_4 , $Sr_3Ru_2O_7$ und Ca-, Mn- und Co-dotierte Strontiumruthenate mit einem Rastertunnelmikroskop bei 6 K und 78 K untersucht.

Gemischte Metalloxide werden weltweit intensiv erforscht, was einerseits durch ihre außergewöhnlichen physikalischen Eigenschaften, wie der kolossale magnetoresistive Effekt in gemischtvalenten Manganoxiden oder Hochtemperatursupraleitung in den Cupraten erklärt werden kann. Andererseits zeichnen sich Perovskite auch durch ihre chemischen Eigenschaften aus und spielen bereits eine Rolle in der Katalyse und als Kathoden in Festkörperbrennstoffzellen. Nichtsdestoweniger, weiß man noch sehr wenig, wie diese Materialien auf atomarer Ebene mit Adsorbaten wechselwirken und über die Oberflächenchemie dieser Elemente im Allgemeinen.

Während sich durch Standard-Reinigungsverfahren, wie Zerstäubungs/Ausheizzyklen, auf gemischten Metalloxiden komplexe Oberflächenstrukturen ausbilden, ermöglicht das Spalten von Sr_2RuO_4 und $Sr_3Ru_2O_7$ Einkristallen eine wohl-definierte SrO-Oberflächenschicht zu untersuchen. Rastertunnelmikroskaufnahmen zeigen, dass die Oberfläche des frisch gespaltenen Kristalls nicht perfekt ist, sondern verschiedene Defekte enthält. Diese Defekte wurden in einer vorherigen Studie fälschlicherweise als Sr- und O-Fehlstellen charakterisiert, die während des Spaltvorgangs entstehen sollen. Unsere Untersuchungen zeigen jedoch, dass es sich hier um Kristallverunreinigungen und Adsorbate aus dem Restgas handelt.

Um die Oberflächenchemie näher zu untersuchen, setzten wir die SrO Oberfläche von Sr_2RuO_4 und $Sr_3Ru_2O_7$ verschiedenen Molekülen wie CO, CO₂, O₂ und H₂O bei 78 K und 100 K aus. Bei diesen Versuchen stellte sich heraus, dass die Oberfläche von Sr_2RuO_4 und $Sr_3Ru_2O_7$ sehr stark mit adsorbierten CO wechselwirkt. Bei 78 K adsorbiert CO auf der SrO Oberfläche von $Sr_3Ru_2O_7$ auf einem Oberflächensauerstoffatom mit einer

Adsorptionsenergie E_{ads} von -0.7 eV. Wird der Kristall auf 100 K erwärmt, so ersetzt das C Atom das Oberflächensauerstoffatom und ein gebogenes CO_2 wird gebildet, wobei das C-Atom an das Ru-Atom gebunden ist (Ru-Carboxylat). Eine Adsorptionsenergie E_{ads} von -2.2 eV verdeutlicht die starke Bindung zwischen dem CO-Molekül und der Oberfläche von $\text{Sr}_3\text{Ru}_2\text{O}_7$. Im Fall von Sr_2RuO_4 konnte nur die Formation eines Carboxylats beobachtet werden, unabhängig von der Proben temperatur.

Wasser dissoziiert bereits auf der sauberen, defekt-freien Oberfläche zu einem Oberflächenhydroxid $\text{O}_s\text{H}_{\text{ads}}$ und einem adsorbierten Hydroxid $(\text{OH})_{\text{ads}}$. Das $(\text{OH})_{\text{ads}}$ befindet sich auf einer Sr-Sr Brücke und steht immer noch in Wechselwirkung mit dem Oberflächenhydroxid. Dies kann experimentell beobachtet werden, da das $(\text{OH})_{\text{ads}}$ um das $\text{O}_s\text{H}_{\text{ads}}$ von einer Sr-Sr Brückenposition zur nächsten springt. Wird die Mobilität von adsorbiertem Wasser durch Erwärmen der Probe auf Raumtemperatur gesteigert, so können Wassermoleküle miteinander wechselwirken und Dimere oder längere Wasserketten werden gebildet.

Vorläufige Versuche zeigen, dass CO_2 wie CO auf einem O-Atom adsorbiert und bei Raumtemperatur nicht desorbiert.

Contents

1	Introduction	1
1.1	Background	1
1.2	Ruthenate Ruddlesden-Popper Series $\text{Sr}_{n+1}\text{Ru}_n\text{O}_{3n+1}$	6
1.2.1	Sr_2RuO_4	8
1.2.2	$\text{Sr}_3\text{Ru}_2\text{O}_7$	8
2	Experimental Setup and Methods	11
2.1	Ultra-high Vacuum System	11
2.2	Floating-Zone Technique	12
2.3	Sample Preparation - Gluing Procedure	13
2.4	Scanning Tunneling Microscopy (STM)	15
2.4.1	Basics	15
2.4.2	Tersoff-Hamann Model	16
2.4.3	FT-STs	17
2.4.4	Tip-induced Manipulation	19
3	Surface Defects of Sr_2RuO_4 and $\text{Sr}_3\text{Ru}_2\text{O}_7$	23
3.1	Introduction	23
3.2	Cleaving Planes and Surface Layer	25
3.3	STM Images of the Clean Surface	27
3.3.1	$\text{Sr}_3\text{Ru}_2\text{O}_7$	27
3.3.2	Sr_2RuO_4	31
3.4	Intentionally Doped Samples	32
3.4.1	$(\text{Sr}_{0.95}\text{Ca}_{0.05})_3\text{Ru}_2\text{O}_7$	33
3.4.2	$\text{Sr}_2\text{Ru}_{0.97}\text{B}_{0.03}\text{O}_4$, (B=Mn,Co)	33
3.5	Oxygen Vacancies	34

3.6	Influence of the Cleaving Temperature	36
3.7	Domain Boundaries	37
3.8	Unidentified Structures	38
3.8.1	Line Defects, Dark Depressions and Bright Hills	38
3.8.2	“Sponge”-Structure	40
3.9	Conclusion	40
4	Adsorption of CO	43
4.1	Introduction	43
4.2	Initial Adsorption	44
4.3	Precursor	45
4.4	Carboxylate	46
4.5	Transition: Precursor - Carboxylate	48
4.6	Reaction V_O - CO_2	48
4.7	From single molecules to a full monolayer	50
4.7.1	Sticking Coefficient	50
4.7.2	Saturation Coverage of CO	52
4.8	Interaction with defects	54
4.9	Interaction with water	54
4.10	Tip-induced Desorption	55
4.10.1	CO - Low Coverage	55
4.10.2	Desorption of CO at High Coverage	59
4.11	Conclusion	59
5	Adsorption of H_2O	61
5.1	Introduction	61
5.2	Monomers	64
5.3	Dimers	65
5.4	Multimers	67
5.5	Higher coverage	69
5.6	Desorption	70
5.6.1	Annealing	70
5.6.2	Tip Manipulation	71
5.6.3	Electron Bombardment	71
5.7	Water Dissociation at V_{Os}	72

5.8	Conclusion	72
6	FT-STs measurements on Sr_2RuO_4	77
7	Preliminary Results	83
7.1	Adsorption of O_2	83
7.2	Adsorption of CO_2	84
8	Summary and Outlook	87
8.1	Sample Preparation	88
8.2	As-cleaved surfaces	89
8.3	Adsorption of CO	89
8.4	Adsorption of H_2O	90
8.5	FT-STs measurements on Sr_2RuO_4	90
A	List of all STM images	93

Chapter 1

Introduction

1.1 Background

Perovskite oxide materials, with the chemical formula ABO_3 , exhibit a wide range of distinct electronic and magnetic properties, including unconventional superconductivity, Mott insulating state, itinerant magnetism and colossal magnetoresistance. Due to a strong coupling between charge, spin, lattice and orbital degrees of freedom [1], these properties can often be tuned via non-thermal parameters such as magnetic fields, pressure or chemical doping.

The ideal perovskite structure is cubic (space group $Pm\bar{3}m$) and consist of octahedrally coordinated B-site cations, where B represents a transition metal (Mn, Ti, Ru, etc.). Each corner-shared BO_6 oxygen octahedron is surrounded by eight A atoms, where A represents a rare/or alkaline earth metal (La, Sr, Ca, etc.). Only a few perovskites adopt this ideal structure, often small distortions of the crystal lattice reduce the symmetry of the system. These distortions are caused by rotation of the BO_6 octahedra [see Fig. 1.1(a)], changes of the B-O distances due to Jahn-Teller distortions [2] [see Fig. 1.1(b)], or displacement of the B atom the inside the octahedron from its central position [see Fig. 1.1(c)].

The symmetry of rotations and tilts can be described by the Glazer notation [5] ($a^\#b^\#c^\#$) [see Fig. 1.1(d)], where a, b and c represent the rotation about each cubic axis and the subscript (0) indicates no, (+) in-phase and (-) out-of-phase rotation of neighboring octahedra. In the general case of unequal rotations, the rotations are denoted (abc). If two rotations are equal,

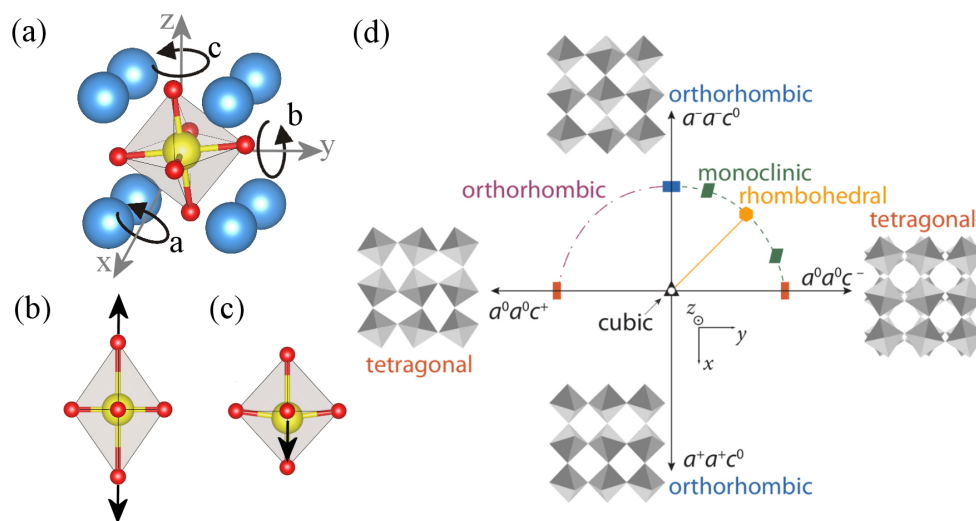


Figure 1.1: Octahedra distortions in a perovskite unit cell. (a) Three different rotations about the three cubic axis, x, y, z are possible. (b) Elongation of the octahedron due to a Jahn-Teller distortion. (c) B-misplacement inside the octahedron. (d) Rotations can be described by the Glazer notation ($a^\#b^\#c^\#$), where a, b and c represent the rotation about each cubic-axis and the subscript (0) indicates no, (+) in-phase and (-) out-of-phase rotation of neighboring octahedra. If two rotations are the same, an appropriate letter is repeated (aac). Color code: A (blue), B (yellow) and O (red). (a) based on Rondinelli *et al.* [3]. (b,c) based on He *et al.* [4] (d) Figure reprinted with permission from [“Structure and Properties of Functional Oxide Thin Films: Insights From Electronic-Structure Calculations”, Rondinelli *et al.*, *Advanced Materials*, **23**, 3363, (2011)], [3]. Copyright © 2014 by John Wiley & Sons.

an appropriate letter is repeated as in (aac). The one-tilt systems $a^0a^0c^+$ and $a^0a^0c^-$ are only rotated about the cubic z axis, where two neighboring octahedra along the z axis rotate in the same direction and opposite direction for $a^0a^0c^+$ and $a^0a^0c^-$ respectively. $a^+a^+c^0$ and $a^-a^-c^0$ systems are not rotated about the z axis but are rotated about the same angle about the x and y axes. Tilts and rotations of the BO_6 oxygen octahedra are usually influenced by steric, size effects such as the Goldschmidt tolerance factor τ , which is a measure how well the A-site cation fits into the cubic corner-sharing octahedral network [6]:

$$\tau = \frac{r_A + r_O}{\sqrt{2}(r_B + r_O)}, \quad (1.1)$$

where r_A , r_B and r_O are the atomic radii for the A cations, B cations and O anions, respectively. In the case of SrRuO_3 the ionic radii for Sr, Ru and O are 1.44, 0.62 and 1.40 Å [7], respectively, which yields a tolerance factor of $\tau = 0.99$, close to the ideal cubic perovskite structure $\tau = 1$. In the case of $\tau < 1$, the A cation atoms are too small, which can induce tilting and rotation of the octahedra. In the case of $\tau > 1$, the A cation atoms are too large and near-hexagonal close-packed layers of A cations and O anions can form, as in BaNiO_3 [8].

In addition to these octahedral tilts and rotations, distortions can also be electronically driven. Due to the crystal field of the six oxygen anions surrounding the B cation, the d -orbitals split into three t_{2g} orbitals (d_{xy} , d_{xz} , d_{yz}) and two e_g orbitals (d_{z^2} , $d_{x^2-y^2}$). If the e_g orbitals are partially filled, a Jahn-Teller lattice distortion can remove the degeneracy of the orbital. If two B-O bonds lengthen and two contract, the geometry of a regular octahedron becomes orthorhombic and if two bonds lengthen and the remaining four contract, or vice versa, the point symmetry becomes tetragonal [9]. Often, perovskites show rotational distortions as well as Jahn-Teller distortions, which do not have to be independent and can influence each other [10].

A common way to tune the physical properties of perovskite oxides is doping. If A atoms are replaced by non-isovalent cations, electrons or holes are introduced into the band at the Fermi energy. If A atoms are replaced by isovalent cations, changes in the electronic and magnetic properties are mainly caused by a modification of the crystal structure. Cations of different

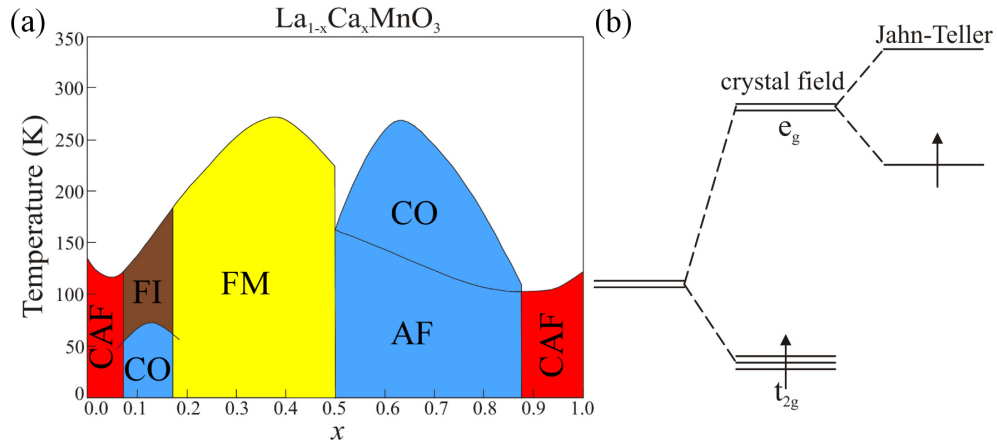


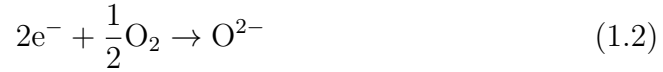
Figure 1.2: $\text{La}_{1-x}\text{Ca}_x\text{MnO}_3$. (a) Phase diagram of $\text{La}_{1-x}\text{Ca}_x\text{MnO}_3$. The physical properties depend on the doping level. Canted ferromagnet (CAF), ferromagnetic insulator (FI), charge ordered state (CO), ferromagnet metal (FM), antiferromagnet (AF). (b) Splitting of the d orbital into three t_{2g} and two e_g orbitals. Due to the Jahn-Teller effect the degeneracy of the e_g orbitals is lifted. (a,b) Figures reprinted with permission from [“Lattice effects in magnetoresistive manganese perovskites”, Millis, *Nature*, **392**, 147, (1998)], [11]. Copyright © 2014 by Nature Publishing Group.

size induce internal stress that leads to a distortion of the BO_6 octahedra (rotation, tilt, B-O bond length). For example, the influence of non-isovalent doping on $\text{La}_{1-x}\text{Ca}_x\text{MnO}_3$ is shown in the phase diagram, Fig. 1.2(a) [11], where the ground state depends on the doping concentration x , ranging from a canted ferromagnet (CAF), over a ferromagnetic insulator (FI), charge ordered states (CO), ferromagnet metal (FM), antiferromagnet (AF) to a canted antiferromagnet once again. In some members of the manganite series $\text{La}_{1-x}\text{Ca}_x\text{MnO}_3$, lattice-spin coupling can be observed. Due to the doping, a fraction x of the Mn atoms is tetravalent Mn^{4+} and $1-x$ is trivalent Mn^{3+} , with a partially filled e_g orbital. Thus, Mn^{3+} is Jahn-Teller active and in addition to the distortion due to the dopant size, two uniaxial volume-preserving distortions (Jahn-Teller distortions) couple to a preferential occupancy of one e_g orbital over the other [11] [see Fig. 1.2(b)].

Strain can not only be induced by dopants, but strain also shows up at interfaces between different perovskite layers, due to a (small) lattice mismatch [3]. In the case of SrRuO_3 it was theoretically shown that local magnetic properties are affected by strain causing octahedral distortions [4]. SrRuO_3 is a nearly half-metallic oxide with minority spin densities at the

Fermi level and majority spin densities just below the Fermi level. Small changes in the Ru-O bond length, tilts and rotations can easily affect the hybridization between Ru d and oxygen p orbitals, which influences the spin configurations.

Due to the wide variety of physical properties that can be tuned by external parameters, perovskite oxides are fascinating materials for condensed matter physics research. From a chemistry point of view perovskite oxides are equally interesting and the possibility to use them as catalysts and as cathodes in solid oxide fuel cells (SOFC) is heavily investigated. For applications, perovskites are considered as cathodes for SOFCs, where oxygen atoms adsorb and get reduced to oxygen ions in the half-cell reaction:



The O^{2-} ions travel through the electrolyte (often yttria-stabilized zirconia) to the anode, where they react with H_2 in the second half-cell reaction to H_2O .



Considering these applications a deep understanding of the surface properties and adsorption behavior on the clean and defective surface is of great importance. However, at this point very little is known about the exact adsorption behavior on clean and defective perovskite surfaces, caused by the difficulty to prepare a well-defined surface, as for $SrRuO_3$. Owing to the volatility of higher ruthenium oxides, $SrRuO_3$ films grow on $SrTiO_3$ with a SrO termination. STM images reveal that, depending on the preparation conditions, different surface reconstructions form [see Fig. 1.3(a,b)]. To gain more insight into the physics behind solid oxide fuel cells and catalytic processes experiments on a well-defined surface layer are essential. To create such well-defined surface layers we cleaved perovskite-like crystals *in-situ*, inside an UHV chamber and investigated the resulting surface with low-temperature scanning tunneling microscopy (LT-STM).

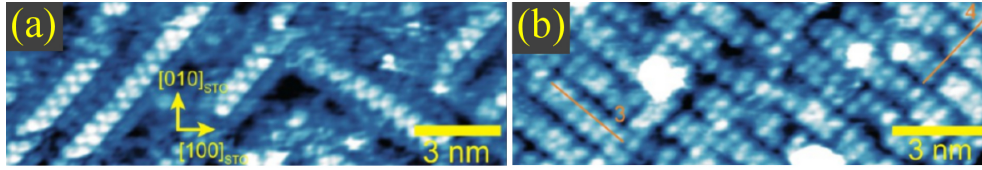


Figure 1.3: STM images of SrRuO₃. (a,b) Thin films of SrRuO₃ grown SrTiO₃(001). Different surface reconstructions can be observed, depending on the sample preparation conditions. (a,b) Figures reprinted with permission from [“Oxygen Control of Atomic Structure and Physical Properties of SrRuO₃ Surfaces”, Tselev *et al.*, ACS Nano, **7**, 4403, (2013)], [12]. Copyright © 2014 by American Chemical Society.

1.2 Ruthenate Ruddlesden-Popper series



Ideal perovskites with the structure ABO₃ cannot be cleaved easily, and to my knowledge, no atomic resolution images of cleaved perovskites exist. In our studies, we cleaved Sr₂RuO₄ and Sr₃Ru₂O₇ single crystals, which are the $n = 1$ and $n = 2$ layered members of the n -layered ruthenate Ruddlesden-Popper series Sr _{$n+1$} Ru _{n} O _{$3n+1$} , respectively. Materials of this series consist of n perovskite layers separated by an additional rock-salt structure [see Fig. 1.4]. Due to the layered structure these materials cleave easily along the [001] direction between two SrO layers. Both materials are metallic and serve as prototype perovskite oxides, where the adsorption behavior of several molecules and the influence of defects can be probed by scanning tunneling microscopy at any sample bias voltage.

The crystal structures of Sr₂RuO₄, Sr₃Ru₂O₇, Sr₄Ru₃O₁₀ and SrRuO₃ show distinct differences [see Fig. 1.4]. While the octahedra in Sr₂RuO₄ are not distorted, they are rotated in Sr₃Ru₂O₇ and Sr₄Ru₃O₁₀, and even rotated and tilted in the perovskite structure SrRuO₃. These different arrangements of the RuO₆ octahedra go along with different properties, as the Sr _{$n+1$} Ru _{n} O _{$3n+1$} series ranges from a spin-triplet superconductor ($n = 1$, Sr₂RuO₄) [17, 18] over an itinerant metamagnetic state with a field-tuned nematic phase ($n=2$, Sr₃Ru₂O₇) [19–21], to an itinerant ferromagnet ($n = \infty$, SrRuO₃) [22, 23].

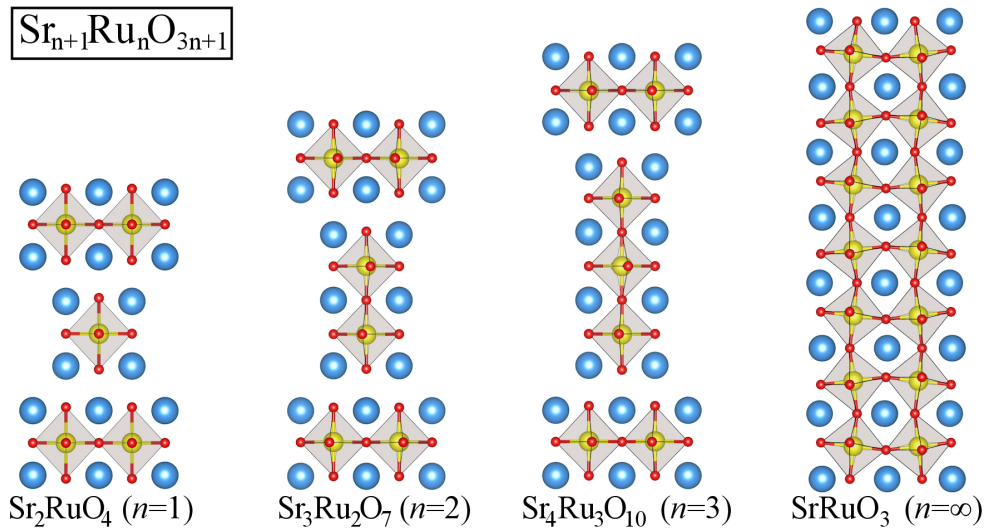


Figure 1.4: Ruthenate Ruddlesden-Popper series $Sr_{n+1}Ru_nO_{3n+1}$. Members of the ruthenate Ruddlesden-Popper series consist of n perovskite layers $SrRuO_3$ separated by two layers of SrO . The crystal structures of Sr_2RuO_4 , $Sr_3Ru_2O_7$, $Sr_4Ru_3O_{10}$ and $SrRuO_3$ show different lattice distortions. The octahedra are not rotated for the $n = 1$ member. In the case of the $n = 2$ and $n = 3$ member, the octahedra are rotated, but not tilted. The octahedra of the perovskite structure, $n = \infty$, are rotated and tilted. Color code: Sr (blue), Ru (yellow) and O (red). The crystals structures were constructed using data from [13–16]. Sr_2RuO_4 ($I4/m\bar{m}$, $a = 3.87 \text{ \AA}$, room temperature), $Sr_3Ru_2O_7$ (BBcb, $a = 5.497 \text{ \AA}$, $b = 5.5008 \text{ \AA}$, room temperature).

1.2.1 Sr_2RuO_4

The single-layered strontium ruthenate Sr_2RuO_4 is the first layered perovskite without CuO_2 planes, which was found to exhibit superconductivity [17, 18]. While most superconductors are conventional (s -wave) superconductors, Sr_2RuO_4 is an unconventional (p -wave) superconductor [18]. Superconductivity involves pairing of conduction electrons and the formation of a Bose-Einstein condensate (Cooper pair). The pair of electrons can either have a total spin of $S = 0$ or $S = 1$. The $S = 0$ anti-symmetric spin-singlet state can be described by a symmetric orbital wave function with angular momentum $L = 0$ (s wave), $L = 2$ (d wave), etc. In the case of $S = 1$ the symmetric spin-triplet state is described by an anti-symmetric orbital wave function with $L = 1$ (p wave), $L = 3$ (f wave), etc. [18].

The electrical resistivity ρ_c follows a metallic temperature dependence below 130 K and a T^2 dependence [18] below 20 K. The in-plane resistivity ρ_{ab} shows metallic behavior below 300 K and a T^2 dependence at low temperatures, characteristic of a Fermi liquid behavior [18]. The ratio ρ_c/ρ_{ab} varies between 400 and 4000 at low temperatures, i. e. a strongly anisotropic behavior [18].

The electronic band structure of Sr_2RuO_4 near the Fermi level is dictated by the Ru $4d$ orbitals [24]. Due to hybridization of the d_{xz} and d_{yz} orbitals a hole-like Fermi surface sheet (α) is formed near X and an electron-like band (β) around Γ [see Fig. 1.5(a,b)]. The d_{xy} orbital leads to an electron-like surface sheet (γ) around Γ . In addition to the bulk bands, angle-resolved photoemission spectroscopy (ARPES) measurements also show surface bands [24], which are caused by a surface reconstruction. In cleaved Sr_2RuO_4 single crystals, the octahedra of the surface layer start to rotate alternately clockwise and counterclockwise forming a $c(2 \times 2)$ surface reconstruction [25, 26].

1.2.2 $\text{Sr}_3\text{Ru}_2\text{O}_7$

The two-layered strontium ruthenate $\text{Sr}_3\text{Ru}_2\text{O}_7$ was first described by a tetragonal space group ($I4/mmm$) [27]. However later studies revealed that the RuO_6 octahedra of $\text{Sr}_3\text{Ru}_2\text{O}_7$ are rotated and that the crystal has to be described by an orthorhombic space group (Pbn [28], BBcb [14]). As the surface layer is just slightly more distorted, see Ref. [29], the surface has in

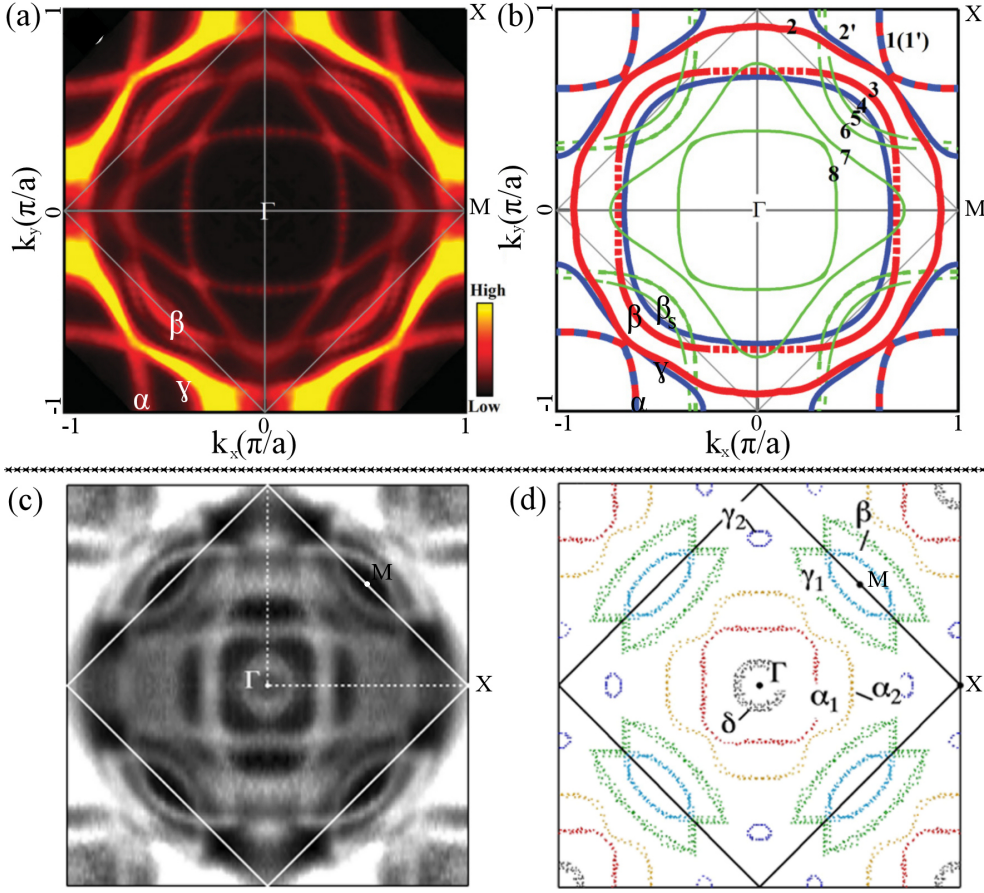


Figure 1.5: Fermi surfaces of Sr_2RuO_4 and $Sr_3Ru_2O_7$. (a–d) ARPES measurements of Sr_2RuO_4 and $Sr_3Ru_2O_7$. (a,b) Due to the surface $c(2 \times 2)$ reconstruction not only the bulk Fermi surface [marked red, in frame (b)], but also the surface Fermi surface [blue in frame (b)] are observed. The green surface sheets are the umklapp Fermi surface sheets, due to the $c(2 \times 2)$ reconstruction. The band structure is dominated by the Ru 4d orbitals. Sr_2RuO_4 Fermi surface: The Fermi surface sheets α and β are formed by a hybridization of the d_{xz} and d_{yz} orbitals. The γ surface sheet is created by the d_{xy} orbital. (c,d) The band structure is also dominated by the Ru 4d orbitals. $Sr_3Ru_2O_7$ Fermi surface: The δ surface sheet is formed by the $d_{x^2-y^2}$ orbital, α by the d_{xz} and d_{yz} orbitals and β and γ are formed by mixing of $d_{xz,yz}$ and d_{xy} orbitals. (a,b) Figures reprinted with permission from [“Fermi surface sheet-dependent band splitting in Sr_2RuO_4 revealed by high-resolution angle-resolved photoemission spectroscopy”, Liu *et al.*, Phys. Rev. B, **86**, 165112, (2012)], [24]. (c,d) Figures reprinted with permission from [“Fermi Surface and van Hove Singularities in the Itinerant Metamagnet $Sr_3Ru_2O_7$ ”, Tamai *et al.*, Phys. Rev. Lett., **101**, 026407, (2008)], [19]. Copyright © 2014 by American Physical Society.

principle the same symmetry as the bulk truncation. However, it is standard notation to use the tetragonal unit cell, where the octahedra are not rotated as the (1×1) unit cell and the primitive unit cell of $\text{Sr}_3\text{Ru}_2\text{O}_7$ is referred to as a $c(2 \times 2)$ structure.

$\text{Sr}_3\text{Ru}_2\text{O}_7$ is a (nearly ferromagnetic) paramagnet, whose ground state can be driven under hydrostatic pressure of 1.1 GPa from paramagnetism to ferromagnetism below 70 K [20]. A superlinear rise of magnetization in a field of approximately 5.5 T indicates the occurrence of metamagnetism [30].

The electrical resistivities ρ_{ab} and ρ_c are metallic and yield a quadratic temperature dependence below 6 K, characteristic for a Fermi liquid behavior [20]. The ratio ρ_c/ρ_{ab} show a strong anisotropic behavior, as it is about 300 at 0.3 K and 40 at 300 K [20]. As for Sr_2RuO_4 the electronic band structure is dictated by the Ru $4d$ orbitals [19] [see Fig. 1.5(c.d)]. The electron-like innermost Fermi surface sheet δ , centered around the Γ point, corresponds to the $d_{x^2-y^2}$ orbital, which is unoccupied in Sr_2RuO_4 . The hole-like α surface sheets correspond to the d_{xz} and d_{yz} orbitals. The β and γ surface sheets found around the M point form by mixing of $d_{xz,yz}$ and d_{xy} orbitals.

Chapter 2

Experimental Setup and Methods

2.1 Ultra-high Vacuum System

The ultra-high vacuum (UHV) system where all scanning tunneling microscopy (STM) measurements were conducted consists of an analysis chamber, a preparation chamber, and a load lock. The analysis chamber is equipped with a commercial Omicron low-temperature STM (LT-STM), which can be operated at 6 K, 78 K or room temperature. All STM data shown in this thesis were either taken at 6 K or 78 K. The analysis chamber is pumped with an ion pump and a titanium sublimation pump to achieve a base pressure of 5×10^{-12} mbar. The pressure is determined by an ion gauge. The preparation chamber is equipped with a raster sputter gun (SPECS IQE 12/38) and a heating stage that can be used for cleaning samples (not used for our samples - see below) and STM tips. In addition, samples can be bombarded with electrons and photons using a rastered electron gun (SPECS EQ22/35) and an X-ray source, respectively. With the help of a hemispherical electron energy analyzer (SPECS EA 10 Plus) these two guns can be used for Auger electron spectroscopy and X-Ray photoelectron spectroscopy, respectively. The surface properties can also be investigated with Low Energy Electron Diffraction (LEED). The preparation chamber is pumped with an ion pump, a titanium sublimation pump, a turbomolecular and a rotary pump. Usually, the gate valve between the preparation chamber and the turbomolecular and

rotary pump was closed to lower the pressure of the preparation chamber from 2×10^{-10} mbar to a base pressure of 5×10^{-11} mbar. The gas pressure is determined by an ion gauge and the composition of the residual gas can be checked with a mass spectrometer (BALZERS QMG 125). A coolable manipulator (down to 100 K) is used to transfer samples from the preparation chamber into the analysis chamber. Each chamber is also equipped with a wobble stick to move samples inside the chambers. The preparation chamber is separated by a gate valve from the loadlock. After inserting new samples or tips into the loadlock, it has to be baked for at least 5 hours and cooled down for 2 hours to preserve a low pressure in the preparation chamber during transfer. New samples or tips are transferred to the preparation chamber via a magnetic transfer rod. The STM chamber as well as the preparation chamber are equipped with leak valves to dose controlled amounts of CO, CO₂, H₂O and O₂ into the chamber. In the preparation chamber, it is possible to dose molecules via a directional doser, which can be brought very close to the sample, using a linear motion. When the directional doser is used, the pressure at the sample is enhanced by a factor of 10-20 compared to the pressure read by the ion gauge.

2.2 Floating-Zone Technique

All Sr₂RuO₄ and Sr₃Ru₂O₇ samples that were investigated in this thesis were grown by our collaborator Prof. Mao and his students at Tulane University, New Orleans, LA. A two-mirror optical floating-zone furnace was used to grow high-quality perovskite single crystals. This technique is explained in detail in Ref. [31], which is also the basis for the following description.

This method is based on melting (via infrared irradiation) the bottom part of a feed rod that is held from the top, and connecting the molten zone to a seed rod held from the bottom. SrCO₃ and RuO₂ are the starting material for the feed rods. The two starting materials are ground in agate mortar and then pressed into disk-shaped pellets. Afterwards the pellets are heated at 1150°C in air and reground into powder. The powder is then filled into a rubber balloon and compressed under water to a rod. Finally, the rod is sintered at 1420°C.

For the seed material either a polycrystal or single crystal can be used. If a single crystal is used, the grown crystal will have the same crystalline orientation as the seed. The molten end of the feed rod is brought close to the seed rod so that the new crystal can grow on the seed rod. At all times, the feed rod and seed rod are rotated in the opposite direction, to ensure efficient intermixing in the molten zone and a homogeneous heating environment around the seed rod. Due to higher evaporation of RuO_2 from the melt at 2200°C , the ratios of $2\text{N}(\text{Ru})/\text{N}(\text{Sr})$ for Sr_2RuO_4 and $3\text{N}(\text{Ru})/2\text{N}(\text{Sr})$ for $\text{Sr}_3\text{Ru}_2\text{O}_7$ have to be larger than unity. The speed at which the crystals are grown also severely affect the crystal properties, as lower growth speeds usually lead to greater RuO_2 evaporation and a Ru deficiency. If the ratio and all growth parameters, such as the ratio between $\text{N}(\text{Ru})$ and $\text{N}(\text{Sr})$, the growth atmosphere, growth speed and rotation speed are not adjusted well it can easily happen that other members of the $\text{Sr}_{n+1}\text{Ru}_n\text{O}_{3n+1}$ family, or Ru microdomains, get incorporated in the grown crystal. A summary on how different parameters affect the quality of crystals grown by the floating zone technique is given in Ref. [32]. Sr_2RuO_4 single crystals grown with this technique can be as large as $\sim 80 \times 4 \times 3 \text{ mm}^3$, where the 3 mm distance is measured along the crystallographic [001] direction. The largest pieces of such a rod, which we investigated with STM, were about $\sim 4 \times 3 \times 2 \text{ mm}^3$. The size of our Sr_2RuO_4 and $\text{Sr}_3\text{Ru}_2\text{O}_7$ samples is mainly restricted by the size of the grown crystal rod and by the fact that samples can cleave during transportation.

In total ~ 30 $\text{Sr}_3\text{Ru}_2\text{O}_7$ single crystals from three different sample batches and Sr_2RuO_4 , $(\text{Sr}_{0.95}\text{Ca}_{0.05})_3\text{Ru}_2\text{O}_7$, $\text{Sr}_2\text{Ru}_{0.97}\text{Mn}_{0.03}\text{O}_4$ and $\text{Sr}_2\text{Ru}_{0.97}\text{Co}_{0.03}\text{O}_4$ single crystals from one sample batch each were investigated. The $\text{Sr}_3\text{Ru}_2\text{O}_7$ samples from batch #1 are numbered sample 1-4, samples from batch #2 are numbered sample 5-9, and samples from batch #3 sample 10-15.

2.3 Sample Preparation - Gluing Procedure

As discussed above [see Section 1.2], Sr_2RuO_4 and $\text{Sr}_3\text{Ru}_2\text{O}_7$ cleave easily along the [001] direction due to their layered structure. To prepare the single

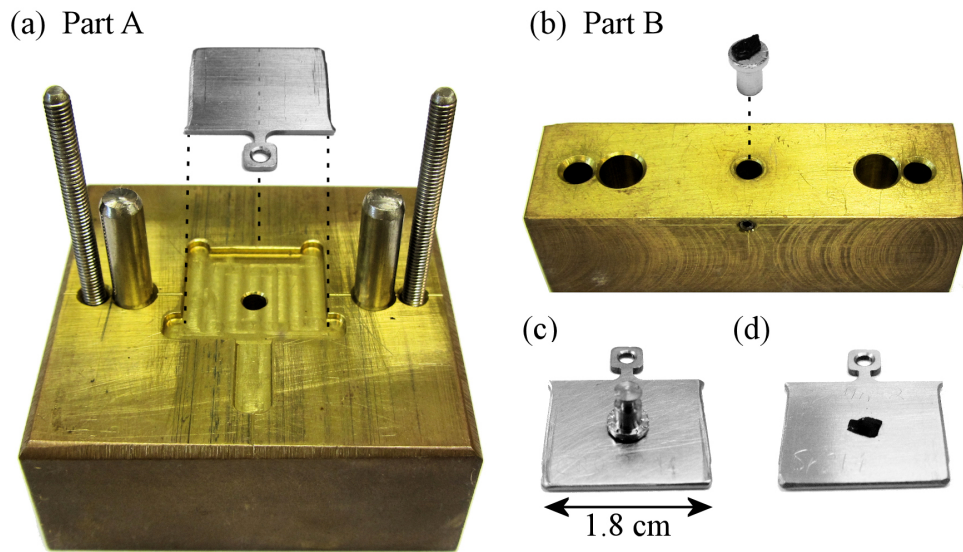


Figure 2.1: Gluing gadget. The gadget consists of part A (a) and part B (b). (c) Prepared sample: The sample is glued between the sample plate and the top metal stub. (d) Cleaved sample: The surface layer can be investigated by STM. The gluing gadget was constructed by Manfred Menhard [33].

crystals for cleaving, the single crystals were fixed on stainless steel sample plates using conducting silver epoxy glue (EPO-TEK H21D), and a metal stub was glued on top with another epoxy adhesive (EPO-TEK H77). We designed a gluing gadget that consists of two parts [see Fig. 2.1]. On part A an area is milled out, where a sample plate is put in. On part B the cleaving stub can be put in a hole and fixed with a screw, to prevent it from falling out when part B is tilted.

The best way to mount the sample is to put the cleaving stub into part B first. Afterwards, the cleaving stub is covered with a thin film of the non-conducting glue. Next, the single crystal is placed on the cleaving stub and a thin film of the conducting silver epoxy is put on top of the single crystal. Then the gadget part B with the cleaving stub is flipped by 180° and put onto part A, where a stainless steel sample plate rests in the cavity. It is very important that only small amounts of glue is used. Otherwise it can easily happen that the metal stub and the sample plate are glued together, which makes the cleaving more difficult or even impossible. Also possible “glue dust” on the sample, caused by the breaking of the glue, has to be avoided. After fixing part B on Part A with the two butterfly screws, the gadget is covered in aluminum foil and baked in an oven at 150°C for 1.5

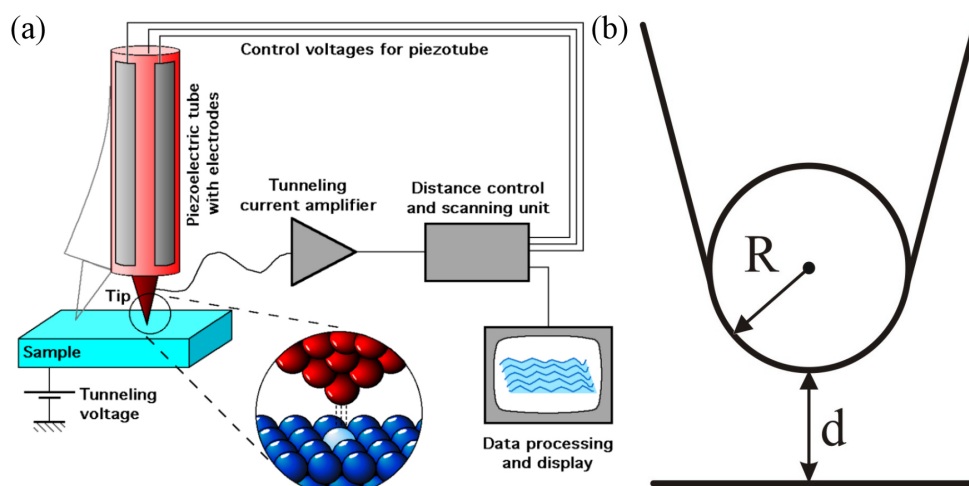


Figure 2.2: STM basics. (a) Schematic drawing of a Scanning Tunneling Microscope. (b) Tip/sample geometry in the Tersoff-Hamann Model. Figure (a) was designed by Michael Schmid, TU Wien.

hours if the oven is already hot, and for 2 hours if the oven is cold. Healing reduces significantly the hardening time of the glue.

After inserting the freshly prepared sample into the UHV system, the metal stub can be grabbed with the wobble stick and the sample can be cleaved by applying a small force to the metal stub. If the metal stub and the sample plate are not glued together, the crystal cleaves easily just by touching the metal stub. To avoid damaging the manipulator, samples, which do not cleave easily have to be cleaved in the tip carousel. However, uncontrolled movements of wobble stick have to be avoided, as the bellows of the wobble stick can easily get damaged. Thus, cleaving at any cost has to be avoided.

2.4 Scanning Tunneling Microscopy (STM)

2.4.1 Basics

In the early 1980s Binnig and Rohrer invented Scanning Tunneling Microscopy, a powerful tool to investigate surface properties of metals and semiconductors at the atomic scale. The physical basis of STM is the quantum mechanical tunneling effect of electrons through a vacuum gap.

In experiment [see Fig. 2.2(a)], a bias voltage $U_s = \pm 0.002\text{--}1\text{ V}$ is applied between the sample and a sharp tungsten tip. The tip is brought close (few Å)

to the surface, using piezoelectric elements, until a tunneling current between the tip and sample can be measured. The tip is mounted on a piezoelectric tube and by applying a voltage to the electrodes the tip can be rastered across the surface. In our experiment, the STM was operated most of the time in the constant current mode, meaning that the tunneling current is kept constant by varying the z -position of the tip. The adjusted signal of the z piezo element is recorded and transformed into an image.

To gain a basic idea of the tunneling current a simple model can be investigated, where electrons are described by wave functions $\psi(z)$, which satisfy the 1D Schrödinger equation with a rectangular potential given by $U(z)$:

$$\left(\frac{-\hbar^2}{2m}\Delta + U(z)\right)\psi(z) = E\psi(z), \quad (2.1)$$

Inside the vacuum gap ($E < |U|$), the solution for the 1D Schrödinger equation is a decaying electron wave function:

$$\psi(z) \propto e^{-z\kappa}, \kappa = \frac{\sqrt{2m(U - E)}}{\hbar}, \quad (2.2)$$

and the tunneling current (I_t) is proportional to the probability (T) for electrons tunneling through the vacuum barrier (width d):

$$I_t \propto T \propto |\psi(d)|^2 \propto e^{-2d\kappa} \quad (2.3)$$

Given the exponential relationship between the tunneling current and the sample-tip distance, small changes in the sample-tip distance can have a huge effect on the tunneling current. This way, changes of the distance in the sub-Å range can be detected.

2.4.2 Tersoff-Hamann Model

A more complex way of describing electron tunneling comes from the Tersoff-Hamann approach [34, 35], which is based on the Bardeen approach [36], making use of the time dependent perturbation theory. In this model the end

of the tip is spherical with a radius R and the distance to the sample is d [see Fig. 2.2(b)]. The tip is modeled as an s wave function and the surface is described by Bloch waves.

An electron can tunnel between the states ψ_μ and ψ_ν of the sample with a probability (w) given by Fermi's Golden Rule:

$$w = \frac{2\pi}{\hbar} |M_{\mu\nu}|^2 \delta(E_\mu - E_\nu), \quad (2.4)$$

where $M_{\mu\nu}$ is the tunneling matrix element and the delta function restricts tunneling to occur only between electron levels with the same energy. The transmission matrix is given by an overlap of the tip and surface states:

$$|M_{\mu\nu}|^2 = \frac{\hbar^2}{2m} \int d\vec{S} (\psi_\mu^* \nabla \psi_\nu - \psi_\nu \nabla \psi_\mu^*), \quad (2.5)$$

When applying a bias voltage U , the tunneling current can be written as:

$$I = \frac{2\pi e}{\hbar} \sum_{\mu,\nu} f(E_\mu) [1 - f(E_\nu + eU)] |M_{\mu\nu}|^2 \delta(E_\mu - E_\nu). \quad (2.6)$$

In a rough approximation the tunneling current can be written as:

$$I \propto \int_{E_F}^{E_F + eU} \rho_T(E - eU) \rho_S(E) T(E, U) dE, \quad (2.7)$$

where $\rho_T(E)$ is the density of states associated with the tip atom, $\rho_S(E)$ is the local density of states of the sample at the position of the STM tip, and $T(E, U)$ the transmission probability. Assuming a constant tip density of states ρ_T and a smooth transmission probability T , dI/dV curves give direct information about the LDOS of the surface states:

$$\frac{dI}{dV} \Big|_{E=E_F+eU} \propto \rho_S(E_F + eU) T(E, U) \Big|_{E=E_F+eU}. \quad (2.8)$$

2.4.3 FT-STs

Fourier-transform scanning tunneling spectroscopy (FT-STs) is a technique that allows probing the electronic properties of a 2D system by characterizing standing waves in STM images. This technique is nicely described in Refs.

[37, 38]. The waves observed in STM are waves in the local density of states (LDOS) and can be related to Friedel oscillations, which are waves in the total charge density and a response of the electronic gas to locally perturbing potentials, induced by point defects or step edges. Due to the quantum-mechanical wave-particle duality, electrons that hit an impurity potential are scattered and are able to interfere with themselves forming standing waves. This can best be illustrated by a simple example, where an electron in a 2D free electron gas is described by a simple wave $e^{i\vec{k}\vec{r}}$ [37]. If this wave scatters at an infinite potential wall, the wave can be described by [37]:

$$\psi_{\vec{k}}(\vec{r}) = C e^{ik_y y} \sin(k_x x), \quad (2.9)$$

where C is a constant. In the local density of states at a given energy E a standing wave is formed [37]:

$$\text{LDOS}(\vec{r}, E) = \int_{\vec{k}} |\psi_{\vec{k}}(\vec{r})|^2 \delta(E - E_{\vec{k}}) \quad (2.10)$$

Inserting the wave function in Eq. 2.9 into Eq. 2.10 and assuming an isotropic dispersion relation of the electrons (free electron gas) reveals that the LDOS [37]:

$$\begin{aligned} \text{LDOS}(\vec{r}, E) &\propto \int_0^\pi \sin^2(k_E x \sin \Theta) d\Theta \\ &\propto 1 - J_0(2k_E x). \end{aligned} \quad (2.11)$$

The Bessel function J_0 oscillates with a wave vector of $q = 2k_E$. As the total charge density $\rho(\vec{r})$ is described by:

$$\rho(\vec{r}) = -e \int \text{LDOS}(\vec{r}, E) f(E, T) dE \quad (2.12)$$

the oscillations in the LDOS can be seen as energy-resolved Friedel oscillations. In the previous section [see Section 2.4] we showed that:

$$\frac{dI}{dV} \propto \text{LDOS}(\vec{r}, E), \quad (2.13)$$

Thus, by taking dI/dV maps at different voltages, oscillations in the LDOS can be directly observed and by taking the Fourier transformation of the dI/dV map at an electron energy $E=eV$, information about the wave vector $q = 2k_E$ can be obtained.

The state of the art technique to probe the electronic structure of solids is angle resolved photon spectroscopy (ARPES). Previous results showed that the band structure obtained by ARPES and FT-STs are in good agreement [39, 40]. However, some differences between these techniques should be pointed out. In FT-STs, both occupied and unoccupied states can be investigated by applying a negative and positive sample bias U_s . ARPES is restricted to occupied states. The sample area, which is used to obtain the information about the band structure is significantly smaller in FT-STs (up to $\sim 100 \times 100 \text{ nm}^2$) than in ARPES (beam size: $\sim 1 \text{ mm}^2$). In FT-STs, it is desirable to take as large dI/dV maps as possible to obtain a sharp scattering pattern in the fast Fourier transformation (FFT). However, taking dI/dV maps is very time consuming and recording a $25 \times 25 \text{ nm}^2$ dI/dV map takes about one hour. Although ARPES is a very surface sensitive technique, still information from the first few layers is collected, and bulk and surface states are measured at the same time. FT-STs is an even more surface sensitive technique and gives more insight into the electronic structure of the surface layer. In addition, FT-STs gives also insight into the sample quality as the number of defects and adsorbates can be easily determined. However, FT-STs also has some drawbacks as the influence of the STM tip is unknown and FT-STs cannot be applied to all materials that can be scanned with STM.

It has to be noted that FT-STs measurements should be performed in a constant-height measuring mode. Otherwise one can only obtain at $E_F \pm 0.1 - 0.2 \text{ eV}$ the correct wave vector $q = 2k_E$ [41, 42]. In our case all STs measurements were performed in a quasi-constant height mode (loop gain: 1%) and the bias voltage U_s varied between -0.05 V and $+0.1 \text{ V}$.

2.4.4 Tip-induced Manipulation

Due to certain tip-sample interactions it can easily happen that adsorbates or adatoms are not stable under the STM tip. Depending on the experiment these

tip-sample interactions can be undesirable. However, it was soon realized that with specific tip-sample interactions atomic-scale structures can be formed, such as the famous IBM letters built out of Xe atoms on Ni(110) by Eigler and Schweizer [43]. More information about “tip-induced manipulation” can be found in Refs. [44, 45].

In principle, adsorbates and adatoms can be manipulated by:

- (a) forming a Van-der-Waals or chemical bond between tip and sample
- (b) electrons tunneling from the tip into the sample
- (c) the electric field between tip and sample

(a) If the tip is brought very close to the surface (from ~ 10 Å to ~ 1 Å) the atomic orbitals of the tip and the manipulated atom can overlap and a Van-der-Waals or chemical bond is formed. Due to this interaction atoms can be pushed (repulsive tip-atom interaction), pulled (attractive tip-atom interaction) or slid (tip-atom entity is formed) across the surface. If the STM is operated in constant current mode, information about the forces between tip and sample can be determined by recording the tip height curves while moving the atoms across the surface.

The threshold tunneling resistance at which a manipulation of the adatom or adsorbate occurs is used to characterize this type of interaction. If the threshold tunneling resistance is small or large, the tip-surface distance is small or large and the tip-atom interaction weak or strong, respectively. This threshold resistance can be determined by slowly increasing the tunneling current at different bias voltages. In the case of Ag atoms on Ag(111) Hla *et al.* [46] recorded 3857 computer-automated pulling attempts and determined a threshold resistance of ~ 210 k Ω .

(b) In STM, electrons can tunnel inelastically through an adsorbed molecule, exciting various excitations. At lower energies vibrational modes can be excited and at higher energies electrons can be captured in unoccupied orbitals and excite the molecule at an electronic level. If a single electron is sufficient to excite the molecule, the process is known as single excitation. If more electrons are necessary, the process is known as a multi excitation. In

the case of the multi excitation model, the molecule is excited by the first electron and then further excited by further electrons. For this process a long lifetime of excited states is necessary so that higher states can be reached. The reaction rate R of an n -electron excitation is proportional to the current I via:

$$R \propto I^n \quad (2.14)$$

As an example, Bartels *et al.* [47] were able to transfer CO molecules from the Cu(111) surface to the tip apex by applying an U_s of +2.4 V and setting the tunneling current to a few nA. The process was explained as exciting the CO molecule via tunneling into the CO $2\pi^*$ orbital.

(c) The third possibility to manipulate atoms or molecules on the surface is using the electric field between tip and sample. Atoms and molecules that have a dipole moment can feel an attractive or repulsive force by the electric field. This way molecules can even be picked up by the STM tip at a certain bias polarity and dropped once again at the opposite polarity. The strength of the electric field between tip and sample decreases much slower ($1/r$) than the tunneling current ($1/e^{-2\kappa r}$) with increasing tip-sample distance. Thus, manipulations of atoms and molecules outside the immediate scanning area, can usually be attributed to the electric field between tip and sample.

Chapter 3

Surface Defects of Sr_2RuO_4 and $\text{Sr}_3\text{Ru}_2\text{O}_7$

This chapter is based on a manuscript published in Physical Review B 90, 165438, 2014, [48] where most parts of this chapter can also be found. However, this chapter contains more information about defects on Sr_2RuO_4 and $\text{Sr}_3\text{Ru}_2\text{O}_7$, which is not discussed in the published paper.

3.1 Introduction

Complex perovskite oxides are increasingly used in solid oxide fuel cells and in catalysis [49–52]. To obtain a better understanding the processes involved in these applications, it is desirable to obtain a better understand of their surface and chemical properties. So far, STM investigations of these perovskite oxides are rare, caused by the difficulty to prepare a well-defined surface. Sputter/annealing cycles or thin film growth, result in intermixing or reconstructed surfaces [12]. The best way to achieve a flat, bulk representative surface suitable for STM investigations is *in-situ* cleaving of single crystals (Sr_2RuO_4 [26, 53–56], $\text{Sr}_3\text{Ru}_2\text{O}_7$ [57–59] and $\text{Sr}_3\text{Ir}_2\text{O}_7$ [60]).

Scanning tunneling microscopy gives direct information about local structural, stoichiometric, and electronic inhomogeneties. Lightly Ti-doped Sr_2RuO_4 [54] and Ti- and Mn-doped $\text{Sr}_3\text{Ru}_2\text{O}_7$ [57, 58] single crystals revealed that Sr atoms are imaged as bright protrusions, and oxygen atoms are imaged

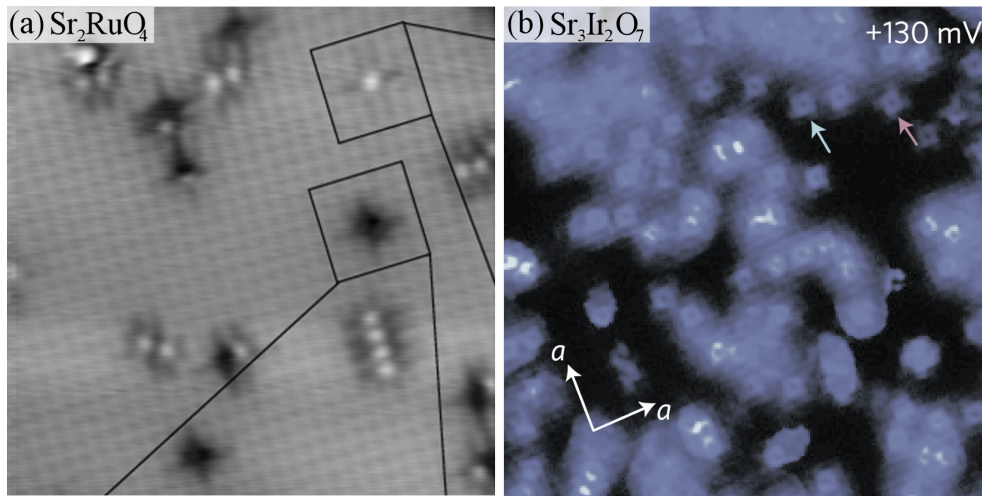


Figure 3.1: Point defects on Sr_2RuO_4 and $Sr_3Ir_2O_7$. (a) Sr_2RuO_4 cleaved at 200 K. Several bright and dark features were observed if the single crystal was cleaved at 200 K. In Ref. [53], these defects were attributed to vacancies and adatoms. (b) $Sr_3Ir_2O_7$ cleaved at 77 K. Defects are centered at the Ir/apical oxygen lattice site ($\sim 1\%$ ML). They were identified as oxygen vacancies. (a) Figure reprinted with permission from [“Cleaving-Temperature Dependence of Layered-Oxide Surfaces”, Pennec *et al.*, Phys. Rev. Lett., **101**, 216103, (2008)], [53]. Copyright © 2014 by American Physical Society. (b) Figure reprinted with permission from [“Imaging the evolution of metallic states in a correlated iridate”, Okada *et al.*, Nat. Mater., **12**, 707, (2013)], [60]. Copyright © 2014 by Nature Publishing Group.

as dark depressions in STM images. In addition, these studies revealed that dopant atoms in the surface layers can be distinguished from the regular lattice and that Mn dopants affect the distortion of the RuO_6 octahedra. Lee *et al.* [57] showed that Ti defects act as scattering centers [see Section 2.4.3], leading to quasiparticle interferences on the $\text{Sr}_3\text{Ru}_2\text{O}_7$ surface. Matzdorf *et al.* [26] first showed that Sr_2RuO_4 single crystals can be cleaved along the [001] direction, creating a flat surface, suitable for STM investigations. In addition they observed a $c(2 \times 2)$ surface reconstruction in STM and LEED. A subsequent study of Pennec. *et al.* [53] suggested that point defects are formed during cleaving, and that this process is temperature-driven [see Fig. 3.1(a)]. This idea was also picked up by Okada *et al.* [60] who investigated the surface properties of cleaved $\text{Sr}_3\text{Ir}_2\text{O}_7$. After cleaving at 78 K, about 1 % ML [1 ML: number of surface Sr or O atoms] was covered with defects, identified as oxygen vacancies [see Fig. 3.1(b)]. The hypothesis that defects are formed during cleaving goes along with puzzling ARPES measurements on Sr_2RuO_4 . Whereas Damascelli *et al.* [61] and Shen *et al.* [62] observed that cleaving at 180 K can suppress the surface states linked to the $c(2 \times 2)$ surface reconstruction [blue in Fig. 1.5(b)], Liu *et al.* did not observe this phenomenon [24, 63].

These inconsistencies motivated us to investigate defects present at the as-cleaved Sr_2RuO_4 and $\text{Sr}_3\text{Ru}_2\text{O}_7$ surface. In the following section we will discuss the defects, which are present at the as-cleaved surface and explain why the surface properties of Sr_2RuO_4 and $\text{Sr}_3\text{Ru}_2\text{O}_7$ do not depend on the cleaving temperature as previously reported.

3.2 Cleaving Planes and Surface Layer

As discussed in Section 1.2, $\text{Sr}_{n+1}\text{Ru}_n\text{O}_{3n+1}$ can cleave easily in the [001] direction and clean, flat surfaces can be created. In the case of $\text{Sr}_3\text{Ru}_2\text{O}_7$, three possible cleaving planes along the [001] direction exist. Plane 1 breaks the rock salt structure and plane 2 and plane 3 break the perovskite structure. DFT calculations [64] predict that the cleaving energy for planes 1, 2 and 3 are $0.08 \text{ eV}/\text{\AA}^2$, $0.18 \text{ eV}/\text{\AA}^2$ and $0.13 \text{ eV}/\text{\AA}^2$, respectively. In the case of plane 1 this represents a cleaving energy of 0.56 eV per broken Sr-O bond. The

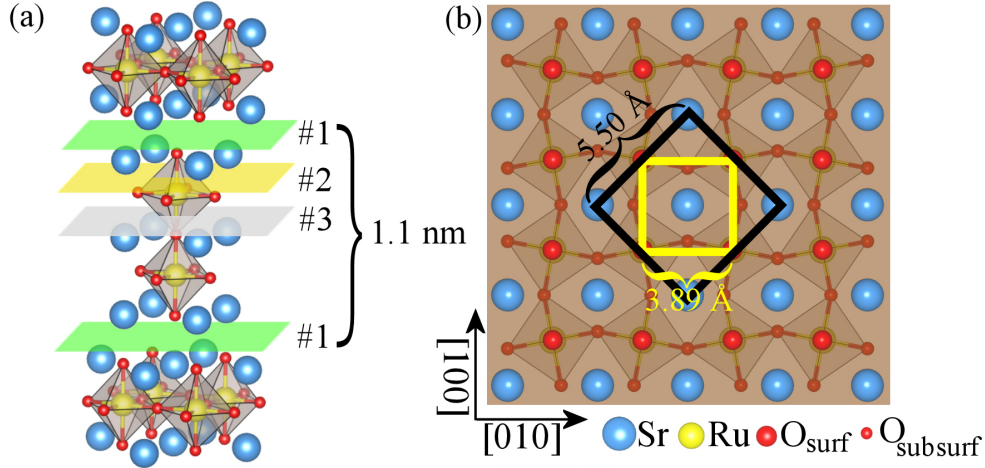


Figure 3.2: Crystal structure of $Sr_3Ru_2O_7$. (a) Three possible cleaving planes, where plane 1 breaks the rock salt and plane 2 and 3 the perovskite structure. Cleaving the rock salt layer, plane 1, is energetically favorable with a cleaving energy of 0.56 eV per broken Sr-O bond. (b) Top view of the plane-1 $Sr_3Ru_2O_7(001)$ surface, which contains Sr (blue) and O (red, large) atoms only. Smaller red circles indicate second-layer O atoms. The inner (yellow) square marks the tetragonal cell; the black square marks the unit cell of the so-called $c(2 \times 2)$ structure, which is caused by the clockwise and counterclockwise rotation of the RuO_6 octahedra.

cleaving energy is lowest for the SrO rock salt structure, thus a SrO surface layer is formed after cleaving. This finding is in agreement with previous studies on Sr_2RuO_4 , $Sr_3Ru_2O_7$ and $Sr_3Ir_2O_7$ [26, 53, 57, 60], and many other layered perovskites.

As already mentioned in the introduction, different members of the $Sr_{n+1}Ru_nO_{3n+1}$ family have different physical properties, which are correlated to slightly different crystal structures. In the case of $Sr_3Ru_2O_7$ the bulk RuO_6 octahedra are rotated by $\pm 8^\circ$ [58] and not tilted. This can be seen in Fig. 3.2(b) which shows the structure of the top $Sr_3Ru_2O_7$ surface layer. The yellow square marks the tetragonal (undistorted) bulk cell and the black square marks the primitive unit cell. It is standard notation to call to the tetragonal unit cell the (1×1) structure and the primitive unit cell the $c(2 \times 2)$ structure. This so-called $c(2 \times 2)$ pattern was already observed in LEED and in STM [26, 29, 57].

It has been reported that the top surface layer is even more distorted than the bulk truncated structure. A LEED-IV study by Hu *et al.* [29]

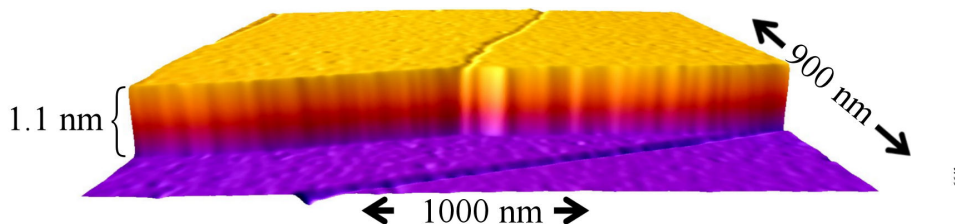


Figure 3.3: Large-scale STM image of $\text{Sr}_3\text{Ru}_2\text{O}_7(001)$. Cleaving creates large, flat terraces of a few μm^2 in size. Two terraces are separated by steps with a height of 1.1 nm. On the upper and lower terrace dark lines are observed. These lines are domain boundaries of the $c(2\times 2)$ rotation of the octahedra. Scanning conditions: $1000\times 900\text{ nm}^2$, $U_s = +1.5\text{ V}$, $I_t = 0.15\text{ nA}$, $T = 78\text{ K}$.

determines a rotation of 12° and a tilt of 4.5° . However, DFT calculations by our collaborators [64] show no sign of an additional tilting of the surface octahedra. Adsorbates, such as CO, CO₂, or water, or even radiation damage by the electron beam might change the surface structure of the top layer and affect LEED-IV results, however.

A large-scale STM image¹ [Fig. 3.3] of the cleaved Sr₃Ru₂O₇(001) surface show terraces several μm^2 in size, separated by steps with a height of 1.1 nm (multiples thereof were rarely observed), consistent with the bulk periodicity, i.e., the distance between the rock salt layers. Occasional line defects are observed. For an analysis of these lines, see Section 3.7.

3.3 STM Images of the Clean Surface

3.3.1 Sr₃Ru₂O₇

Figures 3.4(a–d) show atomically resolved STM images of the SrO surface layer of four different samples, where Sr atoms are imaged as bright protrusions and O atoms as dark depressions [64]. Sample #4 [Fig. 3.4(a)] and sample #8 [Fig. 3.4(b)] contain several defects. These include small, dark squares positioned at Sr lattice sites, bright squares at Ru/apical oxygen sites and different kinds of crosses positioned at O_{surf}/Ru lattice site. The defect coverage is in both cases $\sim 0.8\%$ ML, where 1 ML represents the number of surface Sr or O atoms

¹All STM images shown in this thesis are labeled with small numbers. In the appendix of this thesis a list can be found, which summarizes how different image numbers correlate with different samples and in which directory they can be found on the used STM computer.

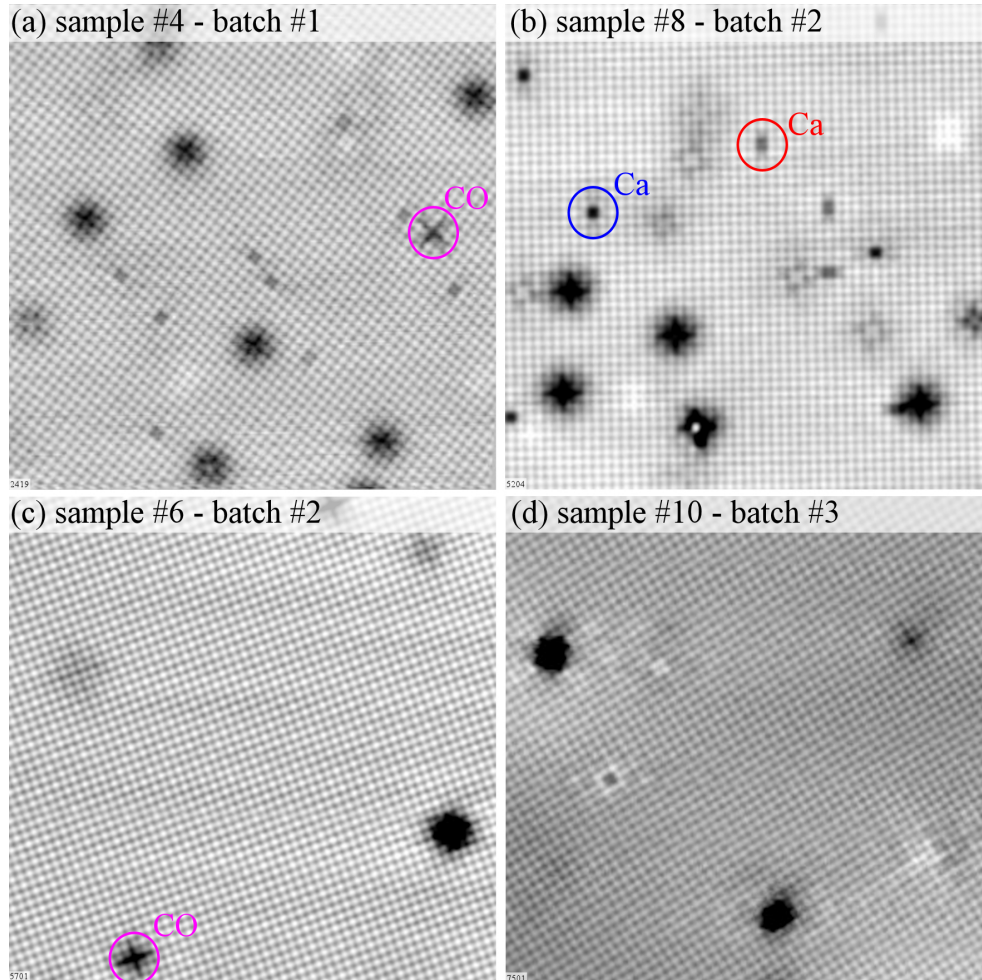


Figure 3.4: As-cleaved surfaces of four different $Sr_3Ru_2O_7$ crystals. Four different $Sr_3Ru_2O_7$ single crystals from three different sample batches were cleaved at 105 K along the [001] direction. Depending on the sample and on the sample batch the amount of defects varies. (a) The sample contains several defects positioned at the Sr and O_{surf} /Ru lattice site (coverage ~ 0.8 % ML). An adsorbed CO molecule is marked by a pink circle. (b) The defect coverage is also ~ 0.8 % ML. Ca impurities in the first and second SrO layer are marked with a blue and red circle, respectively. (c) On a few samples from batch # 2, areas with fewer defects were found. (d) All areas on samples from batch # 3 were almost defect-free. Scanning conditions: (a–d) 20×20 nm², $I_t = 0.15$ nA, $T = 78$ K. (a) $U_s = -0.1$ V, (b) $U_s = +0.05$ V, (c) $U_s = +0.05$ V, (d) $U_s = +0.1$ V.

(8×10^{-20} Atoms/cm²). Sample #6 [Fig. 3.4(c)] and sample #10 [Fig. 3.4(d)] contain significantly fewer defects. So far we were only able to identify a few of these defects. The dark squares with two different intensities, centered at the Sr lattice site are Ca impurities in the first and second SrO layer, marked in Fig. 3.4(b) with a blue and red circle, respectively. These defects will be discussed in Section 3.4.1. The big crosses, centered at a O_{surf}/Ru lattice site are adsorbed CO molecules and will be discussed in Section 4.4.

Identifying unknown features just by STM is a very difficult and sometimes even impossible task, especially if the source for observed defects is unknown. In principle there are three possible sources for the defects observed in Fig. 3.4:

- Defects formed during the cleaving process
- Adsorbates from the residual gas
- Bulk defects

As I will show in Section 3.5, I was able to intentionally create oxygen vacancies on our SrO-terminated surface; these have a different appearance than the point defects observed in Fig. 3.4. Furthermore, DFT calculations showed that the energy needed to create an oxygen and strontium vacancy is 3.81 eV and 4.19 eV, respectively [64]. This value is significantly higher than the energy needed to break the Sr-O bond (0.56 eV). Therefore, vacancies or adatoms created in the cleaving process cannot explain the defects observed in Fig. 3.4.

Even in the best UHV system molecules from the residual gas have to be considered as a possible source of contaminations. In our UHV systems the residual gas consists of CO, CO₂, H₂O and H₂ in the 10⁻¹¹ mbar range. H₂ contributes by far the most, however, no signs of H₂ adsorption or H₂ cracking on the SrO surface were observed. To investigate whether CO, CO₂, H₂O could be the source of the observed features we intentionally exposed the SrO surface layer to small amounts of these molecules [see Chapter 4 (CO), Chapter 5 (water), Section 7.2 (CO₂)]. These studies helped identifying the big cross as an adsorbed CO molecule [Fig. 3.4(a,c)]. All other features observed in Fig. 3.4(a-d) are not caused by the adsorption of CO, CO₂, or H₂O.

LA-ICP-MS	Sample # 5 - batch #2	
Al	1093 ± 47 ppm	~ 1.2 % ML
Cr	620 ± 124 ppm	~ 0.34 % ML
Fe	464 ± 93 ppm	~ 0.24 % ML
Ni	392 ± 78 ppm	~ 0.20 % ML
Mg	167 ± 43.8 ppm	~ 0.14 % ML
LA-ICP-MS	Sample # 8 - batch #2	
Ca	700 ± 100 ppm	~ 0.34 % ML

Table 3.1: Defect concentrations in mass fractions (ppm) and % ML measured by ICP-MS and ICP-OEM for samples from batch #2, which contains a high level of impurities [see Fig. 3.4 (a,b)].

Our STM studies showed that the defect density varies from sample batch to sample batch. According to STM images of different areas on samples from batch #1 and #2, the defect densities is ~ 0.8 % ML [see Fig. 3.4(a,b)] most of the time. However, in rare cases areas can be found, which contain fewer defects [see Fig. 3.4(c)]. In contrast, all samples from batch #3 contain significantly fewer defects all over the crystal [see Fig. 3.4(d)]. This result supports the hypothesis that the point defects are simple bulk impurities. The growth of ultrahigh-purity strontium ruthenates is not easily achieved, since many metals can substitute into the lattice if the starting materials, i.e., RuO or SrCO₃, do not have ultra-high purity. Even small amounts of impurities can show up prominently in STM images. The amount of impurities was too low to investigate the samples with Auger electron spectroscopy and the samples are too small to probe them with X-ray photoelectron spectroscopy (XPS). In addition, CO and CO₂, common components of the residual gas, cannot be identified by XPS on Sr₂RuO₄ and Sr₃Ru₂O₇, as the C 1s and the Ru 3d peak overlap. To determine the composition of the samples, our collaborator Andreas Limbeck (Institute of Chemical Technologies and Analytics, Vienna University of Technology) performed inductively coupled plasma mass spectroscopy (ICP-MS) using laser ablation (LA). The signal from Ca isotopes overlaps with doubly charged Sr isotopes in ICP-MS, thus inductively coupled plasma optical emission spectroscopy (ICP-OES) was used to quantify Ca. The results of this measurement [Table 3.1] confirms that small trace amounts of Al, Cr, Fe, Ni, Mg and Ca are present in samples from batch #2. So far we were only able to identify one of these impurities,

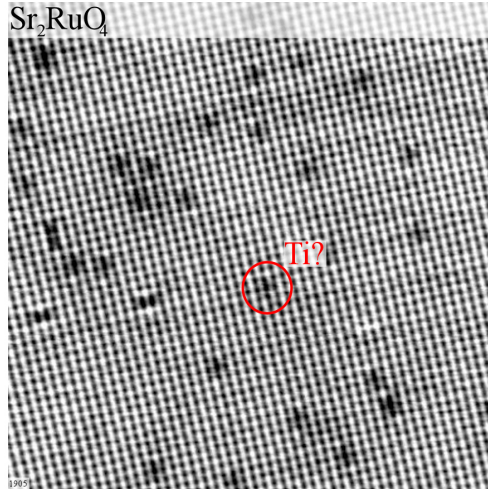


Figure 3.5: As-cleaved surface of one of our Sr_2RuO_4 crystals. The as-cleaved surface of Sr_2RuO_4 cannot be distinguished from the as-cleaved surface of $\text{Sr}_3\text{Ru}_2\text{O}_7$. Sr atoms are imaged as bright protrusions and oxygen atoms as dark depressions. All Sr_2RuO_4 single crystals contain $\sim 1\%$ ML defects centered at the Ru/apical oxygen lattice site (marked with a red circle). These features might be Ti impurities, as Barker *et al.* [54] showed that Ti dopants in Sr_2RuO_4 have a very similar appearance. Scanning conditions: $20 \times 20 \text{ nm}^2$, $U_s = +0.1 \text{ V}$, $I_t = 0.15 \text{ nA}$, $T = 78 \text{ K}$.

namely Ca, which appears as dark squares centered at the Sr lattice site [Section 3.4.1]. To convert (ppm) into % ML, first the mass fractions (ppm) which are given in $\mu\text{g/g}$ have to be transformed into amount of impurity atoms per 1 gram $\text{Sr}_3\text{Ru}_2\text{O}_7$. Afterwards this value has to be compared to the amount of Sr or Ru atoms in 1 gram $\text{Sr}_3\text{Ru}_2\text{O}_7$, depending whether the impurity atom replaces Sr or Ru atoms.

3.3.2 Sr_2RuO_4

As mentioned before, Sr_2RuO_4 is the one-layered member of the ruthenate Ruddlesden-Popper series $\text{Sr}_{n+1}\text{Ru}_n\text{O}_{3n+1}$. Previous studies [26] showed that these crystals also cleave between two SrO layers. In Sr_2RuO_4 the RuO_6 octahedra exhibit no tilt as in $\text{Sr}_3\text{Ru}_2\text{O}_7$ and no rotation, in contrast to $\text{Sr}_3\text{Ru}_2\text{O}_7$ ($\sim 8^\circ$, 90 K [29]). However, at the surface the octahedra are rotated by ($\sim 8^\circ$, 80 K [25]) in the Sr_2RuO_4 system. Therefore the top surface layer of Sr_2RuO_4 and $\text{Sr}_3\text{Ru}_2\text{O}_7$ both exhibit a very similar $c(2 \times 2)$ structure and very similar surface properties can be expected. Indeed, just by

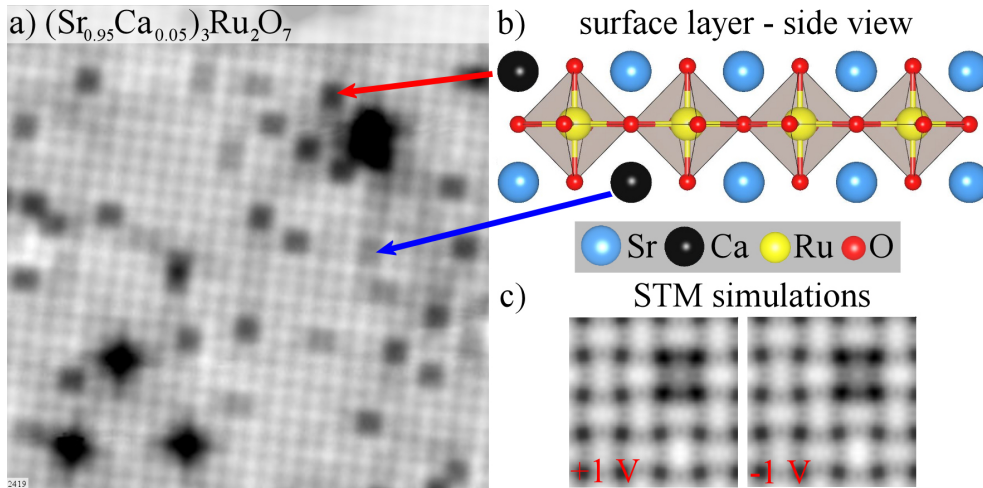


Figure 3.6: STM images of the cleaved $(Sr_{0.95}Ca_{0.05})_3Ru_2O_7(001)$ surface. (a) Ca atoms replacing Sr atoms in the first and second SrO layer appear as black and grey squares, respectively. (b) Side view of the surface layer of $(Sr_{0.95}Ca_{0.05})_3Ru_2O_7$; color code: Sr (blue), Ca (black), Ru (yellow) and O (red). (c) Simulated STM images of Ca dopants in empty and filled states confirm the dark appearance of Ca with respect to its surrounding [64]. Scanning conditions: $10 \times 10 \text{ nm}^2$, $U_s = +0.15 \text{ V}$, $I_t = 0.15 \text{ nA}$, $T = 78 \text{ K}$.

STM it is not possible to distinguish these two members of the $Sr_{n+1}Ru_nO_{3n+1}$ series [Fig. 3.5]. All Sr_2RuO_4 samples contained about 1 % ML of defects positioned at the O_{surf}/Ru lattice site. Similar defects were not observed in our $Sr_3Ru_2O_7$ samples. However, STM investigations by Barker *et al.* [54] show that Ti dopants in Sr_2RuO_4 have a very similar appearance.

3.4 Intentionally Doped Samples

To investigate the appearance of impurity atoms, we imaged the surfaces of intentionally Mn- and Co-doped Sr_2RuO_4 , and Ca-doped $Sr_3Ru_2O_7$ single crystals. Whereas Ca is one of the impurities in our pure samples, the trace analysis showed no signs of Co or Mn. However, the Mn and Co doped samples should still give an impression how impurities at the Ru lattice site look like.

3.4.1 $(\text{Sr}_{0.95}\text{Ca}_{0.05})_3\text{Ru}_2\text{O}_7$

Figure 3.6(a) shows an STM image of the as-cleaved $(\text{Sr}_{0.95}\text{Ca}_{0.05})_3\text{Ru}_2\text{O}_7$ surface. Black squares (red arrow) and grey squares (blue arrow) are located at the position of the surface Sr atoms. We identify these black and grey squares to Ca atoms replacing the Sr atoms in the first and second SrO layer, respectively [Fig. 3.6(b)]. An STM simulation of Ca in the top surface layer confirms its dark appearance with respect to the surrounding Sr atoms [Fig. 3.6(c)], [64]. Counting the Ca atoms in a $20 \times 20 \text{ nm}^2$ STM image yields about 5.8 % and 3.4 % replaced Sr atoms in the first and second layer, respectively, which is in agreement with a Ca doping level of 5% (a very limited data set where the Ca atoms in the first and second layer could be distinguished easily did not allow to determine error bars). The difference between the concentration of the first and second layer is most likely caused by the imperfect distribution of the Ca atoms in the bulk and the fact that STM can only probe a very small area on the sample, which leads to poor statistics. The Ca atoms have 2-fold and not 4-fold symmetry; they are extended along either the [100] or [010] direction, depending on their position within the $c(2 \times 2)$ unit cell.

These Ca impurities in the first and second SrO layer could be observed in almost all of our ~ 50 undoped samples that we have investigated by STM [see Fig. 3.4], in agreement with the chemical analysis [see Table 3.1].

3.4.2 $\text{Sr}_2\text{Ru}_{0.97}\text{B}_{0.03}\text{O}_4$, (B=Mn,Co)

Figure 3.6 shows several different features centered at the Ru/apical oxygen lattice site. In principle, such features could be explained by oxygen vacancies, O adatoms, or bulk impurities. Whereas Okada *et al.* [60] suggested that oxygen vacancies are formed during cleaving, our trace analysis confirms that our crystals contain small amounts of Mg, Al, Cr, Fe, Ni and Ca [see Table 3.1]. The STM images of $\text{Sr}_2\text{Ru}_{0.97}\text{Co}_{0.03}\text{O}_4$ [Fig. 3.7(a)] and $\text{Sr}_2\text{Ru}_{0.97}\text{Mn}_{0.03}\text{O}_4$ [Fig. 3.7(b)] show that dopants, which replace Ru atoms, are clearly visible in STM. The Co atoms appear as bright spots in filled and empty states, centered perfectly at the Ru/apical oxygen lattice site. The Mn dopants appear as bright spots centered at the Ru/apical oxygen

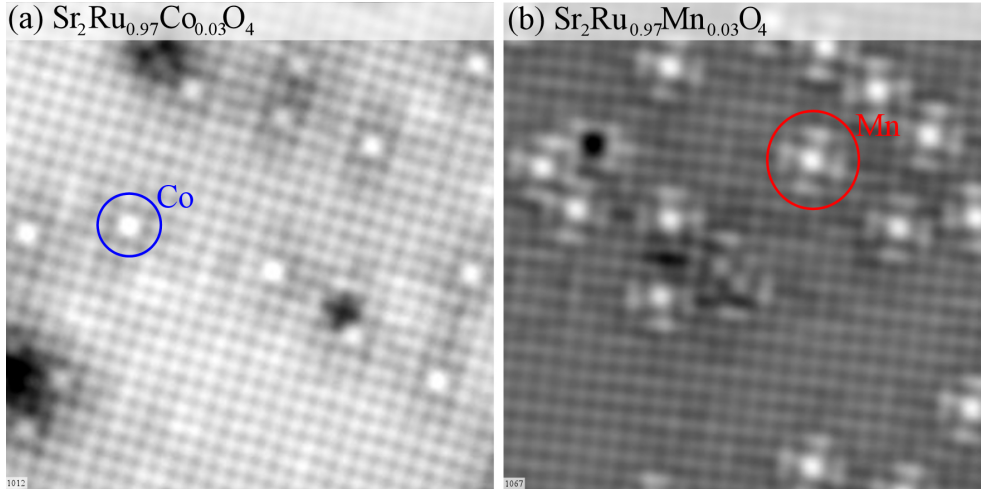


Figure 3.7: STM images of intentionally doped Sr_2RuO_4 single crystals. (a) Co atoms replacing the Ru atoms in $Sr_2Ru_{0.97}Co_{0.03}O_4$ appear as bright protrusions positioned at the Ru/apical oxygen lattice site. (b) Mn atoms replacing the Ru atoms in $Sr_2Ru_{0.97}Mn_{0.03}O_4$ appear also as bright protrusions positioned at the Ru/apical oxygen lattice site. In addition, the bright spot is superimposed with a cross-like feature. Scanning conditions: (a) $10 \times 10 \text{ nm}^2$, $U_s = +0.05 \text{ V}$, $I_t = 0.15 \text{ nA}$, $T = 78 \text{ K}$, (b) $10 \times 10 \text{ nm}^2$, $U_s = +0.1 \text{ V}$, $I_t = 0.25 \text{ nA}$, $T = 6 \text{ K}$.

lattice site, each with an additional weak cross feature. At 6 K standing waves can be observed on the Mn doped Sr_2RuO_4 surface. These waves form when quasiparticles scatter at impurities and interfere with themselves. These results will be further discussed in Chapter 6.

3.5 Oxygen Vacancies

Defects such as step edges or vacancies can severely affect the properties of metal oxides and are often thought to be the reactive sites of the material. Oxygen vacancies can behave quite differently, depending on the metal oxide. For example, the resulting excess electrons in MgO are trapped at the vacancy site, in SiO_2 they occupy bonding and antibonding orbitals, and in TiO_2 they behave somehow between these two cases [65]. In rutile, excess electrons can localize at any Ti atom, forming a small polaron that can hop to neighboring Ti sites. In anatase excess electrons can only be trapped near oxygen vacancies and prefer a free-carrier state [65]. The fact that these surface defects can act as reactive sites can be observed on TiO_2 . Consecutive STM images directly

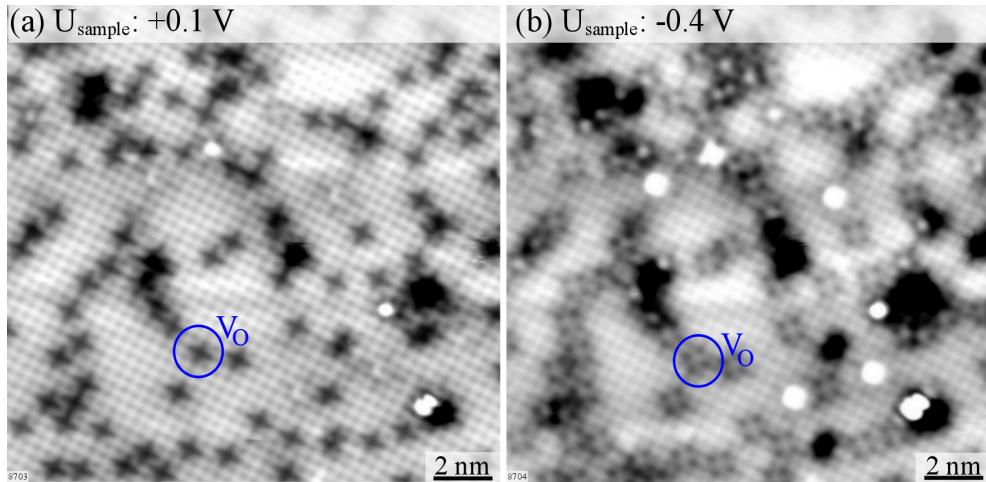


Figure 3.8: Oxygen vacancies on $\text{Sr}_3\text{Ru}_2\text{O}_7(001)$. (a,b) STM images of a $\text{Sr}_3\text{Ru}_2\text{O}_7(001)$ surface following bombardment with 1000 eV electrons at 105 K. (a) In empty-states ($U_s = +0.1$ V) oxygen vacancies appear as small, dark crosses. (b) In filled states ($U_s = -0.4$ V) oxygen vacancies appear as small, bright squares. Both features are centered at apical oxygen/subsurface Ru atoms. Scanning conditions: (a,b) $16 \times 16 \text{ nm}^2$, $I_t = 0.15 \text{ nA}$, $T = 78 \text{ K}$, (a) $U_s = +0.1 \text{ V}$, (b) $U_s = -0.4 \text{ V}$.

show how water adsorbs on the Ti rows, interacts with the oxygen vacancy and form two surface hydroxyls [66].

Due to these fascinating properties of oxygen vacancies, there is a great interest in these defects. So far oxygen vacancies on binary metal oxides have been investigated intensively. Much less is known about oxygen vacancies of ternary metal oxides, such as perovskites.

It is known that surface oxygen vacancies (V_{OS}) can be created on many metal oxide surfaces by electron bombardment [67, 68]. Following bombardment with 1000 eV electrons for 45 minutes at 105 K (current: $\sim 5 \mu\text{A}$, bombarded area: $\sim 1 \text{ mm}^2$), new features appear that are centered at the position of the apical oxygen/subsurface Ru atom [Fig. 3.8]. Counting the number of these features in the STM images yields an estimated cross section for electron-induced oxygen desorption of the order of $\sim 10^{-20} \text{ cm}^2$. In empty-states images [Fig. 3.8(a)] V_{OS} appear as small, dark crosses, while in filled states they appear as bright squares [Fig. 3.8(b)]. Such features were not observed on the as-cleaved surface. While simulated STM images show reasonable agreement with experiment for occupied states [64], the

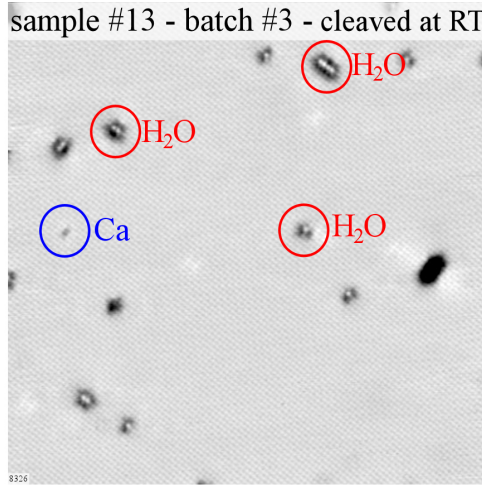


Figure 3.9: Influence of the cleaving temperature. STM images of a $Sr_3Ru_2O_7(001)$ crystal, cleaved at room temperature. Only very few defects are present at the as-cleaved surface. These defects are identified as water monomers and multimers (marked with red circles), and a Ca atom (marked with a blue circle). Scanning conditions: $40 \times 40 \text{ nm}^2$, $U_s = +0.2 \text{ V}$, $I_t = 0.15 \text{ nA}$, $T = 78 \text{ K}$.

calculations predict a bright appearance in the unoccupied-states images.

3.6 Influence of the Cleaving Temperature

Pennec *et al.* [53] investigated the cleaving-temperature dependence of layered oxide surfaces, and came to the conclusion that the surface quality of Sr_2RuO_4 single crystals depends strongly on the cleaving temperature. Crystals cleaved at 200 K contained significantly more defects than crystals cleaved at 20 K.

In contrast, our studies show that cleaving at different temperatures does not affect the quality of the as-cleaved surface. Our samples cleaved at room temperature contain similar features as observed by Pennec *et al.*. However, the defect coverage of our samples cleaved at room temperature is significantly less than the coverage observed by Pennec *et al.* who cleaved their samples at 100 K. Fig. 3.9 shows 21 features in total of which are 17 water molecules (a few are marked by red circles, see Chapter 5), one Ca atom (marked by a blue circle, see section 3.4.1) and 4 unknown defects.

Samples cleaved at 105 K usually do not contain water adsorbates on the as-cleaved surface, as the cooled sample manipulator acts as a cryo pump. Therefore, we usually cleaved our samples at 105 K to reduce the initial

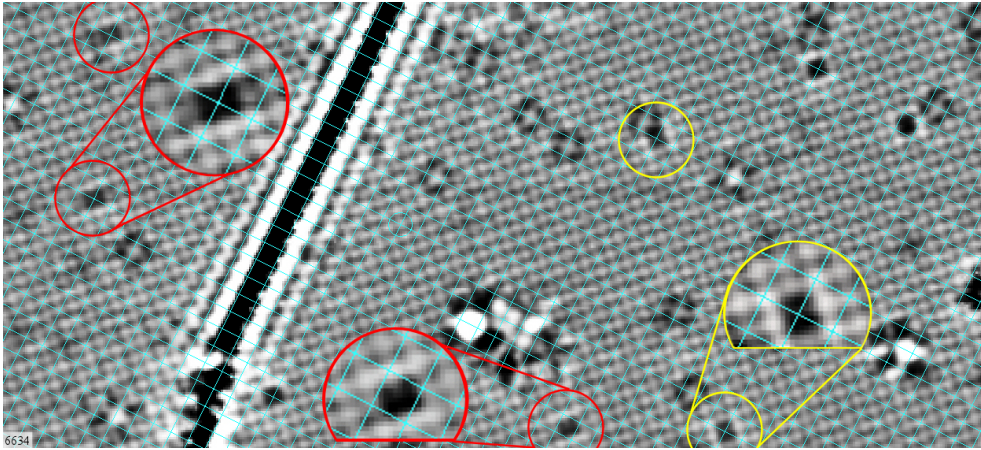


Figure 3.10: Domain boundary. The dark line (domain boundary) separates two areas on the crystal where the RuO_6 octahedra are rotated differently. The $c(2 \times 2)$ structure can best be visualized by the different appearance of defects. The crossing points of the blue $c(2 \times 2)$ grid lines are centered on half of the surface Sr atoms. The second half of the Sr atoms rest in the center of the grid squares. The Ca defects marked with a red circle on the left side and the Ca defects marked with a yellow circle on the right side are rotated by 90° , although they sit on the same lattice site (grid lines cross). $27.6 \times 12.1 \text{ nm}^2$, $U_s = -0.3 \text{ V}$, $I_t = 0.15 \text{ nA}$, $T : 78 \text{ K}$.

contamination of our samples.

3.7 Domain Boundaries

The large-scale image of the $\text{Sr}_3\text{Ru}_2\text{O}_7(001)$ crystal at the beginning of this chapter showed two lines that start (or end) at a step edge [see Fig. 3.3]. A zoomed-in images of one of these lines reveal that the defects are domain boundaries between two different rotations of the octahedra [see Fig. 3.10]. Octahedra that are rotated clockwise on the left side of the domain boundary are rotated counter-clockwise at the same lattice site on the right side of the domain boundary and vice versa. These domain boundaries are only a property of the surface bi-layer and do not expand over step edges, as two bi-layers of different terraces are not coupled due to an additional SrO layer [see crystal structure, Fig. 3.2].

The different rotation of the RuO_6 octahedra can be seen indirectly by the appearance of the same types of defects on the left and right side. As discussed in Section 3.4.1 Ca dopants in the first and second SrO layer appear always slightly elongated along the $[100]$ or $[010]$ direction. Whether they

are elongated along the [100] or [010] direction is dictated by the $c(2 \times 2)$ structure, and thus by the rotation of the octahedra. The Ca defects in the second SrO layer [see grey defects, Fig. 3.6(a)] marked with a red circle on the left side and the Ca defects in the second SrO layer marked with a yellow circle on the right side of the domain boundary are rotated by 90° , although they sit on the same lattice site (grid lines cross). Thus, the octahedra have to be rotated in opposite directions on both sides of the domain boundary. In the top right side of the Fig. 3.10 two Ca atoms in the first layer are visible. We ignore these defects for analyzing the RuO_6 rotations, as Fig. 3.10 shows no Ca impurities in the first SrO layer on the left side of the domain boundary.

3.8 Unidentified Structures

In addition to the defects already discussed, we also observed more extended defects of a few \AA^2 in size, as well as and some line defects, which have already been observed in other STM studies [53, 55]. These latter defects occurred rarely on the Sr_2RuO_4 and $Sr_3Ru_2O_7$ samples. Due to the limited number of STM images an identification of these defects was not possible. However, sharing these results may help others working with strontium ruthenates.

3.8.1 Line Defects, Dark Depressions and Bright Hills

Figures 3.11(a–c) show three defects that can be found regularly on Sr_2RuO_4 and $Sr_3Ru_2O_7$ samples. The line defects in Fig. 3.11(a) are oriented along [110] and [1-10] directions. These are not domain boundaries because they do not enclose an area but can end in the middle of one terrace. Similar defects have been already observed by [53, 55], who identifies these lines as Ru lamellar microdomains. For Sr_2RuO_4 Maeno *et al.* [69] found that embedded Ru lamellar microdomains (width: $1 \mu\text{m}$, depth and length: $1\text{--}10 \mu\text{m}$) can increase the superconducting transition temperature from $T_c = 1.5 \text{ K}$ for Sr_2RuO_4 to $T_c = 3 \text{ K}$. These lamellar structures look somehow similar to our line defects, but have a different length scale: $1 \mu\text{m}$ vs. 1 nm . However, the possibility that we observe in our STM images “nano”-domains cannot be excluded.

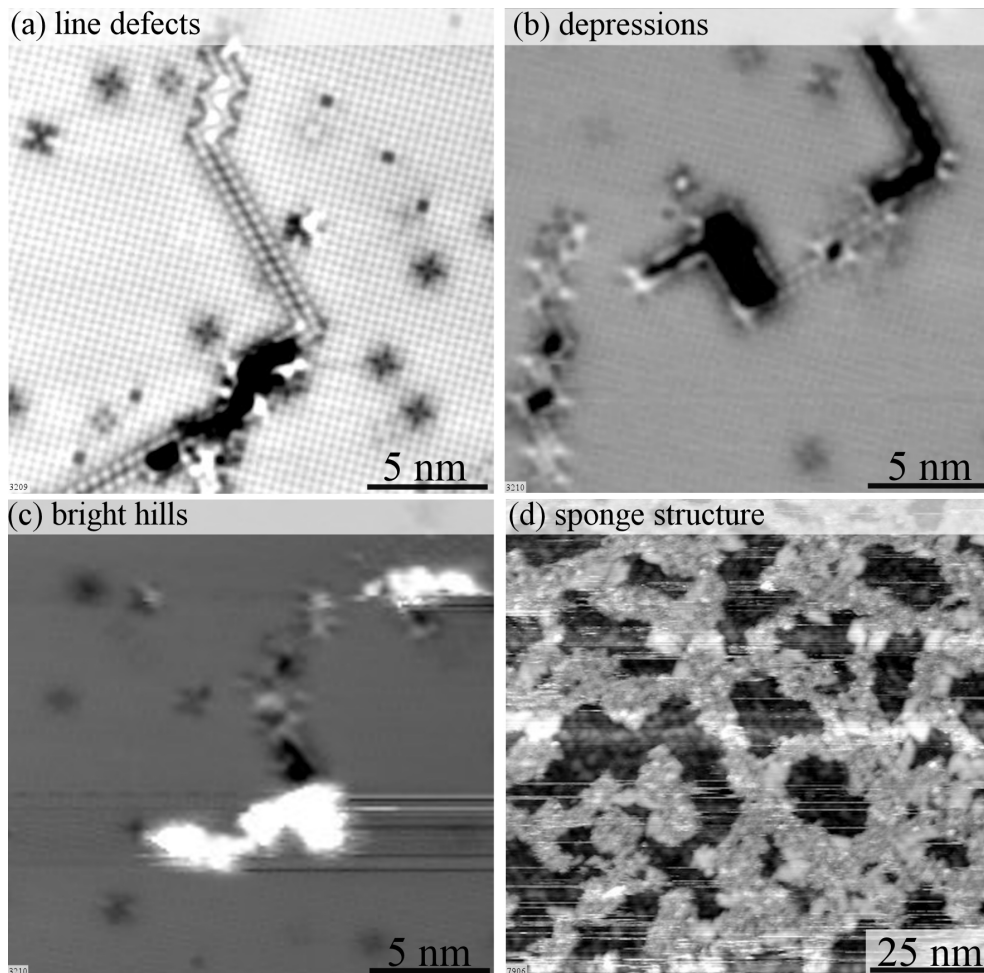


Figure 3.11: Unidentified defects. (a) Unidentified line defects. The lines are oriented along $[110]$ and $[1-10]$ directions and can end in the middle of a terrace. Thus, they are not domain boundaries. (b) If the line defects get thicker, they appear as dark areas in STM. (c) Bright hills often appear next to the line defects and dark areas. The hills and depressions might be seen as two fitting pieces of a puzzle. (d) “Sponge structure”: Unknown bulk defects, which were rarely observed on certain areas of the sample. Scanning conditions: (a–d) $I_t = 0.15$ nA, $T = 78$ K, (a) $U_s = +0.15$ V, (b) $U_s = +0.15$ V, (c) $U_s = +0.15$ V, (d) $U_s = -0.3$ V.

In addition, to these line defect sometimes dark depressions [Fig. 3.11(b)] and bright hills [Fig. 3.11(c)] can be found. As we always observed hills and depressions, these two features can be seen as two fitting pieces of puzzle. These defects could be either different members of the strontium ruthenate Ruddlesden-Popper series, or an indication that the crystal did not cleave between two SrO layers but between the SrO and the RuO₂ layer [56].

3.8.2 “Sponge”-Structure

Three out of 50 cleaved single crystals showed a sponge-like structure as shown in the large-scale STM image, Fig. 3.11(d). This structure was not spread across the entire surface layer, since by moving the STM tip macroscopically we could also find the standard perovskite surface. Thus, these defects have to be bulk defects and are not caused by adsorbates. One plausible explanation is that during the crystal growth instead of two SrO layers next to each other, three SrO layers grew. However, the step height expected for bulk SrO is 2.6 Å and larger than the measured step height of 1.8 Å.

3.9 Conclusion

Whereas previous studies by Pennec *et al.* [53] and Okada *et al.* [60] suggested that cleaving of layered perovskite creates defects on the as-cleaved surface, we have clearly shown that point defects on the as-cleaved surface result from bulk impurities and (see below) the adsorption of CO, H₂O, CO₂. Neither oxygen vacancies nor strontium vacancies are created during the cleaving process. Thus, also features observed on Sr₃Ir₂O₇ [60] are most likely bulk impurities and not oxygen vacancies.

Our experiments also showed that oxygen vacancies can be created intentionally by electron bombardment. The appearance of these vacancies varies significantly with the bias voltage, as they appear as bright protrusions and dark crosses in empty and filled states measuring mode, respectively.

Some of the Sr₃Ru₂O₇ samples contain impurities in the ~ ppm to 100 ppm range, as determined by a trace analysis. This points out the difficulty to grow extremely pure strontium ruthenates, since many metals can substitute

into the lattice if the starting materials, i.e., RuO and SrCO₃, do not have ultra-high purity.

Our STM images showed that even in UHV systems with a base pressure of 1×10^{-11} mbar CO and water can already contaminate the as-cleaved surface. Therefore we suggest that cleaving-temperature dependent ARPES signals are caused by adsorbates from the residual gas. In poor vacuum conditions a difference could occur if cold surfaces in the vicinity of the sample act as a cryogenic pump, reducing the local pressure around a freshly cleaved surface. Cleaving at room temperature would have no such benefits, and the sample would suffer more contamination.

Meevasana *et al.* and Wang *et al.* [70, 71] showed that oxygen vacancies can be formed on SrTiO₃ by photon irradiation. Our electron bombardment results show that O vacancies on strontium ruthenate surfaces are easily created by electronic excitations. This has to be considered in synchrotron experiments, as beam damage might occur.

Chapter 4

Adsorption of CO

The following chapter is based on a manuscript published in Physical Review Letters 113, 116101, 2014, [72]. However, this chapter includes additional information that cannot be found in the published manuscript.

4.1 Introduction

As mentioned in the last chapter, puzzling effects have been observed on Sr_2RuO_4 and $\text{Sr}_3\text{Ru}_2\text{O}_7$ single crystals. ARPES measurements by different groups showed surface properties that can vary with varying cleaving temperatures, others showed that the same properties do not change with changing cleaving temperature. For Sr_2RuO_4 a suppression of surface states could be observed if the cleaving temperature was increased to 180 K, surface degradation was observed if the sample temperature was cycled between 10 and 200 K and surface-“aging” was found if the sample was just kept in UHV for a longer time. These observations could be partially explained by the result of Pennec *et al.* [53] result that the surface quality can change when the single crystals are cleaved at different temperatures. However, we have already shown [see Chapter 3] that cleaving at different temperatures has no influence on the surface quality. Therefore there has to be another explanation for these puzzling results.

As carbon monoxide is one of the main constituents of the residual gas in UHV systems, the interaction of CO with any surface is of great interest.

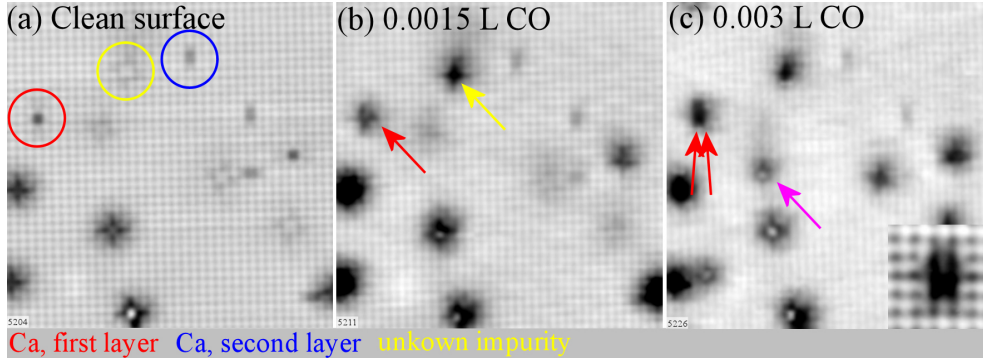


Figure 4.1: Initial CO adsorption on the $\text{Sr}_3\text{Ru}_2\text{O}_7(001)$ surface at 78 K. (a) The clean surface contains several point defects: Ca impurities in the first SrO layer (red), Ca impurities in the second layer (blue), and an unknown impurity (yellow). (b) After dosing 0.0015 L CO, molecules adsorb first at defects. Cross-like features are formed at Ca atoms of the first layer (red arrow) and at the unknown defect (yellow arrow). (c) After dosing another 0.0015 L CO, a second CO molecule can adsorb at the Ca defect of the first layer (two red arrows). The inset shows a high-quality image of two CO molecules sitting at one Ca defect. Once all defect sites are saturated, CO adsorbs on the clean surface (pink). Scanning conditions: (a–c) $15 \times 15 \text{ nm}^2$, $I_t = 0.15 \text{ nA}$, $T = 78 \text{ K}$, (a) $U_s = +0.05 \text{ V}$, (b) $U_s = +0.05 \text{ V}$, (c) $U_s = +0.10 \text{ V}$.

We show that the CO molecules interact strongly with the two top layers of $\text{Sr}_3\text{Ru}_2\text{O}_7$ and Sr_2RuO_4 . In the case of $\text{Sr}_3\text{Ru}_2\text{O}_7$ the CO molecule forms first a weakly adsorbed precursor, and after overcoming a small activation energy ($E_{\text{act}} = 0.17 \text{ eV}$ [64]), a strongly bound COO species forms with the underlying Ru atom. The strong reactivity of the Sr_2RuO_4 and $\text{Sr}_3\text{Ru}_2\text{O}_7$ surfaces could explain the puzzling ARPES measurements mentioned earlier.

4.2 Initial Adsorption

We investigated the first steps of the CO adsorption by dosing small amounts of CO (0.0015 Langmuir, $1 \text{ L} = 1 \times 10^{-6} \text{ torr sec}$, gas temperature: 300 K) into the cold STM (78 K) onto $\text{Sr}_3\text{Ru}_2\text{O}_7$. The tip was retracted for ~ 50 steps for dosing and reapproached at the same position. The gas dose was simply measured by the ion gauge and the exact dose on the sample inside the STM will vary from this value.

Figure 4.1(a) shows the initially clean surface. Several point defects are seen, which are bulk impurities as described in Section 3.3. One Ca impurity

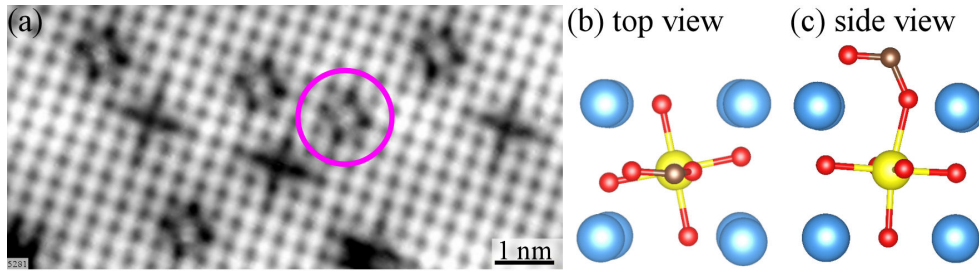


Figure 4.2: CO-precursor adsorbed on the $\text{Sr}_3\text{Ru}_2\text{O}_7(001)$ surface. (a) STM image: CO adsorbs weakly ($E_{\text{ads}} = -0.66$ eV [64]) on top of an apical oxygen atom (marked with a pink circle). (b,c) Calculated structure of the precursor [64]. Color code: Sr (blue), Ru (yellow), O (red), C (brown). Scanning conditions: $9.5 \times 4.5 \text{ nm}^2$, $U_s = +0.1$ V, $I_t = 0.15$ nA, $T = 78$ K.

in the first and one in the second layer are marked with red and blue circles, respectively. One unknown defect at the Ru lattice site is marked with a yellow circle. After dosing 0.0015 L of CO the appearance of the Ca impurity in the first layer and the appearance of the unknown defect changed, indicating transient mobility of the adsorbate [see Fig. 4.1(b)]. Cross-like features can be observed at the unknown defect at the Ru/apical oxygen lattice site [Fig. 4.1(b), yellow arrow] and next to the Ca impurity in the first layer [Fig. 4.1(b), red arrow]. The Ca impurities in the second layer did not react with the CO molecules. After dosing an additional 0.0015 L CO (0.003 L total), see Fig. 4.1(c), all Ca impurities in the first layer are covered with two CO molecules right next to each other (two red arrows; inset), all (unknown) white square-defects are covered with CO and new features appear on the clean surface [Fig. 4.1(c), pink arrow].

4.3 Precursor

The purple marked features adsorbed on the clean surface [Fig. 4.1(c)] is the first stage of the CO adsorption on perfect $\text{Sr}_3\text{Ru}_2\text{O}_7$ that we can observe by STM and will be called CO-precursor in the following. This feature was only observed on $\text{Sr}_3\text{Ru}_2\text{O}_7$, but not on Sr_2RuO_4 . A high-resolution STM image [see Fig. 4.2 (a)] reveals that the CO adsorbs right on top of an apical oxygen atom. The appearance of this precursor does not change significantly with different tunneling conditions and always looks like a bright spot right on top

of an apical oxygen atom in filled- and empty-states. This configuration is in agreement with a DFT derived geometry [see Fig. 4.2 (b,c), [64]], where the C bonds downwards to the surface oxygen atom and the O points towards a Sr bridge site [64]. According to DFT, the C-O bond length increases to 1.27 Å (gas phase: 1.14 Å), and the distance between the carbon and surface oxygen atom is 1.35 Å. The predicted adsorption energy for this physisorbed CO-precursor is $E_{\text{ads}} = -0.66$ eV [64, 72].

4.4 Carboxylate

Next to the five precursor molecules shown in Fig. 4.2(a) dark crosses are found. These are also centered at the Ru/apical oxygen site. The crosses always consist of one thicker and one thinner bar, which can be rotated by 90° [see Fig. 4.3(a), purple and yellow circle], which illustrates two different orientations of the adsorbate. These crosses are a second, more stable, adsorption configuration of CO.

With the help of DFT we could identify these features as a chemisorbed adsorption configuration ($E_{\text{ads}} = -2.17$ eV [64, 72]) where a carboxylate is formed. In this configuration the carbon atom replaces the apical oxygen atom and forms a Ru-COO species [see Fig. 4.3(c)]. The Ru atom is pulled upwards by 0.33 Å and the C-Ru bond length is 2.03 Å. The two oxygen atoms of the COO-species point towards two Sr bridge positions with an O-C-O angle of 119°. Both C-O bonds are elongated to a value of 1.3 Å due to partial occupation of antibonding intramolecular states. Due to symmetry reasons the carboxylate can be rotated by 90° [see Fig. 4.3(b,c)]. The lattice next to the carboxylate is slightly distorted, caused by the formation of the Ru-COO species. In particular the neighboring RuO₆ octahedra tilt. This tilt is most pronounced for the octahedra aligned with the COO axis (about 6° additional tilt).

STM images suggest that the very same structure is formed if CO adsorbs on the SrO surface of Sr₂RuO₄ [see Fig. 4.3(d)]. After dosing 0.04 L of CO onto Sr₂Ru_{0.97}Mn_{0.03}O₄ at 10 K no interaction of the CO molecules with the defects and no sign of a precursor can be found. One single Mn atom is marked with a red circle. Due to a relatively “bad tip” it is difficult to identify

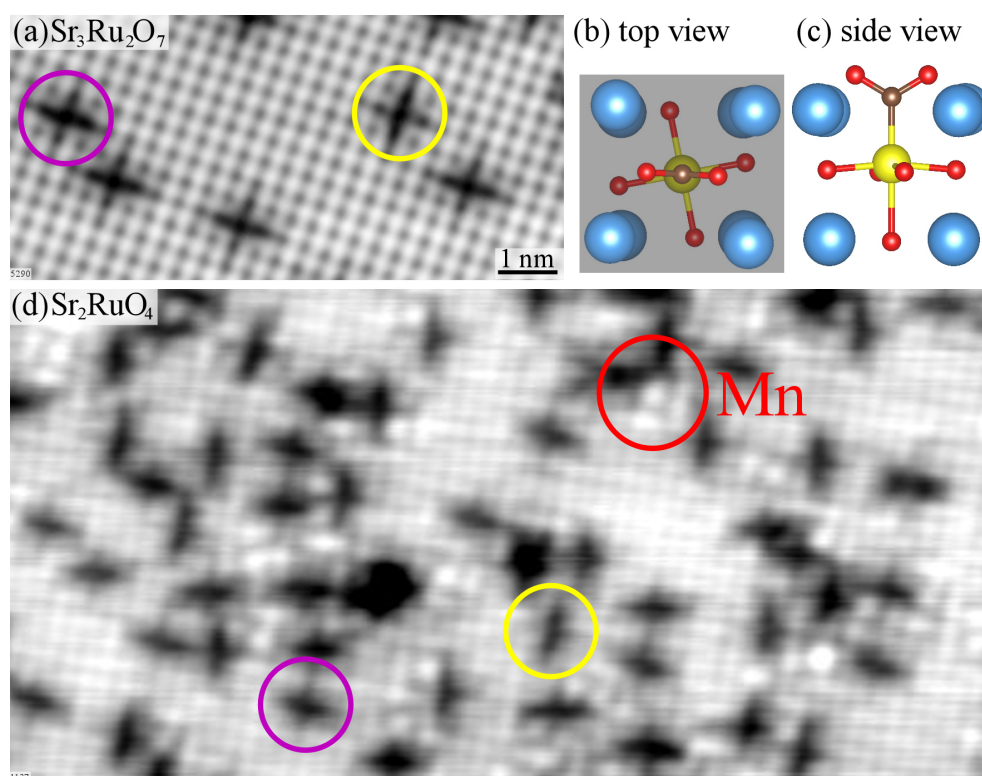


Figure 4.3: CO-cross adsorbed on the $\text{Sr}_3\text{Ru}_2\text{O}_7$ and $\text{Sr}_2\text{RuO}_4(001)$ surface. (a) STM image of the CO-cross (carboxylate) adsorbed on $\text{Sr}_3\text{Ru}_2\text{O}_7$: CO adsorbed strongly ($E_{\text{ads}} = -2.2$ eV) on top of an apical oxygen atom [64]. The CO-crosses always consist of one thicker and one thinner bar, which can be rotated by 90° (purple and yellow circles). (b,c) Top and side view of the CO-cross. Color code: Sr (blue), Ru (yellow), O (red), C (brown). (d) STM image of the carboxylate adsorbed on 3 % Mn doped Sr_2RuO_4 . No influence of the dopants (Mn, red circle) was observed. Adsorbed CO also forms two different CO-crosses, where the O-C-O complex is rotated by 90° (purple and yellow circles). Scanning conditions: (a) 9.5×4.5 nm², $U_s = +0.2$ V, $I_t = 0.15$ nA, $T = 78$ K, (d) 20×10 nm², $U_s = +0.1$ V, $I_t = 0.15$ nA, $T = 6.3$ K.

Mn atoms, which are close to CO crosses. On Sr_2RuO_4 also two different orientations of the the CO-crosses (purple and yellow circle) are found. Thus, although no calculations of the Sr_2RuO_4 system were performed, its quite safe to say that a carboxylate is also formed on Sr_2RuO_4 .

When the CO-covered $\text{Sr}_3\text{Ru}_2\text{O}_7$ sample was annealed to 420 K no desorption was observed, which is not surprising considering the calculated adsorption energy of $E_{\text{ads}} = -2.17$ eV. Unfortunately, we were not able to anneal the sample to higher temperatures, as we needed to avoid outgassing of the epoxy glue. Therefore, we could not find out experimentally if CO desorbs as CO or as a CO_2 , leaving an oxygen vacancy behind. In PBE calculations [64, 72] the oxidation of CO to CO_2 results in an energy gain of 3.3 eV. However, the energy to create an oxygen vacancy is 3.8 eV and therefore desorption as CO should be expected.

4.5 Transition: Precursor - Carboxylate

The transition from the physisorbed CO-precursor to the chemisorbed CO-cross was investigated by DFT calculations [64]. During this transformation, the O-Ru bond breaks, and a C-Ru bond is formed. The energy barrier for this process is quite small ($E_{\text{act}} = 0.17$ eV) as shown in the energy diagram [see Fig. 4.4(c)]. This activation barrier can be overcome either by annealing the sample to 100 K, or by scanning at slightly higher bias voltages. The second process is shown in Fig. 4.4(a,b) where the blue marked CO precursors transform into two CO-crosses after applying a bias voltage of +1 V.

The energy diagram [Fig. 4.4(c)] also shows that there is a small activation energy ($E_{\text{act}} = 0.44$ eV) for rotating one CO-cross by 90° in plane. Experimentally this can be done by scanning at increased bias voltages of about $U_s = +2.4$ V.

4.6 Reaction V_O - CO_2

The DFT derived structure model for the Ru-COO species [Fig. 4.3(b,c)] shows that the carboxylate is similar to a structure where a bent CO_2 molecule sits in an oxygen vacancy. As electron bombardment creates oxygen vacancies

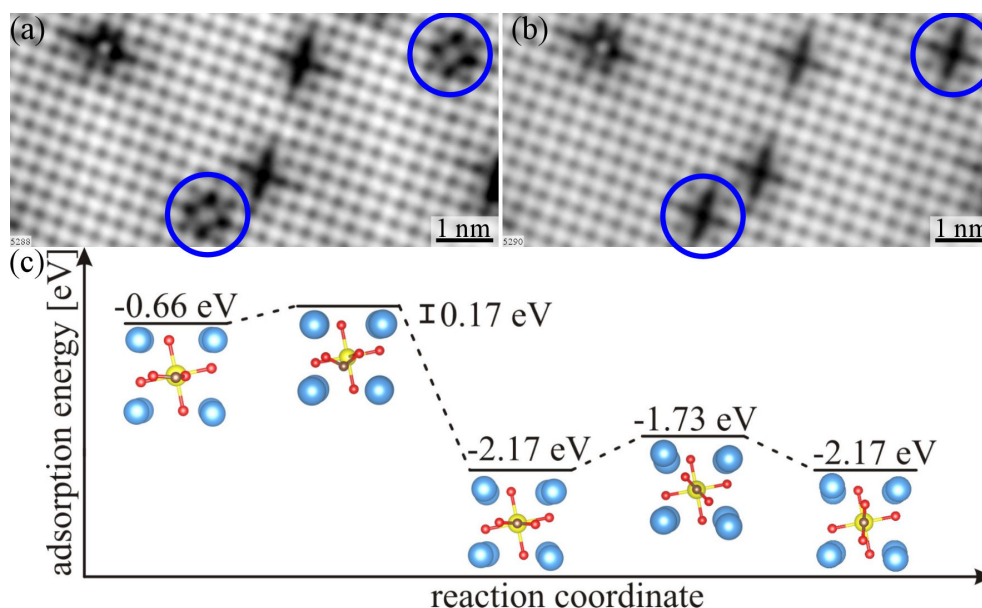


Figure 4.4: Transition from the CO-precursor to the CO-cross. (a) The CO-precursor molecules are marked with blue circles. (b) The two CO-precursor molecules transformed into CO-crosses after scanning with +1 V across the image area. (c) Energy diagram for the transition from the precursor via a transition state to the CO-cross. The carboxylate can be rotated by 90° via a second transition state ($E_{\text{act}} = 0.44$ eV). Color code: Sr (blue), Ru (yellow), O (red), C (brown). Scanning conditions: (a) 9.5×4.5 nm², $U_s = +0.2$ V, $I_t = 0.15$ nA, $T = 78$ K, (b) 9.5×4.5 nm², $U_s = +0.2$ V, $I_t = 0.15$ nA, $T = 78$ K.

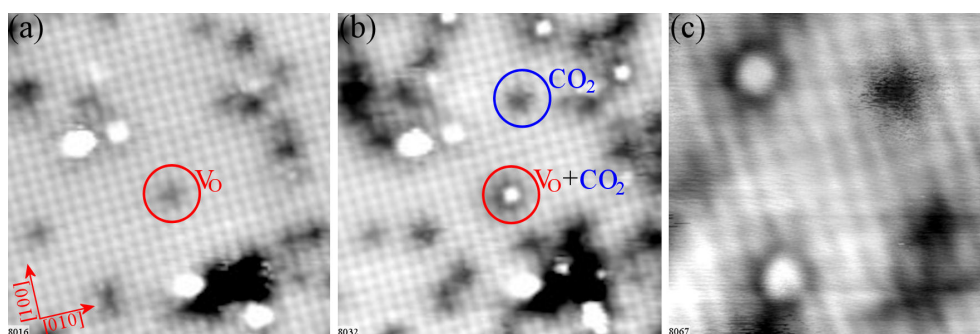


Figure 4.5: Reaction of CO_2 molecules with oxygen vacancies (V_O s). (a) Electron bombardment created several V_O s. (b) CO_2 molecules reacted with some oxygen vacancies (marked red). A CO_2 molecule adsorbed on a regular lattice site is marked in blue. (c) Zoomed-in image of the new V_O/CO_2 species. Scanning conditions: (a–c) $I_t = 0.15$ nA, $T = 78$ K, (a) 10×10 nm², $U_s = +0.05$ V, (b) 10×10 nm², $U_s = +0.1$ V, (c) 4.5×4.5 nm², $U_s = +0.4$ V.

on Sr_2RuO_4 and $\text{Sr}_3\text{Ru}_2\text{O}_7$ [see Section 3.5], we were able to directly observe the reaction of V_O s with CO_2 in STM. After bombarding the SrO surface of $\text{Sr}_3\text{Ru}_2\text{O}_7$ with electrons, several oxygen vacancies were created [Fig. 4.5(a), red circle]. Afterwards, 0.04 L CO_2 was dosed directly into the STM (78 K) and the same position on the sample was scanned again [Fig. 4.5(b)]. The CO_2 molecules randomly adsorbed on the clean surface [4.5(b), blue circle] and some molecules adsorbed on top of an V_O [Fig. 4.5(b), red circle]. The new features appear as big bright spot in STM [Fig. 4.5(c)], centered at the position of the apical oxygen atom. The obvious differences compared to CO adsorption on the clean surface have to be explained by a different adsorption behavior of the linear CO_2 molecule. It is imaginable that the CO_2 molecule does not adsorb in a C-down configuration, but with a O-down configuration and that an unknown activation energy prohibits the transformation into the carboxylate. Experimentally, this transformation could not be induced by scanning at higher bias voltages ($U_s = +3.0$ V); this rather caused diffusion of the $\text{V}_\text{O}/\text{CO}_2$ species. It is also unknown whether this activation barrier can be overcome by annealing the crystal to room temperature, due to the small amount of $\text{V}_\text{O}/\text{CO}_2$ species and the presence of CO molecules (from e-gun filament) contaminating the electron-bombarded SrO surface. Additionally, some further impurities can be found after bombarding the surface with electrons. It is difficult to judge how these impurities influence the surface quality after annealing to room temperature and whether they undergo reactions with the other species at the surface.

4.7 From single molecules to a full monolayer

4.7.1 Sticking Coefficient

As discussed above, CO reacts strongly with Sr_2RuO_4 and $\text{Sr}_3\text{Ru}_2\text{O}_7$ single crystals to form a Ru-COO complex, which is stable at room temperature. In the following section, we will investigate the sticking coefficient of CO on Sr_2RuO_4 and $\text{Sr}_3\text{Ru}_2\text{O}_7$ at different conditions to better characterize this high activity.

Figure 4.6(a–c) describes the adsorption behavior of CO on Sr_2RuO_4 at

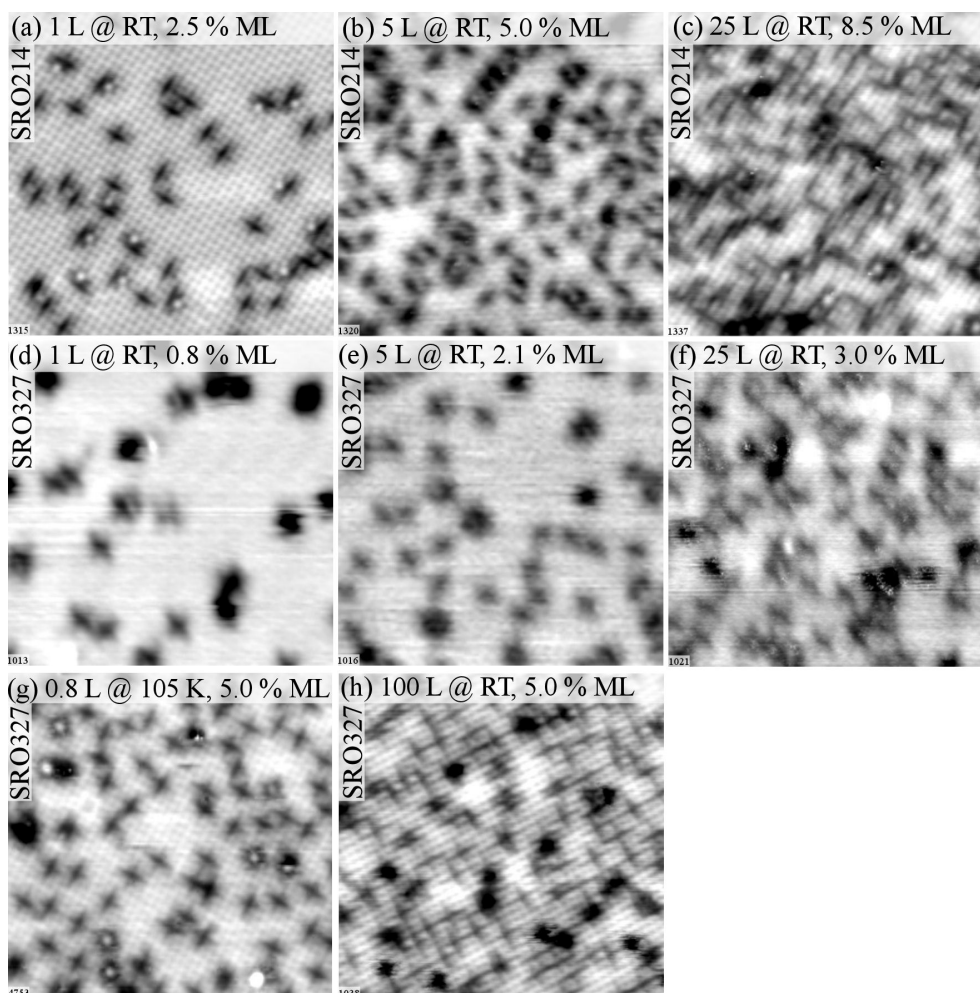


Figure 4.6: Different CO-coverages on Sr_2RuO_4 and $\text{Sr}_3\text{Ru}_2\text{O}_7$. (a–f) CO exposure at room temperature: The uptake on Sr_2RuO_4 (a–c) is about 2-3 times higher than on $\text{Sr}_3\text{Ru}_2\text{O}_7$ (d–f). On $\text{Sr}_3\text{Ru}_2\text{O}_7$ a coverage of 0.005 ML is achieved if the surface is exposed to either 0.8 L at 105 K (g), or to 100 L at room temperature (h). Side note: After cleaving the Sr_2RuO_4 single crystal, a few water molecules were present on the as-cleaved surface. The bright spots next to some CO-crosses in (a) indicate an interaction of water with CO. All STM images: $15 \times 15 \text{ nm}^2$, $T = 78 \text{ K}$.

	T [K]	Dose [L]	$\hat{=}$ %ML	Sticking Coefficient
Sr ₂ RuO ₄	300	1	2.5	0.053
	300	5	5.0	0.021
	300	25	8.5	0.007
Sr ₃ Ru ₂ O ₇	300	1	0.8	0.017
	300	5	2.1	0.009
	300	25	3.0	0.003
	300	100	5.0	0.001
	105	0.8	5.0	0.131

Table 4.1: Coverage and sticking coefficient of CO at different doses and temperatures on Sr₂RuO₄ and Sr₃Ru₂O₇. See Fig. 4.6.

room temperature (RT). After dosing 1 L, 5 L and 25 L of CO, 2.5 %, 5 % and 8 % of the surface oxygen atoms reacted with the CO to form a carboxylate. Thus, the sticking coefficient decreases from initially 0.053 (1 L dosed) to 0.007 (25 L dosed) [see Table 4.1].

Exactly the same experiment was repeated under the same conditions for Sr₃Ru₂O₇ [see Fig. 4.6(d-f)]. The sticking coefficient decreases also on this system from initially 0.017 (1 L dosed) to 0.003 (25 L dosed) [see Table 4.1]. This shows that the initial sticking coefficient on Sr₃Ru₂O₇ is drastically lower than on Sr₂RuO₄. The absence of a precursor on Sr₂RuO₄ might explain the differences between these two similar systems, as on Sr₃Ru₂O₇ some adsorbed CO-precursor might desorb immediately and do not transform into the carboxylate.

To test for the influence of the adsorption temperature, we also dosed CO onto a cold sample (105 K). After dosing 0.8 L of CO at 105 K about 5 % ML was covered with CO, pointing out an increase of the sticking coefficient (\sim factor 10) [see Fig. 4.6(g,h), Table 4.1]. To achieve a similar coverage, about 100 L of CO has to be dosed at room temperature [Fig. 4.6(h)].

4.7.2 Saturation Coverage of CO

In the previous subsections we showed that the sticking coefficient strongly depends on the sample temperature and on the CO coverage. Thus, to achieve a high CO coverage, exposure at low temperatures is necessary. To avoid contaminating our preparation chamber, we used a directional doser,

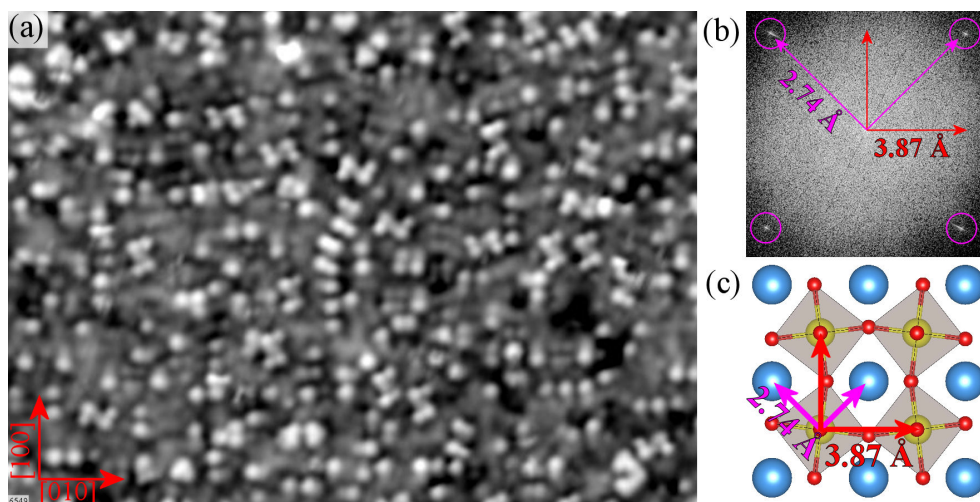


Figure 4.7: Saturation Coverage of CO. (a) ~ 50 L CO dosed at 105 K on $\text{Sr}_3\text{Ru}_2\text{O}_7$. The entire surface is covered with CO. (b) In the FFT no sign of the lattice can be observed (lattice vector: 3.87 \AA , red arrows). However, four spots in the FFT indicate a periodicity of 2.74 \AA (pink arrows). (c) The structure model of the surface layer illustrates the distances of 3.87 \AA and 2.74 \AA . Scanning conditions: (a) $14 \times 10 \text{ nm}^2$, $U_s = +0.3 \text{ V}$, $I_t = 0.15 \text{ nA}$, $T = 78 \text{ K}$.

consisting of a tube with a shower-like head at the end. This way the CO pressure at the sample should be about 10 times higher than the pressure read by the ion gauge. We exposed the cold $\text{Sr}_3\text{Ru}_2\text{O}_7$ single crystal to ~ 50 L of CO using this experimental setup. The STM image shows some short-range ordered structures [Fig. 4.7], however, no long-range ordering could be observed. The FFT of this STM image [inset Fig. 4.7] reveals four weak spots corresponding to a lattice vector of 2.74 \AA (pink arrows). The lattice spots of the tetragonal unit cell (3.87 \AA) are not visible. If this 2.74 \AA periodicity is caused by the adsorbed CO molecules, CO molecules have to adsorb not only on the apical oxygen atoms but also on the Sr atoms.

However, to better characterize the full monolayer of CO, further experiments are needed, where the CO coverage is increased step by step to the saturation coverage. As mentioned previously XPS measurements were not performed to characterize the adsorption of CO, due to the small sample size and the overlap of the C 1s and the Ru 3d peaks.

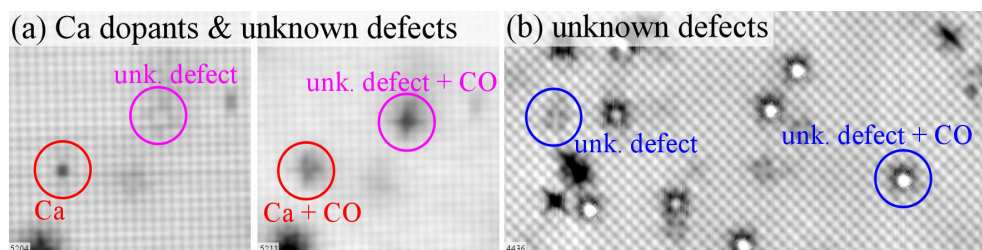


Figure 4.8: CO interacting with defects. (a) Repetition of Fig. 4.1(a,b). Two STM images of the same area before and after adsorbing CO: CO interacts with Ca (red circle) and an unknown defect (pink circle). (b) CO interacts with another unknown defect (blue circle). Scanning conditions: (a) $10 \times 10 \text{ nm}^2$, $U_s = +0.05 \text{ V}$, $I_t = 0.15 \text{ nA}$, $T = 78 \text{ K}$, (b) $20 \times 10 \text{ nm}^2$, $U_s = +0.5 \text{ V}$, $I_t = 0.15 \text{ nA}$, $T = 78 \text{ K}$.

4.8 Interaction with defects

In Section 4.2 we showed that CO adsorbs first at some defects, before it adsorbs on the clean surface. This initial adsorption is once again shown in Fig. 4.8 (a). The Ca dopant (marked with a red circle) interacts with CO to form a cross-like feature next to the Ca dopant. An unknown (unk.) defect (marked with a pink circle) interacts with CO to form also a cross-like feature. As we have shown in Section 4.4 CO likes to interact with the Ru atom of the subsurface layer to form a Ru-COO species, which appears in STM as a dark cross. It is quite likely that at these defects no CO-precursor exists, that a Ru-carboxylate is formed at the Ca defect and an unknown carboxylate at the unknown defect. According to the trace analysis (see Section 3.3) these defects could be Al, Cr, Fe or Ni. Fig. 4.8(b) illustrates the interaction of CO with another unknown defect at a Ru site. If CO reacts with the unknown defect (marked with a blue circle) a bright spot appears in the STM image. After annealing the crystal to room temperature, all these white spots are gone, suggesting that the CO either interacted with these defects to form a carboxylate or desorbed once again.

4.9 Interaction with water

In Section 3.6 we showed that, after cleaving Sr_2RuO_4 single crystals at room temperature, small amounts of water can be observed on the freshly cleaved crystal [see Fig. 4.9(a), marked with red circles]. In STM water monomers

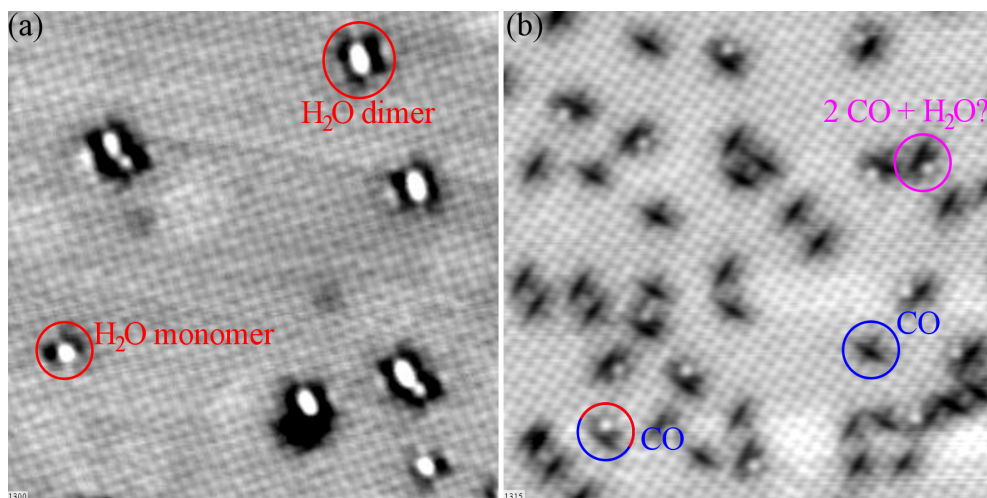


Figure 4.9: Interaction of CO with water on Sr₂RuO₄. (a) After cleaving a few water molecules were present on the surface (red circle). (b) Every water molecule interacted with adsorbed CO molecules forming an unknown complex (mixed-colored circle). In some cases two CO molecules may interact with one water molecule (pink circle). CO also adsorbs on the clean surface (blue circle). Scanning conditions: (a,b) $15 \times 15 \text{ nm}^2$, $I_t = 0.15 \text{ nA}$, $T = 78 \text{ K}$, (a) $U_s = +0.3 \text{ V}$, (b) $U_s = +0.8 \text{ V}$.

and water multimers appear as bright spots or bright chains [see Section 5.2, 5.3]. After dosing 1 L CO at 300 K onto such a water-covered surface the regular water crosses centered on an apical oxygen atom and new features are observed [see Fig. 4.9(b), blue/red circle]. These new features consist of a dark cross-like feature and a bright spot next to it, which might indicate that the CO molecules reacted with the water molecules to form a new complex. The exact adsorption configuration of this species is unknown at this point, but should be investigated in the future.

4.10 Tip-induced Desorption

4.10.1 CO - Low Coverage

Due to the high adsorption energy ($E_{\text{ads}} = 2.2 \text{ eV}$), CO does not desorb at room temperature. Thus, once contaminated, a clean surface could not be regained in our experiment. However, we observed that the surface can be cleaned locally from CO by manipulating the CO molecules with the STM. A general discussion of STM manipulation is found in section 2.4.4. Since

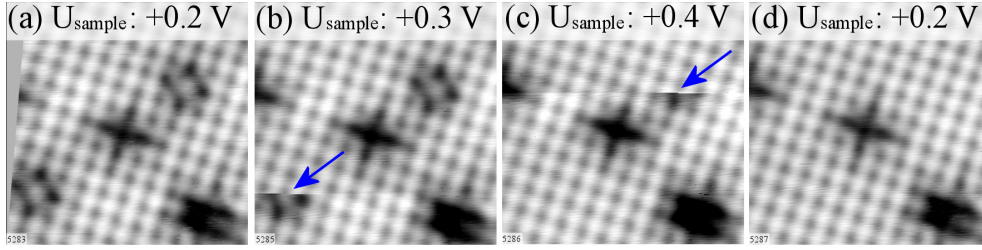


Figure 4.10: Tip-induced desorption of the CO-precursor from $\text{Sr}_3\text{Ru}_2\text{O}_7$. (a) $U_s = +0.2$ V, the precursors are stable. (b) $U_s = +0.3$ V, the first precursors desorb during scanning (blue arrow). (c) $U_s = +0.4$ V, the second precursor desorbs during scanning (blue arrow). (d) $U_s = +0.2$ V, both precursors are gone. Scanning conditions: (a–d) 4.5×4.5 nm², $I_t = 0.15$ nA, $T = 78$ K. (a) $U_s = +0.2$ V (b) $U_s = +0.3$ V (c) $U_s = +0.4$ V (d) $U_s = +0.2$ V.

U_s , I_t and the tip-sample distance cannot be changed independently, it would necessitate further experiments to figure out if the electric field between sample and tip, or if electrons tunneling between the tip and the sample cause the observed effects.

In the case of the CO-precursor we found out that scanning at $U_s = \pm 0.3$ V, $I_t = 0.15$ nA causes the precursor to desorb [Fig. 4.10(a–d)]. Possibly, the weakly-bound precursor desorbs via excitations of stretching vibrations through inelastic tunneling. The DFT calculations indicate a molecule-surface vibrational mode at ~ 120 meV [64], which is roughly consistent with the observed desorption parameters. Possibly, the process might be also related to the C-O stretch frequency (typically ~ 270 meV for adsorbed CO [73]).

To desorb the carboxylate, we scanned across the marked area in Fig. 4.11(a) twice with $U_s = +2.8$ V, $I_t = 0.015$ nA. At these conditions only few desorption processes could be observed (10 in total, 4.11(b)). However, several CO crosses rotated by 90° [see Fig. 4.11(d,e)]. After increasing the tunneling current by a factor of 3.3 to $I_t = 0.05$ nA, about 30 CO molecules desorbed [Fig. 4.11(c)]. If the desorption-process is a one-electron process [equation 2.14], then the number of desorption processes should increase linearly with increasing tunneling current. In our case, however, after increasing the tunneling current by a factor of 3.3 the amount of desorbed CO increased by a factor of 6. These differences could be explained by our limited data set or by the possibility that the electric field also affects the desorption of the carboxylate as shown below.

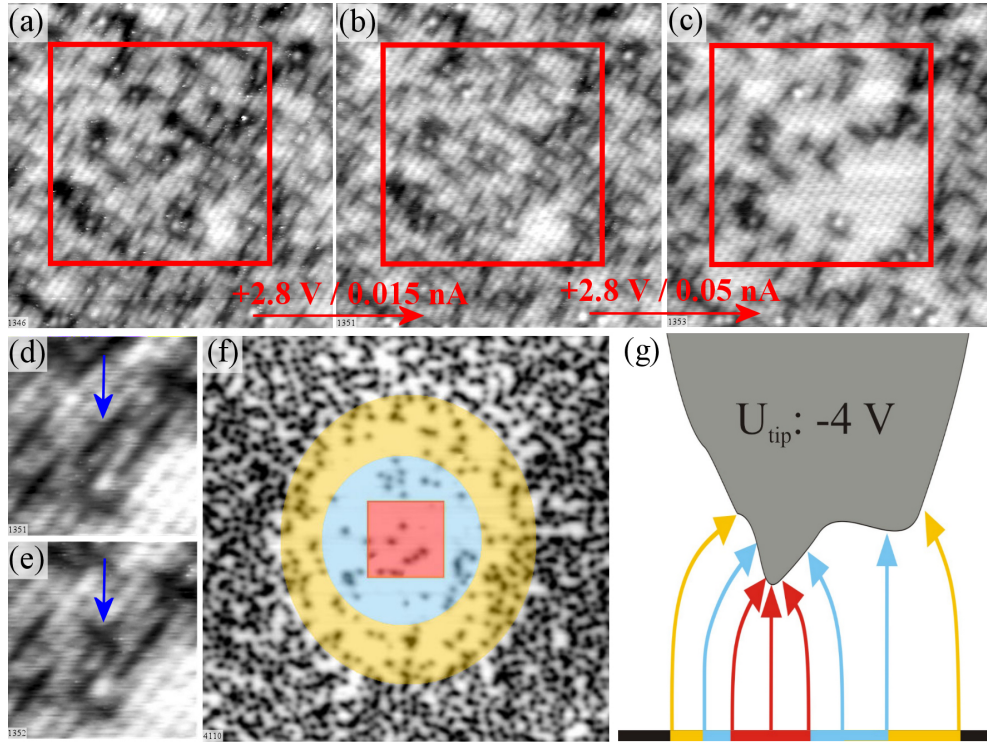


Figure 4.11: Tip-induced desorption of the CO-cross from Sr_2RuO_4 (a–c) and $\text{Sr}_3\text{Ru}_2\text{O}_7$ (d). (a) Starting point. (b) After scanning across the marked area twice with $U_s = +2.8$ V, $I_t = 0.015$ nA, about 10 carboxylates disappeared. Many carboxylates rotated by 90° . (c) After scanning across the marked area with $U_s = +2.8$ V, $I_t = 0.05$ nA more carboxylates desorbed (about 30). (d,e) The CO cross in the center of the STM image (blue arrow) rotates, after scanning across the area with $U_s = +2.8$ V, $I_t = 0.015$ nA (f) The red marked area was scanned with $U_s = +4.0$ V, $I_t = 0.15$ nA. CO also desorbed from the area which was not scanned. This can be explained by a finite extension of the STM tip [see Fig.(g)]. Scanning conditions: (a) 15×15 nm², $U_s = -0.02$ V, $I_t = 0.15$ nA, $T = 78$ K, (b) 15×15 nm², $U_s = +0.05$ V, $I_t = 0.15$ nA, $T = 78$ K, (c) 15×15 nm², $U_s = +0.1$ V, $I_t = 0.15$ nA, $T = 78$ K, (f) 53×53 nm², $U_s = +1.5$ V, $I_t = 0.15$ nA, $T = 78$ K. Fig. (g) Based on [74].

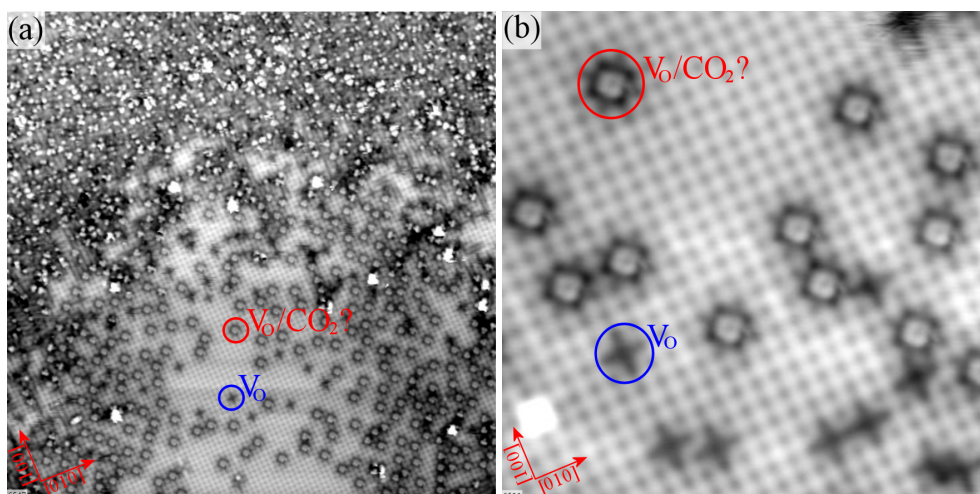


Figure 4.12: Saturation coverage of CO – tip-induced desorption. (a) After scanning a small area with $U_s = +4$ V, $I_t = 0.15$ nA and $U_s = +5$ V, $I_t = 0.15$ nA CO was removed from the scanned and surrounding area. (a,b) In the clean area new features appear, which can be identified as oxygen vacancies (marked with a blue circle) and, possibly, V_O/CO_2 complexes (marked with a red circle). Scanning conditions: (a,b) $U_s = +0.3$ V, $I_t = 0.15$ nA, $T = 78$ K, (a) 37×37 nm², (b) 9×9 nm².

At bias voltages above +2.8 V, CO is not only removed from the scanned area, but also from the surrounding area [Fig. 4.11(g)]. After scanning the red area (10×10 nm²) with $U_s = +4.0$ V, CO also desorbed from the blue and yellow area, which was not scanned. This desorption behavior is characteristic for a field-induced desorption, where the field strength varies underneath a STM tip of finite size [see Fig. 4.11(g)]. The strength of the electric field between tip and sample decreases much slower ($1/r$) than the tunneling current ($1/e^{-2\kappa r}$) with increasing tip-sample distance and will therefore affect CO from an area that was not scanned.

DFT predicts that the lowest antibonding O-C-O molecular orbital of the carboxylate is centered around +2.4 eV [64]. A detailed analysis of the orbital (wave function) phase factors shows that both, the O-CO bond and the Ru-C bond get weakened. Thus, the carboxylate is most likely desorbed by electron capture into antibonding orbitals at scanning conditions such as $U_s = +2.8$ V, $I_t = 0.015$.

4.10.2 Desorption of CO at High Coverage

Figures 4.12(a,b) shows the tip-induced desorption of CO molecules, starting with the entire surface covered with CO [see Section 4.7.2]. After scanning a small area first with $U_s = +4$ V, $I_t = 0.15$ nA and then $U_s = +5$ V, $I_t = 0.15$ nA, most of the CO from the scanned and the surrounding areas was removed. However, two features were observed on the cleaned area. These features were discussed in previous sections (Section 4.6). We find small, dark crosses that can be identified as oxygen vacancies [compare with Fig. 4.5(a)] and big, bright spots that can be identified as a V_O/CO_2 complex [compare with Fig. 4.5(c)]. It is important to note that on the clean surface scans up to $U_s = +7$ V, $I_t = 0.15$ nA have no effect on the scanned area. It seems that under these tunneling conditions a transformation from the carboxylate to the V_O/CO_2 species took place. The occurrence of oxygen vacancies might be explained by removing the CO_2 from the V_O/CO_2 complex, leaving behind a V_O on the surface.

4.11 Conclusion

The experimental and computational results clearly show a strong interaction between CO and strontium ruthenate perovskites. Thus, this reaction needs to be taken into account even for experiments under the most pristine conditions. So far, very little had been known about the exact adsorption behavior of CO on perovskite (ABO_3) surfaces.

To get a feeling of the influence of the A site, one can compare the CO adsorption on different earth alkali oxides, as reviewed in Ref. [75]. The reactivity increases with basicity¹ of the oxide, i.e., $MgO < CaO < SrO$. A reaction between lattice O and CO was postulated as the first step of CO polymerization. This process might be the O-C-O species identified in this work.

To characterize the influence of the B-site, it is instructive to compare the CO adsorption on Sr_2RuO_4 and $Sr_3Ru_2O_7$ with binary transition metal oxides. On $RuO_2(110)$, CO adsorbs at the undercoordinated Ru atoms, reacts with

¹Lewis definition: A solid is basic if it is able to donate an electron pair to an acidic probe molecule.

the neighboring bridging oxygen atom and desorbs as CO_2 [76]. $\text{TiO}_2(110)$, which has the same structure, is less reactive and CO adsorbs only weakly below 200 K [77]. A similar weak interaction of CO with SrTiO_3 was reported [78], however, as pointed out before, the surface termination of such sputtered and annealed perovskite samples is often not well-defined.

Preliminary results show that CO does not only react strongly with the clean surface layer, but can also interact with water molecules. Thus, the adsorption of CO and the interaction of CO with other molecules could easily explain “surface-degradation” effects reported on high T_c superconductors [79, 80], as well as “aging” effects and cleaving-temperature depended surface properties of Sr_2RuO_4 observed in ARPES measurements [24, 61, 62].

Chapter 5

Adsorption of H₂O

5.1 Introduction

The interaction of water with metal and metal oxides is a key aspect for several fields of material science, including corrosion science, photo catalysis and heterogeneous catalysis [83–85]. Especially in the catalytic context, the question whether water adsorbs dissociatively or molecularly on oxide surfaces is of great importance, since the dissociation of water is the first step of hydrogen production from water [86]. MgO is one of the prototype materials where water adsorption has been investigated theoretically and experimentally. General agreement exists that water adsorbs molecularly [81, 87, 88] on the clean surface unless defects are present. At higher coverages an ordered monolayer forms, which consists of dissociated and intact water molecules.

Xiao Liang Hu *et al.* [81, 88] investigated by DFT calculations how the water adsorption changes along the MgO, CaO, SrO, BaO series coming to the result that the lattice constant and rumpling of the surface are the two main parameters, which decide whether water adsorbs molecularly or dissociatively. On MgO water adsorbs molecularly on top of the Mg atom [see Fig. 5.1(a), Type I]. On CaO, SrO and BaO water adsorbs dissociatively [see Fig. 5.1(a), Type IV]. Type II describes the energetically less favorable molecular adsorption of a single H₂O molecule on CaO, SrO and BaO, and Type III describes the water adsorption on CsF and RbF. With increasing lattice constant from 4.25 Å (MgO) to 5.61 Å (BaO) the adsorption energy for both molecular and dissociative adsorption decreases (i.e, more stable

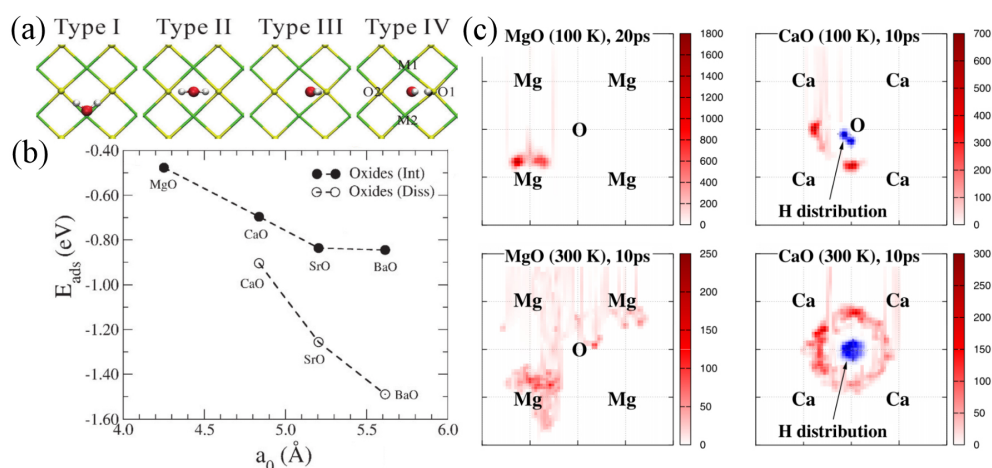


Figure 5.1: Water adsorption on earth alkali oxides. (a) Type I: Molecular adsorption on MgO, Type II: Molecular adsorption on CaO, SrO and BaO, (Type III: Adsorption on CsF and RbF), Type IV: Dissociated adsorption on CaO, SrO and BaO. (b) Adsorption energies of the most stable intact and dissociated single water molecules on MgO, CaO, SrO and BaO. (c) AIMD simulations at 100 K and 300 K. The positions of the H_2O oxygen atom and H_{ads} are marked with red and blue spots, respectively. (a,b) Figures reprinted with permission from [“Trends in water monomer adsorption and dissociation on flat insulating surfaces”, Hu *et al.*, Phys. Chem. Chem. Phys., **13**, 12447, (2011)], [81]. Copyright © 2014 by Royal Society of Chemistry. (c) Figures reprinted with permission from [“Dynamic Ion Pairs in the Adsorption of Isolated Water Molecules on Alkaline-Earth Oxide (001) Surfaces”, Carrasco *et al.*, Phys. Rev. Lett., **100**, 016101, (2008)], [82]. Copyright © 2014 by American Physical Society.

adsorption). The adsorption energy for dissociative adsorption decreases even faster than that for the molecular configuration, which leads to a favored dissociative adsorption for CaO, SrO and BaO [see Fig. 5.1(b)]. This finding is in agreement with further DFT studies, which predict a dissociative adsorption of water on CaO [82] and BaO [89]. Interestingly, for these two systems the dissociated water molecules do not dissociate completely but still interact via hydrogen bonds. Carrasco *et al.* performed a series of DFT calculations complemented by *ab initio* molecular dynamics (AIMD) simulations to investigate the properties of isolated water molecules on MgO and CaO. AIMD simulations show that while the water molecule on top of the MgO atom shows no diffusion at 100 K and almost no diffusion at 300 K, the $(\text{OH})_{\text{ads}}$, which sits on a Ca-Ca bridge, can move from one bridge to another at 100 K and at 300 K [see Fig. 5.1(c)]. Due to the interaction between the two dissociated $(\text{OH})_{\text{ads}}$ and $\text{O}_s\text{H}_{\text{ads}}$ Carrasco *et al.* called the dissociated hydroxyls “dynamic ion pairs”.

A very good tool to investigate the adsorption behavior of single molecules is scanning tunneling microscopy. However, due to their large band gap, bulk earth alkali oxides are not suitable for STM measurements. To overcome this problem, thin films of MgO were grown on Ag(100) confirming a molecular adsorption [87].

Whereas the interaction of water with binary oxides has been investigated quite intensively so far, little is known about the interaction of water with more complex ternary oxides, despite their use in catalysis. The main reason why little data about water adsorption on perovskites exist is the difficulty to experimentally prepare perfect, well-defined surfaces. In the case of SrTiO₃(001) it was predicted that water should dissociate on the SrO terminated surface in a similar way as reported for the earth alkali oxides.

As Sr₃Ru₂O₇ and Sr₂RuO₄ single crystals are metallic and thus suitable for STM investigation, they are the perfect material for investigating water adsorption on perovskites. We will show in the following section that water will adsorb in the same way as predicted for SrTiO₃. In addition we will show experimental proof for the formation of “dynamic ion pairs” on the SrO surface of Sr₂RuO₄ and Sr₃Ru₂O₇, as we observed a hopping of the $(\text{OH})_{\text{ads}}$ around the $\text{O}_s\text{H}_{\text{ads}}$ from one Sr-Sr bridge to another Sr-Sr bridge.

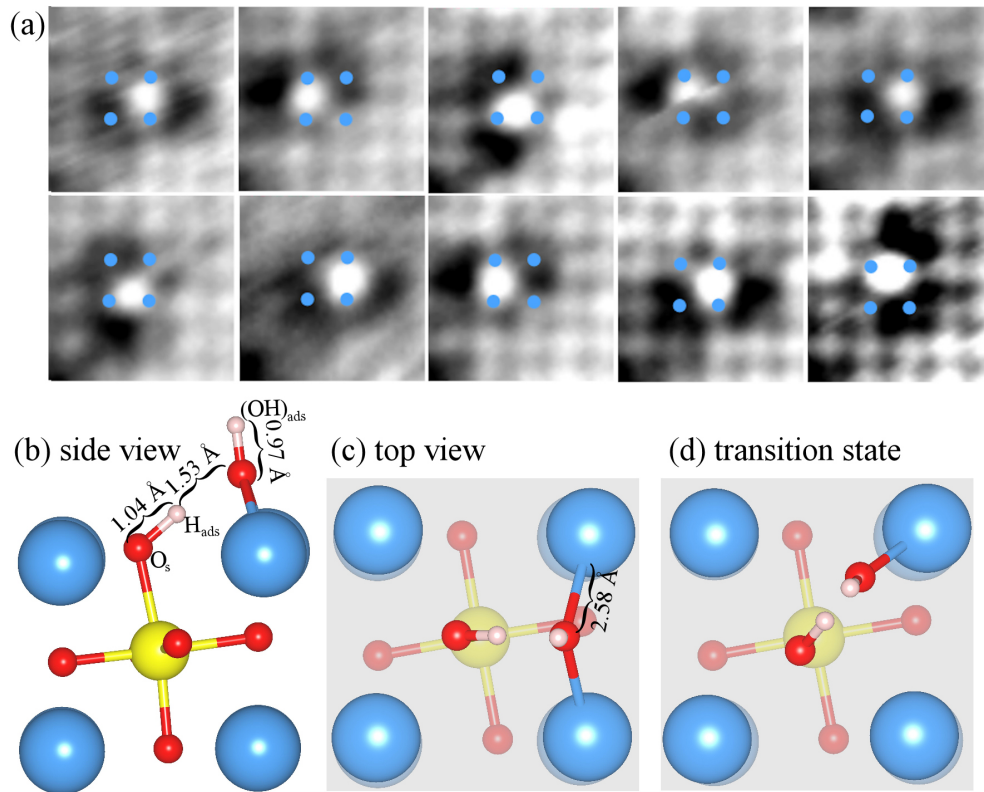


Figure 5.2: Water adsorption on SrO terminated $Sr_3Ru_2O_7$. Water dissociates on the clean, defect-free surface, but the resulting hydroxyls do not separate. (a) $(OH)_{ads}$ on a Sr-Sr bridge site appears bright in STM. This hydroxyls can jump around the H_{ads} that formed a hydroxyl with the O_s . (b,c) Side and top view of the calculated adsorption configuration [64]. (d) Transition state. The activation energy needed to move an $(OH)_{ads}$ from one Sr-Sr bridge site via the transition state to a neighbouring bridge site is $E_{act} = 0.18$ eV [64]. Color code: Sr (blue), Ru (yellow), O (red), H (white).

5.2 Monomers

To investigate the adsorption of H_2O on Sr_2RuO_4 and $Sr_3Ru_2O_7$ we cooled the manipulator to 105 K in the preparation chamber and exposed the crystal to 0.05 L H_2O . Afterwards the cold sample was put into the STM and measurements at 78 K followed. In STM new features, positioned at a Sr-Sr bridge site, appear after dosing H_2O [see Fig. 5.2(a)]. To better visualize the adsorption site, four blue spots are drawn in this image, marking the same four position of the Sr atoms in all images.

DFT calculations predict a slightly stronger adsorption energy ($E_{ads} = -1.26$ eV) for the dissociative configuration compared to the molecular

adsorption ($E_{\text{ads}} = -1.08$ eV) [64]. The geometry of the adsorbed water fragments is shown in Fig. 5.2(b,c). In this configuration two different types of hydroxyls form: One hydroxyl, $(\text{OH})_{\text{ads}}$, adsorbs in a Sr-Sr bridge with an Sr-O distance of 2.58 Å. The remaining H is transferred to a neighboring surface oxygen atom and forms a second hydroxyl $\text{O}_s\text{H}_{\text{ads}}$. The OH bond length of the $(\text{OH})_{\text{ads}}$ is slightly smaller (0.97 Å) than the bond length of the $\text{O}_s\text{H}_{\text{ads}}$ bond (1.04 Å). The $\text{O}_s\text{H}_{\text{ads}}$ is tilted towards the $(\text{OH})_{\text{ads}}$ to form a hydrogen bond between both hydroxyls, with a distance of 1.53 Å. The DFT calculations also predict that only the $(\text{OH})_{\text{ads}}$ should be visible in STM, which is in agreement with the experimental results.

Consecutive STM images of the same sample area [see Fig. 5.2(a)] reveal that the $(\text{OH})_{\text{ads}}$ is mobile on the surface at 78 K. The $(\text{OH})_{\text{ads}}$ is able to jump from one Sr-Sr bridge to another. The $(\text{OH})_{\text{ads}}$ cannot move freely on the surface, however, it is trapped by the hydrogen bond between the $(\text{OH})_{\text{ads}}$ and H_{ads} , resulting in a rotation around the $\text{O}_s\text{H}_{\text{ads}}$. Thus each $(\text{OH})_{\text{ads}}$ can sit on four different Sr-Sr bridge sites. The predicted activation energy is rather small ($E_{\text{act}} = 0.18$ eV), confirming the observed hopping at low temperatures. To minimize the possibility that the observed hopping is tip induced, we scanned at very low currents (40 pA) and changed the scanning angle. At these conditions the water hopping could still be observed.

As mentioned above, a similar adsorption behavior was already predicted on CaO and BaO, as Carrasco *et al.* predicted the formation of “dynamic ion pairs” on CaO [82] [see Fig. 5.1(c)] and Grönbeck and Panas on BaO [89].

5.3 Dimers

Figures 5.3(a,b) illustrate the SrO surface of $\text{Sr}_3\text{Ru}_2\text{O}_7$ and Sr_2RuO_4 after dosing 0.045 L H_2O and 0.05 L H_2O , respectively. In both cases not only monomers (marked with a red circle) are found, but also a few dimers (marked with a blue circle). Interestingly, the $c(2\times 2)$ surface structure, caused by the rotation of the RuO_6 octahedra influences the configuration of the dimers. Due to the clockwise and counterclockwise rotation of the RuO_6 octahedra two subsurface oxygen atoms of two neighboring octahedra in the RuO_2 plane are either 4.7 Å or 3.3 Å apart. Thus, the center of a dimer (middle

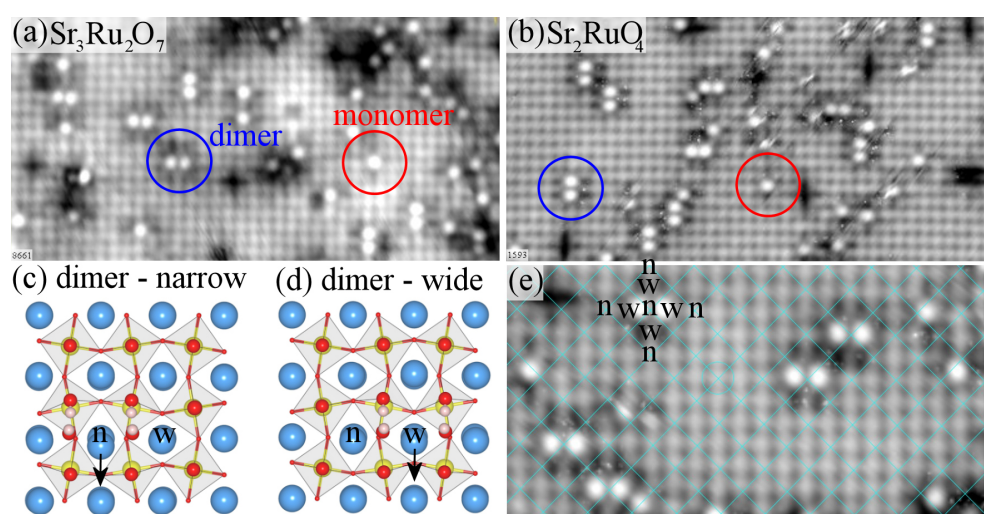


Figure 5.3: Dimer formation on $Sr_3Ru_2O_7$ and Sr_2RuO_4 . (a,b) A water monomer and dimer is marked with a red and a blue circle, respectively. After the formation of dimers, jumping of the $(OH)_{ads}$ is no longer observed. (c,d) The dimer formation depends on the rotation of the RuO_6 octahedra. Due to the rotation “narrow” and “wide” sides form where two neighboring oxygen atoms in the RuO_2 plane are either 3.3 Å or 4.7 Å apart. (e) Under the assumption that the crossing points of the grid lines are centered on “narrow” sites, the “wide” site have to be in the center of the grid. Only “narrow” dimers are observed. Scanning conditions: (a,b) $15 \times 7.5 \text{ nm}^2$, $I_t = 0.15 \text{ nA}$, $T = 78 \text{ K}$, (a) $U_s = +0.01 \text{ V}$, (b) $U_s = +0.5 \text{ V}$.

between two $(\text{OH})_{\text{ads}}$ can either be located on a “narrow” (n) or “wide” (w) site [see Fig. 5.3(c,d)]. Experiments show that just one of these dimers is formed [see Fig. 5.3(e)]. Unfortunately, based on our STM images, we cannot determine whether the narrow or wide dimer is preferred. It has to be noted that the notation “wide” and “narrow” site only refers to the distance of the oxygen atoms in the RuO_2 plane, not to the surface layer.

DFT predicts a dimer preferred at a “narrow” site is indeed energetically more favorable than one at a “wide” site. The difference in binding energy, ΔE , is 80 meV [64]. This energy difference might be explained by the interaction between the distorted Sr atom between two $(\text{OH})_{\text{ads}}$ and their surrounding RuO_6 octahedra: In the case of dimers on the “narrow” site the Sr atom between two $(\text{OH})_{\text{ads}}$ is moved **with** the RuO_6 octahedra rotation direction and in the case of dimers on the “wide” site the RuO_6 octahedra are moved **against** the rotation direction. With other words, in the “narrow” configuration the Sr atom has more space to move away from the $\text{O}_s\text{H}_{\text{ads}}$ than in the “wide” configuration [see Fig 5.3(c), black arrows].

5.4 Multimers

After dosing 0.045 L H_2O at 105 K we mostly observed water monomers and just a few water dimers [see Fig. 5.3(a,b)]. Larger clusters were usually not observed at low coverages, presumably due to kinetic barriers. To overcome such a barrier we annealed our samples to room temperature for one hour after first exposing it to 0.05 L H_2O . This caused the water molecules to form 2D multimers along the [100] and [010] direction. Due to symmetry reasons there is no difference between the horizontal and vertical chains. Thus, we will only focus on one type of chains, namely the horizontal chains. In the energetically most favorable dimer configuration the $(\text{OH})_{\text{ads}}$ are not located perfectly on the Sr-Sr bridge site, but are shifted towards the $\text{O}_s\text{H}_{\text{ads}}$ [see Fig. 5.3(c)]. A similar shift can be observed for longer chains, as the chain marked by a red/blue rectangle [see Fig. 5.4(a)] is partly shifted to the bottom and partly to the top. A chain consisting of two dimers next to each other, where one is shifted to the top and one is shifted to the bottom, is marked by the mixed-colored rectangle [see Fig. 5.4(a)].

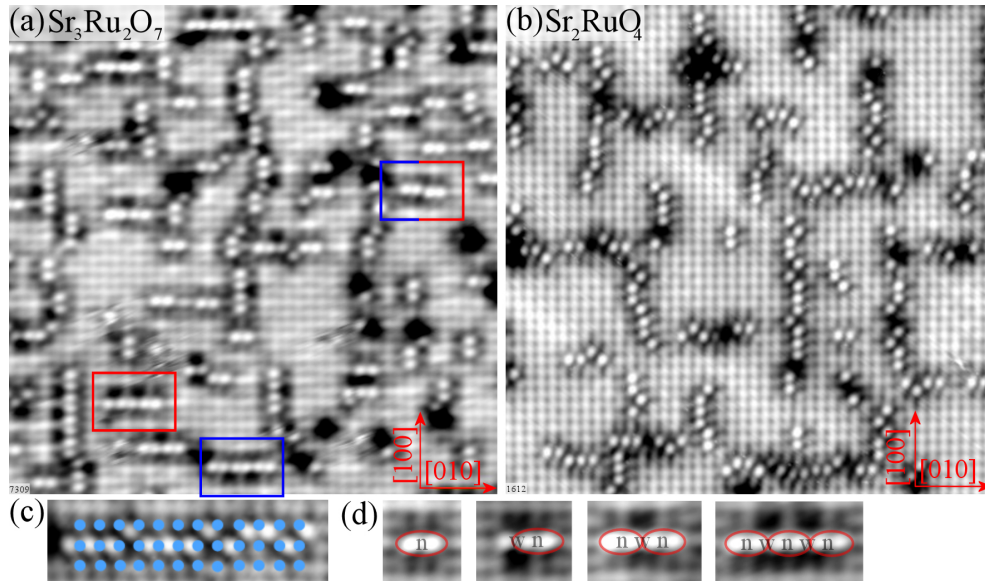


Figure 5.4: Water multimer formation on $Sr_3Ru_2O_7$ and Sr_2RuO_4 . After annealing to room temperature 2D water multimers formed. (a) The chains are oriented along the $[100]$ and $[010]$ direction. They are not perfectly centered on the Sr-Sr bridge site. The chains marked by red and blue frames are shifted to the bottom and top, respectively. (b) The chains on Sr_2RuO_4 are not as perfectly straight as on $Sr_3Ru_2O_7$. (c) Thirteen water molecules forming a chain on Sr_2RuO_4 . The blue spots mark the position of the underlying Sr atoms, illustrating that the 5 top bright spots are shifted by one lattice constant to an opposite Sr-Sr bridge. (d) Four cutouts of STM images, showing a water dimer, trimer, tetramer and hexamer. Dimers centered on a “narrow” site are marked with a red ellipse. Even-numbered multimers contain more “narrow” than “wide” sites. Scanning conditions: (a,b) $17.3 \times 17.3 \text{ nm}^2$, $I_t = 0.15 \text{ nA}$, $T = 78 \text{ K}$, (a) $U_s = +0.7 \text{ V}$, (b) $U_s = +0.5 \text{ V}$.

Apart from the shifts, all chains are perfectly straight on $\text{Sr}_3\text{Ru}_2\text{O}_7$. The water chains on Sr_2RuO_4 have some kinks, however [see Fig. 5.4(b)]. Some of the white spots $(\text{OH})_{\text{ads}}$ are located on an opposite Sr-Sr bridge [see Fig. 5.4(c)]. This difference is most likely caused by a slightly different surface structure. It is also possible that, at higher water coverages, the $c(2\times 2)$ reconstruction of Sr_2RuO_4 , which influences the water adsorption, is lifted. In contrast, the “ $c(2\times 2)$ ” symmetry of $\text{Sr}_3\text{Ru}_2\text{O}_7$ is a property of the bulk lattice.

A closer look at the trimers, tetramers, etc. reveal that the formation of chains also depends on the $c(2\times 2)$ surface structure, caused by the rotation of the RuO_6 octahedra [see Fig. 5.4(d)]. Starting from a water dimer centered on a “narrow” site, the third water molecule can adsorb either on the left or on the right side. However, for water trimers a fourth water molecule always adsorbs in a way that the tetramer consists of two stable water dimers centered on two “narrow” sites, and not of two dimers on “wide” sites. This is also true for hexamers, which consist of three dimers on “narrow” sites. It is likely that all even-numbered water multimers consist of stable water dimers on “narrow” sites, i.e. contain more “narrow” than “wide” sites.

5.5 Higher coverage

To achieve a higher-coverage of water, we dosed 1 L of H_2O at 150 K on $\text{Sr}_3\text{Ru}_2\text{O}_7$ and Sr_2RuO_4 [see Fig. 5.5(a,b)]. As for the chain formation, the behavior of the high coverage layer is slightly different for $\text{Sr}_3\text{Ru}_2\text{O}_7$ and Sr_2RuO_4 . In both cases the STM images show bright lines (similar to the lines observed at low-coverages, see Fig. 5.4(a,b)). In addition to these lines, some ordered areas consisting of four or six bright spots which we call “four-pack” (red arrow) and “six-pack” (dark blue arrow) can be found on $\text{Sr}_3\text{Ru}_2\text{O}_7$. On Sr_2RuO_4 the number of these ordered structures is significantly higher and even “two-packs” (light blue arrow) and “single-packs” (yellow arrow) were found. Assuming that the bright lines are caused by dissociated water molecules, as in the low-coverage case, and that the OH groups are located on the same Sr-Sr bridge site, the bright spots of the single-, two-, four- and six-packs must be located on top of Sr atoms [see Fig. 5.5(c)]. Thus, at higher

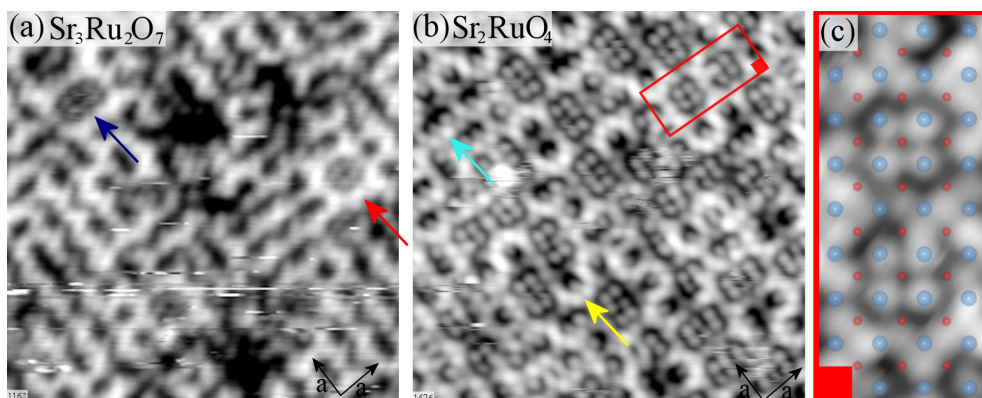


Figure 5.5: Saturation layer of water on $Sr_3Ru_2O_7$ and Sr_2RuO_4 . After exposing $Sr_3Ru_2O_7$ and Sr_2RuO_4 to 1 L H_2O at 150 K, regular structures formed. (a) On $Sr_3Ru_2O_7$ the surface consist of bright wiggly lines and patches of four dots (red arrow, “four-packs”) and six dots (dark blue arrow, “six-packs”). (b) On Sr_2RuO_4 the saturation layer consists of similar structures as on $Sr_3Ru_2O_7$. However, significantly more six-packs, four-packs and even some two-packs (light blue arrow) and single-packs (yellow arrow) are found. (c) Digitally zoomed-in image of the area marked in Fig. (b). The blue spots mark the Sr atoms and the red spots mark the oxygen atoms. The bright spots of the four pack are not located on a Sr-Sr bridge, but on a Sr atoms. Scanning conditions: (a,b) $10 \times 10 \text{ nm}^2$, $I_t = 0.15 \text{ nA}$, $T = 78 \text{ K}$, (a) $U_s = +0.5 \text{ V}$, (b) $U_s = +0.4 \text{ V}$.

coverages, there have to be two different adsorption configurations for water [see Fig. 5.5(c)]. According to Ref. [81] this is consistent with a molecular adsorption on top of the earth alkali atom [see Fig. 5.1(a), Type I].

5.6 Desorption

5.6.1 Annealing

Annealing to room temperature is sufficient to remove most of the adsorbed water from $Sr_3Ru_2O_7$ and Sr_2RuO_4 . After dosing 1 L of H_2O at 105 K the Sr_2RuO_4 crystal was annealed to room temperature for 35 h hours [see Fig. 5.6(a)]. Almost the entire water layer desorbed, however, a few 2D chains remained on the surface. In the case of $Sr_3Ru_2O_7$ after annealing to room temperature few chains remained on the surface (not shown). After further annealing for one night (~ 12 hours) more water desorbed, and after annealing for one weekend (~ 60 hours) almost all the water was gone.

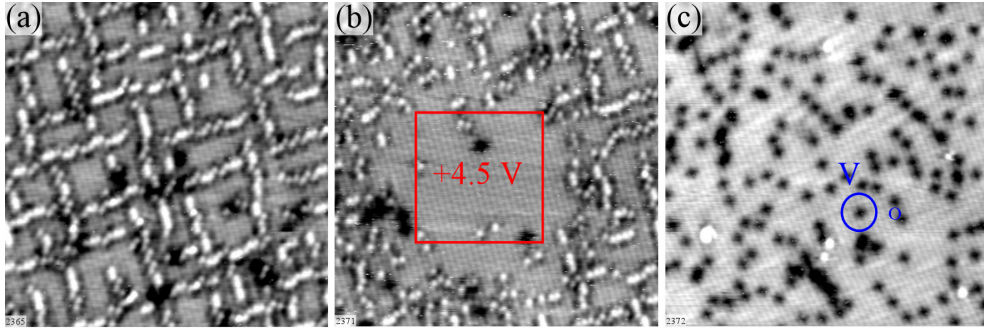


Figure 5.6: Three ways to desorb water from $\text{Sr}_3\text{Ru}_2\text{O}_7$ and Sr_2RuO_4 . All STM images show the SrO surface layer of Sr_2RuO_4 . (a) After dosing 1 L H_2O at 105 K most of the surface is covered with water [see previous section, Fig. 5.5(b)]. Annealing to room temperature (for 35 h) desorbs most of the water and only a few water chains remain on the surface. (b) An area (red square) on the water-covered surface shown in (a) was scanned with $U_s = +4.5$ V, $I_t = 0.1$ nA. Water desorbs from this area. (c) Electron bombardment of the surface shown in (a) leads to desorption of the water molecules. In addition, oxygen vacancies are formed on the cleaned surface. Scanning conditions: (a–c) 20×20 nm², $I_t = 0.1$ nA, $T = 78$ K, (a) $U_s = +0.5$ V, (b) $U_s = +0.3$ V, (c) $U_s = +0.8$ V.

5.6.2 Tip Manipulation

At certain tunneling conditions water gets also removed from the surface by some tip-sample interactions. Increasing the bias voltage to $U_s = +4.5$ V desorbs all water molecules from the scanned area [see Fig. 5.6(b)]. So far, no studies have been performed to figure out whether this process is electron-induced or field-induced. In addition, it was found that scanning at certain bias voltages ($U_s = -2$ V, -1.5 V, $+2.7$ V, $+3.0$ V) enables the diffusion of the water molecules. The finding that water can be moved at these bias voltage could be useful for further experiments where the interaction of H_2O with oxygen vacancies and CO will be investigated.

5.6.3 Electron Bombardment

A third way to desorb water is by electron bombardment. Bombarding the water covered surface [Fig. 5.6(a)] for 45 minutes with 1000 eV electrons leads to a desorption of the water molecules. It is plausible that secondary electrons created by the primary high energy electrons cause the desorption. This desorption mechanism might be similar to the desorption process via tip

manipulation, if it is electron and not field induced.

5.7 Water Dissociation at V_{OS}

In Section 3.5 we have described how to create oxygen vacancies in the SrO layer of $Sr_3Ru_2O_7$. After bombarding the clean surface for 45 minutes with 1000 eV electrons at 105 K approximately 4.2 % ML oxygen vacancies were created [see Fig. 5.7(a)]. To investigate the interaction of V_{OS} with H_2O , we dosed 0.023 L H_2O right onto this surface at 105 K. Fig. 5.7(b) reveals that the water did not interact with the oxygen vacancies, as both features are still visible individually. Whether it is an activation barrier, or the limited diffusion of the water molecules, that hinders this reaction is not known. However, after annealing to 200 K fewer V_{OS} are present and H_2O is no longer found on the surface [see Fig. 5.7(c)]. Instead a new feature appears, which is centered at the Sr-Sr bridge site. Dosing additional 0.023 L H_2O onto the surface shown in Fig. 5.7(d) reveals the difference between water molecules and the new feature [see inset Fig. 5.7(c)]. It can be expected that one H_2O molecule reacted with one V_O to form two surface hydroxyls (O_sH_{ads}). Unfortunately, due to poor statistics it cannot be confirmed whether the number these new features is twice the number of oxygen vacancies in the beginning, as would be expected. As the O_sH_{ads} appears on a Sr-Sr bridge site in STM instead of a 4-fold site on top of the O_s , these hydroxyl groups are most likely not upright but tilted. However, up to now, no calculations were performed, which describe the exact adsorption behavior of one hydrogen on top of a surface oxygen atom O_s . It seems that two hydroxyls do not want to get too close to each other, and one Sr-Sr bridge site is always empty between two hydroxyls. Thus two hydrogen atoms sitting on two neighboring O_s atoms could repel each other due to their negative charge [89].

5.8 Conclusion

Our results clearly show that single water molecules dissociate on the SrO surface layer of Sr_2RuO_4 and $Sr_3Ru_2O_7$, and that the two hydroxyls, $(OH)_{ads}$ and O_sH_{ads} , are still able interact via a hydrogen bond. Due to this interaction

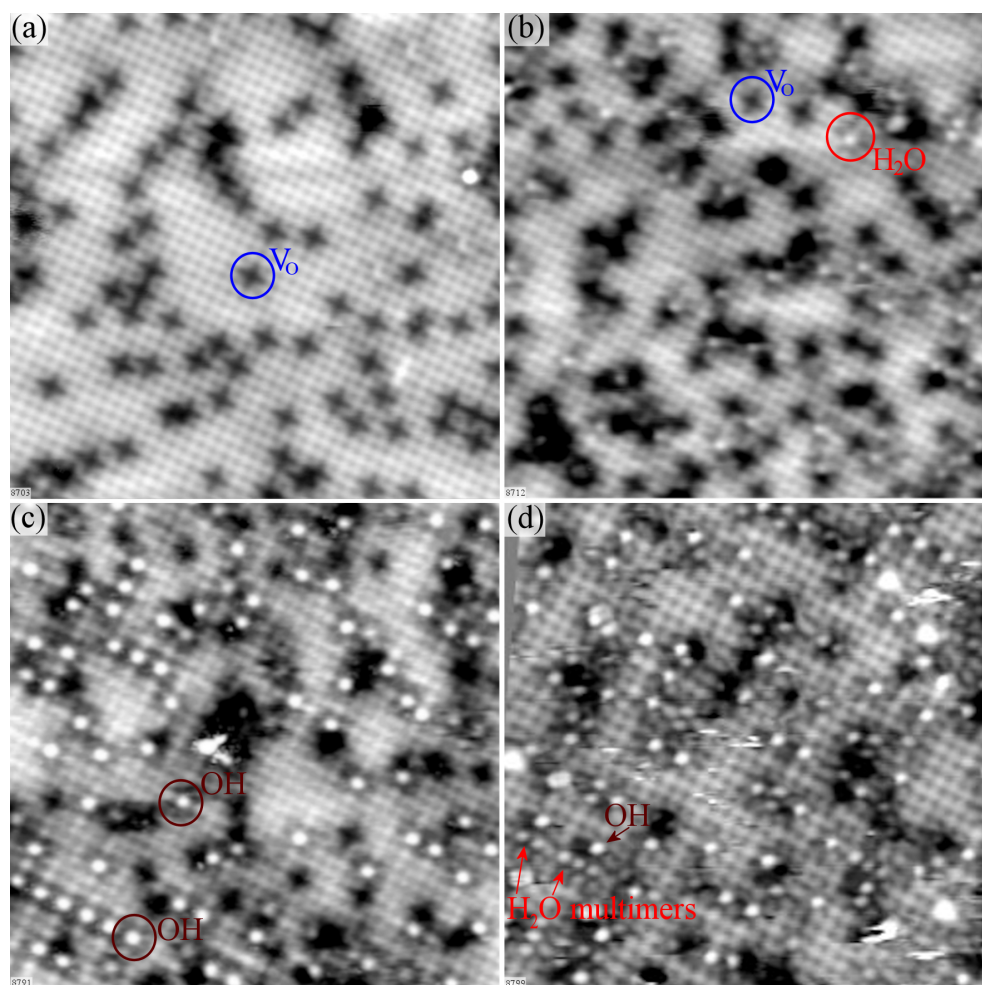


Figure 5.7: Interaction of H₂O with oxygen vacancies. (a) After bombarding the SrO surface of Sr₃Ru₂O₇ with electrons, oxygen vacancies are formed. The V_Os appear as dark crosses centered at the position of the apical oxygen atom (blue circle). (b) After dosing 0.023 L H₂O at 105 K water molecules (red circle) and oxygen vacancies are found on the surface. No reaction took place. (c) Additional annealing to 200 K leads to new features (OH) positioned at Sr-Sr bridge sites (brown circle). (d) After dosing additional 0.023 L H₂O some water chains form (red arrows), which look different from hydroxyls (brown arrows). Scanning conditions: (a–d) 15×15 nm², $I_t = 0.15$ nA, $T = 78$ K, (a) $U_s = +0.1$ V, (b) $U_s = +0.2$ V, (c) $U_s = +0.8$ V, (d) $U_s = +0.4$ V.

the adsorbed hydroxyls cannot move freely on the surface but are trapped by the O_sH_{ads} , which allows the $(OH)_{ads}$ just to jump from one Sr-Sr bridge around the H_{ads} to another Sr-Sr bridge. According to DFT, the activation energy for this process is relatively small ($E_{act} = 0.18$ eV).

The dissociated water adsorption and the jumping of the $(OH)_{ads}$ is also in good agreement with the predicted water adsorption on CaO, SrO and BaO [81, 82, 88, 89]. Grönbeck *et al.* [89] pointed out that the two dissociated hydroxyls, $(OH)_{ads}$ and O_sH_{ads} are both negatively charged and repel each other. However due to the interaction with the Ba ions this repulsion is screened and the two dissociated hydroxyls can still interact via a hydrogen bond. As described by Hu *et al.* [81] the dissociative adsorption becomes more favorable with increasing lattice constant. This result is also in good agreement with the observed dissociative water adsorption on the SrO surface layer of $Sr_3Ru_2O_7$, as the Sr-Sr distance in the SrO layer of perovskite oxides (SrTiO₃: 3.90 Å, $Sr_3Ru_2O_7$: 3.87 Å) is even bigger than the Sr-Sr distance of their binary earth alkali counterpart (SrO: $a_0/\sqrt{2}=5.16$ Å/ $\sqrt{2}=3.54$ Å).

On oxygen-covered Ru(0001) the formation of water chains was observed just below the desorption temperature of water. This formation was explained by the dipole-dipole interaction between two neighboring water molecules [90]. On TiO₂(110) hydrogen bonds are formed between intact water molecules sitting on two neighboring fivefold-coordinated Ti atoms of the Ti rows forming 1D chains [91]. On ZnO hydrogen bonding between dissociated and non dissociated water molecules lead to a regular water structure [92]. The general rule for forming regular water structures is that the O-O distance should not be too different from bulk ice. However, the regular structures on TiO₂ and ZnO have O-O distances of about 3 and 3.3 Å which is significantly larger than the O-O distance of ice (2.61 Å).

On $Sr_3Ru_2O_7$ the distance between two O atoms of two $(OH)_{ads}$ is about 4 Å and significantly larger than for TiO₂ and ZnO. It is quite unlikely that a hydrogen bond of more than 4 Å stabilizes the dimer and longer multimers. In the case of the stable dimer, the interaction between the adsorbed water molecules and the $c(2 \times 2)$ structure and therefore the RuO₆ rotation is important. In the case of dimers on the “narrow” site the Sr atom between two $(OH)_{ads}$ is moved **with** the RuO₆ octahedra rotation direction and in the

case of dimers on the “wide” site the RuO_6 octahedra are moved **against** the rotation direction. This way, the Sr atom between two $(\text{OH})_{\text{ads}}$ has more space to move from its initial position, which might explain the energy difference of $\Delta E = 80$ meV between these two configurations.

Longer chains are most likely also explained by local lattice distortions induced by adsorbed water. If the lattice is already slightly distorted due to the dimer formation, the next Sr-atom between two $(\text{OH})_{\text{ads}}$ might get pushed away more easily.

The full monolayer adsorption suggests that water can adsorb at two different sites, and that, at higher coverages, water is not only able to adsorb dissociatively but also molecularly. It is interesting that this is exactly opposite to MgO, where single water molecules adsorb molecularly and at higher coverages water molecules partially dissociate [93]. However, to better understand the adsorption of a full monolayer, further calculations are needed.

Chapter 6

FT-STs measurements on Sr_2RuO_4

In Section 2.4.3 we introduced the possibility to probe the band structure by the use of the FT-STs technique. Electrons scattered at point defects interfere with themselves and form standing waves in the LDOS with a wavevector $q = 2k_E$. These scattering vectors join two points on curves of constant electron energy (CCE) in k-space and are identified in the FFT of dI/dV maps. In the case of simple, free-electron like systems, the band dispersion is parabolic, and the CCE are circles in k-space and appear as circles in the FT-STs. In the case of more complex band structures, the interpretation of the scattering vectors in FFT is not trivial, as shown for some high-temperature superconductors [94, 95] and $\text{Sr}_3\text{Ru}_2\text{O}_7$ [57].

To investigate the band structure of Sr_2RuO_4 with FT-STs we studied slightly Mn-doped samples, which were already discussed in Section 3.4.2. Quasiparticles scattered at the Mn dopants interfere with themselves and form standing waves in the LDOS [see Fig. 6.1 (a)]. To investigate the modulation in the LDOS a dI/dV map at $U_s = +10$ mV was recorded. The dI/dV map was created using a lock-in amplifier which superimposed an AC voltage on the DC tunneling bias voltage and recorded the AC component of the tunneling current. The dI/dV map was recorded in a “quasi-constant-height” measuring mode, by lowering the loop gain to a very low value (1%). While it is difficult to characterize the involved wave vectors in the dI/dV map, the FFT of the dI/dV map gives clear information about the involved scattering

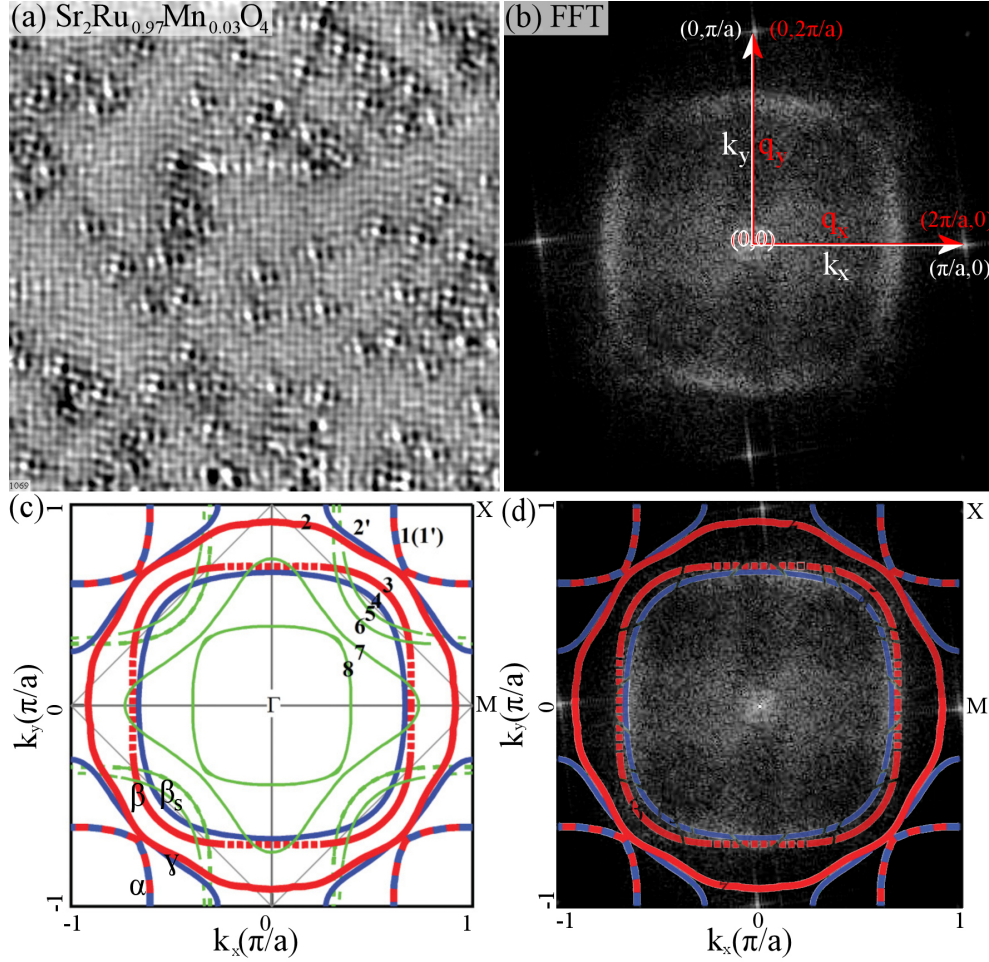


Figure 6.1: Characterization of standing waves on $\text{Sr}_2\text{Ru}_{0.97}\text{Mn}_{0.03}\text{O}_4$. (a) dI/dV map taken at $U_s = +10$ mV, $T = 6$ K. In addition to the atomic structure of the SrO layer, standing waves are seen. (b) The FFT of the dI/dV map reveals four bright spots that correspond to the lattice points in q -space, which allow the calibration of the q_x and q_y axes. Due to the doubling of the wavevector q , the lattice points correspond to $(\pi, 0)$ and $(0, \pi)$ spots in k -space. In addition, a rounded square-like interference pattern is visible. (c) Fermi Surface obtained from ARPES measurements (reprinted from [24]). See section 1.2.1 for a detailed explanation. (d) A superposition of (b) and (c) illustrates that the FT-STs results show the the β_s band. Scanning conditions: (a) 24×24 nm², $U_s = +10$ mV, $I_t = 0.25$ nA, $T = 6$ K, loop gain: 1 % scanning speed: 10 nm/s.

vectors. In the FFT image four bright spots mark the reciprocal lattice points and determine the direction of the reciprocal lattice vectors q_x and q_y . The spots correspond to a q_x vector of $(2\pi, 0)$ and a q_y vector of $(0, 2\pi)$. Due to the doubling of the wave vector q ($q = 2k$), these spots correspond to a k_x and k_y vector of $(\pi, 0)$ and $(0, \pi)$, respectively. A re-normalization of the reciprocal space vectors from $q \rightarrow k$ is necessary to compare FT-STs results with ARPES measurements.

The ARPES measurements performed by Liu *et al.* [24] beautifully illustrate the bulk α , β and γ bands [see Fig. 6.1(c)]. In addition, surface bands, caused by the $c(2 \times 2)$ reconstruction of the surface layer are visible [see Fig. 6.1(c), blue lines]. In our FT-STs image the scattering vectors form a rounded square structure, which is in good agreement with the surface β_s band observed in ARPES [see Fig. 6.1(d)]. In addition to the rounded square-like structure, the FFT reveals more features, which cannot easily be characterized, due to the complex band structure of Sr_2RuO_4 . More experimental data and theoretical help will be necessary to fully understand the scattering pattern observed in Fig. 6.1(b).

To gain more information about the occupied states, which are also probed in ARPES, we performed measurements at various negative sample bias voltages. Information about the unoccupied states, which cannot be probed in ARPES were found, by taking dI/dV maps at positive sample bias voltages [see Fig 6.2]. Along the series from $U_s = -50$ mV to $U_s = -10$ mV the k_x vector of the the surface β_s band remains about $0.62 \pi/a$ [see Fig. 6.2, red rounded square, Fig. 6.3]. However, above -10 mV the scattering vector k_x increases to $0.67 \pi/a$. In addition, a second structure is observed at $U_s = 25$ mV and $U_s = 40$ mV with a k_x vector of $0.73\pi/a$ and $0.78\pi/a$, respectively [see Fig. 6.2 (blue circle)]. This second band might be explained by contributions from a second surface state, however, further theoretical support will be necessary to understand these features. The complex inner structure at $U_s = +15$ mV cannot be explained at this point. It is planned to continue these experiments in a collaboration with a theoretical group.

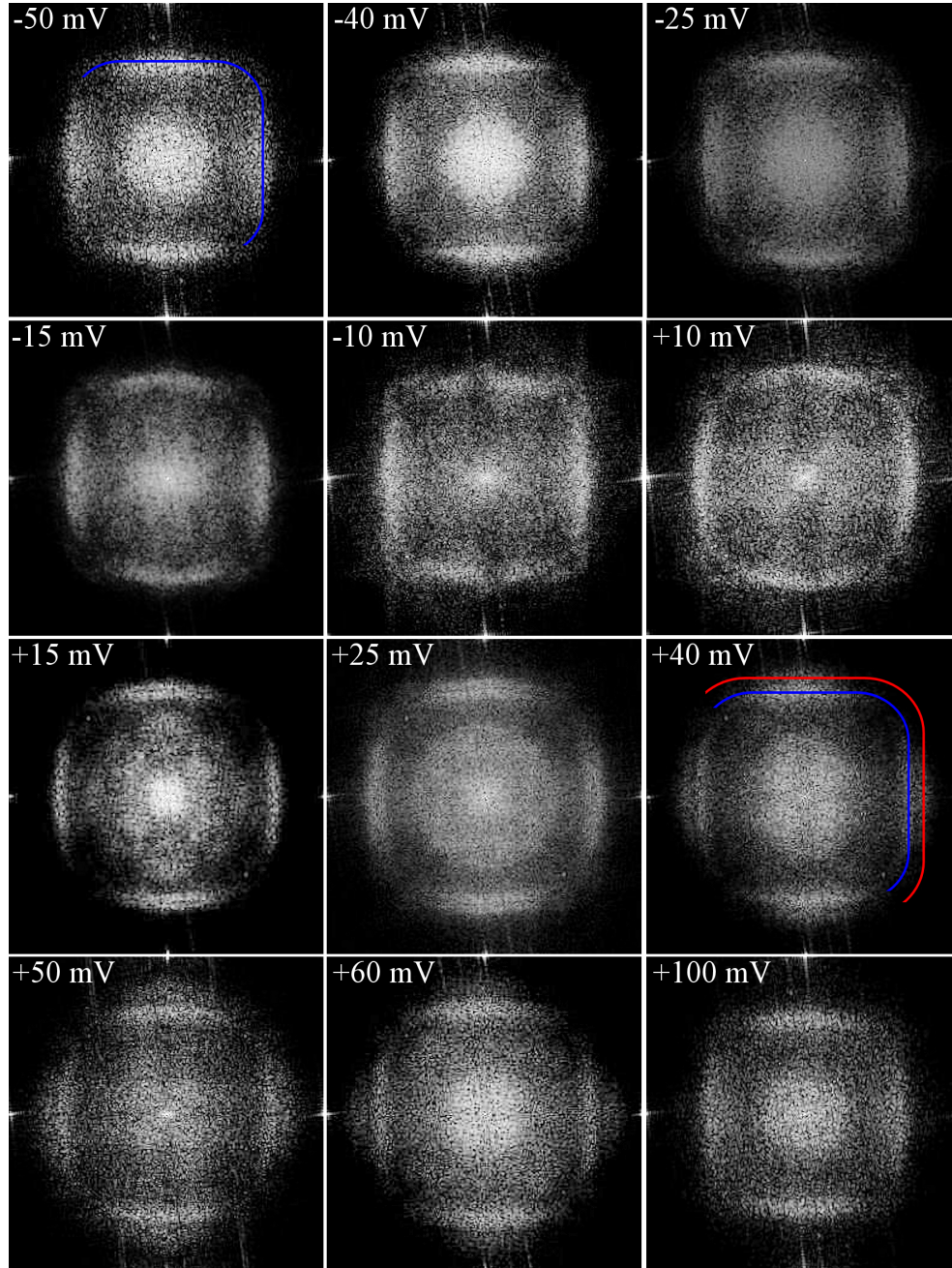


Figure 6.2: 12 cuts through the band structure of Sr_2RuO_4 . By recording twelve dI/dV maps at different sample voltages, and conducting a Fourier transformation, one can see how the scattering vectors change. The blue rounded square mark the β_s band. The band marked by a red square is yet not understood.

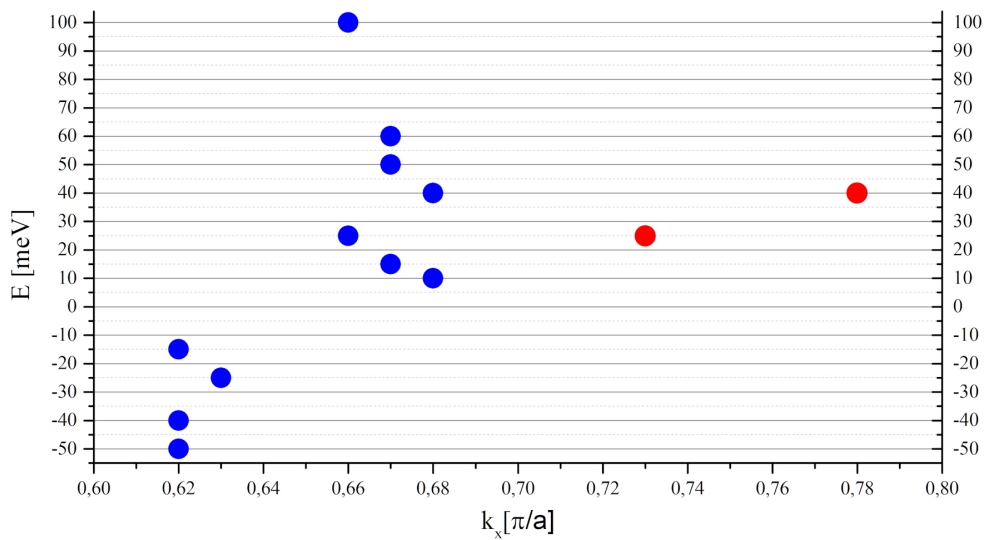


Figure 6.3: Analysis of the scattering vectors. The k_x vector of the 12 CCE cuts shown in Fig. 6.2 that correspond to the surface β_s band. From $U_s = -50$ mV to $U_s = -10$ mV the surface β_s band does not change significantly and the k_x vector remains about $0.62 \pi/a$. Above -10 mV the scattering vector k_x increases to $0.67 \pi/a$. The red dots mark the appearance of second, larger scattering vector observed at $U_s = +25$ mV and $U_s = +40$ mV.

Chapter 7

Preliminary Results

I have spent most of my time in the lab investigating the properties of the clean surface, defects and the adsorption behavior of CO and H₂O. However, I have also collected some preliminary results, dealing with the adsorption of O₂ and CO₂ on Sr₃Ru₂O₇. I hope that these results will serve as a good starting point for further experiments.

7.1 Adsorption of O₂

We used the directional doser for dosing O₂ on Sr₃Ru₂O₇. Thus no exact doses can be given. After dosing ~ 0.2 L O₂¹ at 105 K, no sign of adsorbed molecules can be found on the surface. After dosing ~ 2 L O₂ a new (1×1) structure is visible in STM. This (1×1) structure is not perfect, but a few “flower-like” defects are present, where four or six spots of the (1×1) structure are missing [see Fig. 7.1(a), red arrow]. Repeated scanning reveals that with every scan more spots of the (1×1) structure are removed. This finding suggests that the O₂ molecules move under the tip at low coverages and are invisible to STM. At a monolayer coverage the oxygen molecules cannot move under the tip and a new 1×1 structure with flower-like defects is visible. So far it is unknown how single O₂ molecules are removed by the tip. A similar behavior was also reported on La_{5/8}Ca_{3/8}MnO₃, where parts

¹Dose according to ion gauge: 0.02 L. This value was multiplied by 10, due to the use of the directional doser.

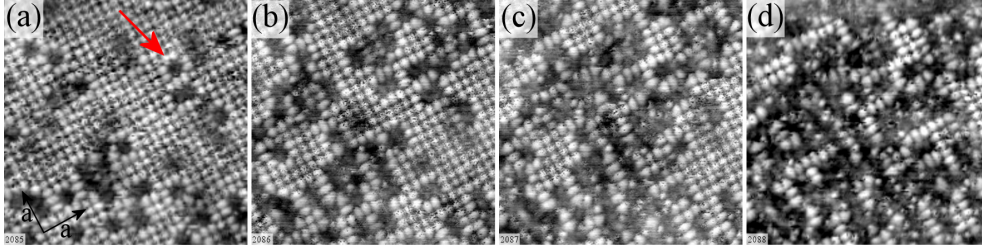


Figure 7.1: Adsorption of O_2 on $\text{Sr}_3\text{Ru}_2\text{O}_7$. (a–d) Four STM images of the same area. (a) ~ 2 L O_2 dosed at 105 K. A (1×1) structure is visible. “Flower-like” defects are visible as well (red arrow). In the center of these defects, four white spots of the 1×1 structure are missing. A few larger defects, where six spots are missing, are found as well. (b, c, d) After scanning across the same area several times, more spots are removed. (a–d) 15×15 nm², $U_s = -0.55$ V, $I_t = 0.155$ nA, $T = 78$ K.

of an oxygen monolayer was scraped off by the STM tip [96].

7.2 Adsorption of CO_2

To investigate the interaction between CO_2 and the SrO surface layer of $\text{Sr}_3\text{Ru}_2\text{O}_7$ we dosed 0.002 L CO_2 onto the sample [see Fig. 7.2(a,b)]. New features appear in STM that are more or less centered at the oxygen lattice site (red arrows). These features are always dark and fuzzy. The exact adsorption configuration and the desorption temperature are unknown at this point. After annealing to room temperature, the CO_2 molecules or CO_2 -induced entities are still on the surface, indicating an adsorption energy of at least ~ 1 eV.

After exposing the surface to ~ 50 L CO_2 at room temperature most likely the entire surface was covered with CO_2 [see Fig. 7.2(c)]. In FFT neither any signs of the substrate spots, nor any other long-range ordered structures are visible. However, STM reveals small patches with ordered structures. Scanning across the surface with an unusually high bias voltage ($U_s = +10$ V) desorbs CO_2 from the scanned and the surrounding area [see Fig. 7.2(d), red square]. In the scanned area and the area close to the scanned area oxygen vacancies were created. Previously, high-bias voltage scans on the clean $\text{Sr}_3\text{Ru}_2\text{O}_7$ surface were only performed up to $U_s = +7$ V, showing that no oxygen vacancies are formed at these scanning conditions. Thus, it is

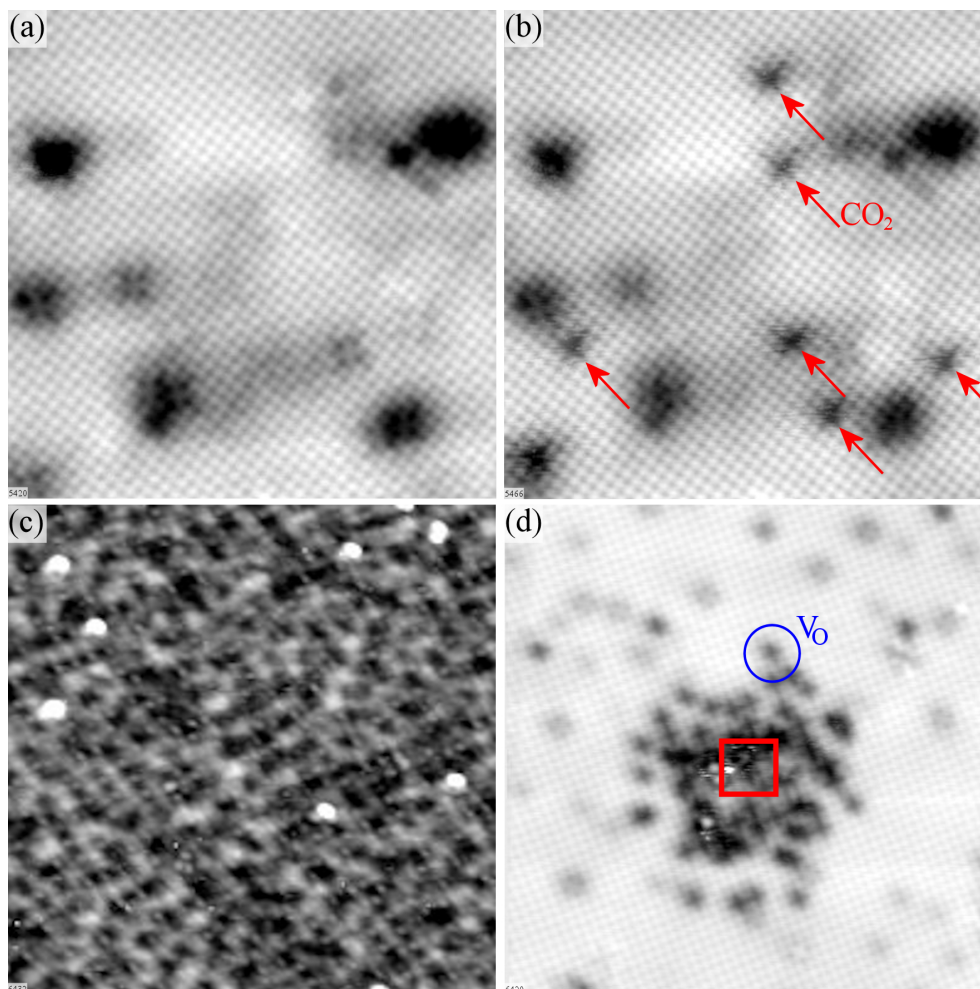


Figure 7.2: Adsorption of CO_2 on $\text{Sr}_3\text{Ru}_2\text{O}_7$. (a) The as-cleaved surface. (b) After dosing 0.002 L CO_2 new features appear. CO_2 is imaged as a dark, fuzzy feature, centered more or less on an apical oxygen lattice site (red arrows). (c) After dosing ~ 50 L CO_2 at room temperature the lattice structure is no longer apparent. New short range ordered structures appear. (d) Scanning at $U_s = +10$ V removed CO_2 from the scanned area (red square) and neighboring areas. Oxygen vacancies were created as well (marked with a blue circle). Scanning conditions: (a) $15 \times 15 \text{ nm}^2$, $U_s = +0.05$ V, $I_t = 0.15$ nA, $T = 78$ K, (b) $15 \times 15 \text{ nm}^2$, $U_s = +0.005$ V, $I_t = 0.15$ nA, $T = 78$ K, (c) $20 \times 20 \text{ nm}^2$, $U_s = +1.0$ V, $I_t = 0.155$ nA, (d) $20 \times 20 \text{ nm}^2$, $U_s = +1.0$ V, $I_t = 0.15$ nA.

not possible to decide whether adsorbed CO_2 molecules play a role in the formation of oxygen vacancies at $U_s = +10$ V.

Chapter 8

Summary and Outlook

When I started my Ph.D thesis, very little about defects and nothing about the adsorption behavior of molecules on strontium ruthenates was known. Therefore, I spent most of my time as Ph.D student to characterize defects and the adsorption behavior of common molecules present in the residual gas.

Our first important finding was that no surface defects are created if the samples are cleaved at low temperature or at room temperature. This result stands in contrast to a study by Penneec *et al.* [53], suggesting that defects are formed during cleaving and that this process is temperature driven. If defects are present at the as-cleaved surface, they are either bulk impurities or by adsorbates from the residual gas.

The SrO surface is highly reactive. Molecules such as CO, H₂O and CO₂, which are common members of the residual gas, adsorb easily and are stable up to room temperature. CO adsorbs in two different configurations on Sr₃Ru₂O₇, namely a precursor (physisorbed) and as a carboxylate (chemisorbed), both adsorbed at the position of the apical oxygen atoms. The precursor is only observed if CO is dosed below 78 K on Sr₃Ru₂O₇. If CO is dosed above 100 K only the carboxylate can be found on the surface. By annealing the precursor to 100 K or by manipulating the precursor with the STM tip, it can be transformed into the more stable carboxylate. The carboxylate has a very characteristic appearance in STM, as it is imaged as a large dark cross centered at the position of the apical oxygen atom. This configuration results from a reaction of the CO with the surface atoms, and is a structure similar to a bent CO molecule in an oxygen vacancy.

The interaction of water with the SrO surface is not as strong as the one between CO and $\text{Sr}_3\text{Ru}_2\text{O}_7$. At 78 K water dissociates on the clean surface, forming two hydroxyls $(\text{OH})_{\text{ads}}$ and $\text{O}_s\text{H}_{\text{ads}}$. These two hydroxyls still interact with each other and form “dynamic ion pairs”, which were already predicted for water on CaO, BaO and SrTiO_3 . Due to the interaction between $(\text{OH})_{\text{ads}}$ and $\text{O}_s\text{H}_{\text{ads}}$, the $(\text{OH})_{\text{ads}}$ sitting on a Sr-Sr bridge can just jump around the $\text{O}_s\text{H}_{\text{ads}}$ to one of the other three Sr-Sr bridge sites. By exposing the surface to more water, dimers and long water chains form, which are stable up to room temperature. At high coverages, a second adsorption configuration is observed, where the water most likely adsorbs molecularly on a Sr atom.

Whereas these first studies focused on exploring the chemical properties of Sr_2RuO_4 , $\text{Sr}_3\text{Ru}_2\text{O}_7$, at the end of my Ph.D time I started to investigate physical properties of perovskites as well. Quasiparticles scattered at impurities (dopants) interfere with themselves and form standing waves, which can be observed in STM. Fourier transformation of the STM images reveals information about the involved scattering vectors and about the electronic band structure. First results already show that the surface β band formed by the Ru 4 d_{xy} orbital can be imaged in FT-STs. However, to better understand the data further collaborations with a theory group will be necessary.

My successor Daniel Halwidl will investigate how oxygen vacancies influence the adsorption behavior of different molecules such as CO, CO_2 and H_2O on strontium ruthenates. In addition, the interaction between different molecules will be investigated. One main part of his project will also be to compare the adsorption behavior of CO, CO_2 and H_2O on $\text{Sr}_3\text{Ru}_2\text{O}_7$ and $\text{Ca}_3\text{Ru}_2\text{O}_7$, where the octahedra are tilted and rotated.

A short summary of the most important results follows:

8.1 Sample Preparation

1. Only very small amounts of glue should be used for gluing the single crystals on the sample plate. Otherwise the sample plate and the cleaving stub are glued together, and the glue has to be cleaved as well.
2. Excess glue might cause uncontrollable movements of the wobble stick

or broken “glue dust” may contaminate the as-cleaved surface.

8.2 As-cleaved surfaces

1. Sr_2RuO_4 and $\text{Sr}_3\text{Ru}_2\text{O}_7$ single crystals cleave between two SrO layers.
2. No defects such as Sr or O vacancies are formed during cleaving.
3. In STM, Sr atoms are imaged as bright protrusions and oxygen atoms are imaged as dark depressions.
4. Point defects observed on the as-cleaved surface result from bulk impurities or adsorbates from the residual gas.
5. Oxygen vacancies can be created by bombarding the SrO surface with high energy electrons (500 eV).

8.3 Adsorption of CO

1. **Adsorption on $\text{Sr}_3\text{Ru}_2\text{O}_7$**
 - (a) At 78 K, CO molecules adsorb first at Ca dopants and some other unknown defects before adsorbing on the clean surface.
 - (b) CO adsorbs first above the apical surface O atom with a DFT-derived binding energy $E_{\text{ads}} = -0.7$ eV (precursor).
 - (c) Above 100 K, the CO replaces the surface O and forms a Ru-COO carboxylate with a binding energy $E_{\text{ads}} = -2.2$ eV. The carboxylate appears in STM as a dark cross centered on an apical oxygen atom.
 - (d) The activation barrier from the physisorbed precursor to the chemisorbed carboxylate is small ($E_{\text{act}} = 0.17$ eV).
 - (e) The precursor as well as the carboxylate can be removed by tip-sample interactions.
 - (f) CO_2 reacts with a V_{O} to a V_{O}/CO_2 complex.
2. **Adsorption on Sr_2RuO_4**

- (a) No precursor can be found.
- (b) The carboxylate is formed at any temperature.
- (c) Higher sticking probability than on $\text{Sr}_3\text{Ru}_2\text{O}_7$.
- (d) The carboxylate can be removed by tip-sample interactions.

8.4 Adsorption of H_2O

1. Water dissociates on the clean surface, forming two hydroxyls: $(\text{OH})_{\text{ads}}$ and $\text{O}_s\text{H}_{\text{ads}}$.
2. The two hydroxyls still interact: $(\text{OH})_{\text{ads}}$ moves around the $\text{O}_s\text{H}_{\text{ads}}$ from one Sr-Sr bridge to the next.
3. Two water molecules form stable water dimers. Their position depends on the $c(2\times 2)$ reconstruction, although this reconstruction affects only the geometry of the subsurface layer.
4. If the sample is annealed to room temperature, water molecules start to diffuse, interact with each other, and form long 1D chains.
5. At high water coverages water also adsorbs in a second adsorption configuration. (Most likely molecular adsorption on top of a Sr atom)
6. Water can be removed by sample-tip interaction or electron bombardment.
7. Water molecules interact with oxygen vacancies forming two surface hydroxyls $\text{O}_s\text{H}_{\text{ads}}$

8.5 FT-STs measurements on Sr_2RuO_4

1. Mn dopants serve as quasiparticle scattering centers and standing waves can be observed in STM.
2. Fourier transformations of dI/dV maps reveal information about the scattering vectors at a certain voltage U_s .

3. In FT-STIS images the β_s surface band is visible near E_F . The results are in good agreement with ARPES measurements.

Appendix A

List of all STM images

Table A.1: List of all STM images

<i>Figure numbers</i>	<i>Image numbers</i>	<i>File path</i>	
Fig. 3.4	(a)	2419	..\Sr3Ru2O7
	(b)	5204	..\Sr3Ru2O7
	(c)	5701	..\Sr3Ru2O7
	(d)	7501	..\Sr3Ru2O7
Fig. 3.5		1905	..\Sr2Ru1O4
Fig. 3.6	(a)	2419	..\(Sr0.95Ca0.05)3Ru2O7
Fig. 3.7	(a)	1012	..\Sr2Ru0.97Co0.03O4
	(b)	1067	..\Sr2Ru0.97Mn0.03O4
Fig. 3.8	(a)	8703	..\Sr3Ru2O7
	(b)	8704	..\Sr3Ru2O7
Fig. 3.9		8326	..\Sr3Ru2O7
Fig. 3.10		6634	..\Sr3Ru2O7
Fig. 3.11	(a)	3209	..\Sr3Ru2O7
	(b)	3210	..\Sr3Ru2O7
	(c)	3210	..\Sr3Ru2O7
	(d)	7906	..\Sr3Ru2O7
Fig. 4.1	(a)	5204	..\Sr3Ru2O7
	(b)	5211	..\Sr3Ru2O7
	(c)	5226	..\Sr3Ru2O7

Continued on next page

Table A.1 – Continued from previous page

Fig. 4.2	(a)	5281	..\Sr3Ru2O7
Fig. 4.3	(a)	5290	..\Sr3Ru2O7
	(d)	1137	..\Sr2Ru0.97Mn0.03O4
Fig. 4.4	(a)	5288	..\Sr3Ru2O7
	(b)	5290	..\Sr3Ru2O7
Fig. 4.5	(a)	8016	..\Sr3Ru2O7
	(b)	8032	..\Sr3Ru2O7
	(c)	8067	..\Sr3Ru2O7
Fig 4.6	(a)	1315	..\Sr2Ru1O4
	(b)	1320	..\Sr2Ru1O4
	(c)	1337	..\Sr2Ru1O4
	(d)	1013	..\2014_Sr3Ru2O7
	(e)	1016	..\2014_Sr3Ru2O7
	(f)	1021	..\2014_Sr3Ru2O7
	(g)	4753	..\Sr3Ru2O7
	(h)	1038	..\2014_Sr3Ru2O7
Fig. 4.7	(a)	6549	..\Sr3Ru2O7
Fig. 4.8	(a)	5204	..\Sr3Ru2O7
	(b)	5211	..\Sr3Ru2O7
	(c)	4436	..\Sr3Ru2O7
Fig. 4.9	(a)	1300	..\Sr2Ru1O4
	(b)	1315	..\Sr2Ru1O4
Fig. 4.10	(a)	5283	..\Sr3Ru2O7
	(b)	5285	..\Sr3Ru2O7
	(c)	5286	..\Sr3Ru2O7
	(d)	5287	..\Sr3Ru2O7
Fig. 4.11	(a)	1346	..\Sr2Ru1O4
	(b)	1351	..\Sr2Ru1O4
	(c)	1353	..\Sr2Ru1O4
	(d)	1351	..\Sr2Ru1O4
	(e)	1352	..\Sr2Ru1O4
	(f)	4110	..\Sr3Ru2O7

Continued on next page

Table A.1 – *Continued from previous page*

Fig. 4.12	(a)	6547	..\Sr3Ru2O7
	(b)	6520	..\Sr3Ru2O7
Fig. 5.2	(a)	8647-69	..\Sr3Ru2O7
Fig. 5.3	(a)	8661	..\Sr3Ru2O7
	(b)	1593	..\Sr2Ru1O4
	(e)	1593	..\Sr2Ru1O4
Fig. 5.4	(a)	7309	..\Sr3Ru2O7
	(b)	1612	..\Sr2Ru1O4
Fig. 5.5	(a)	1162	..\2014_Sr3Ru2O7
	(b)	1676	..\Sr2Ru1O4
Fig. 5.6	(a)	2365	..\Sr2Ru1O4
	(b)	2371	..\Sr2Ru1O4
	(c)	2372	..\Sr2Ru1O4
Fig. 5.7	(a)	8703	..\Sr3Ru2O7
	(b)	8712	..\Sr3Ru2O7
	(c)	8791	..\Sr3Ru2O7
	(d)	8799	..\Sr3Ru2O7
Fig. 6.1	(a)	1069	..\Sr2Ru0.97Mn0.03O4
Fig. 6.2	-50 mV	1071	..\Sr2Ru0.97Mn0.03O4
	-40 mV	1116	..\Sr2Ru0.97Mn0.03O4
	-25 mV	1117	..\Sr2Ru0.97Mn0.03O4
	-15 mV	1121	..\Sr2Ru0.97Mn0.03O4
	-10 mV	1070	..\Sr2Ru0.97Mn0.03O4
	+10 mV	1069	..\Sr2Ru0.97Mn0.03O4
	+15 mV	1120	..\Sr2Ru0.97Mn0.03O4
	+25 mV	1118	..\Sr2Ru0.97Mn0.03O4
	+40 mV	1115	..\Sr2Ru0.97Mn0.03O4
	+50 mV	1068	..\Sr2Ru0.97Mn0.03O4
	+60 mV	1119	..\Sr2Ru0.97Mn0.03O4
	+100 mV	1067	..\Sr2Ru0.97Mn0.03O4
Fig. 7.1	(a)	2085	..\Sr3Ru2O7
	(b)	2086	..\Sr3Ru2O7

Continued on next page

Table A.1 – *Continued from previous page*

	(c)	2087	..\Sr3Ru2O7
	(d)	2088	..\Sr3Ru2O7
Fig. 7.1	(a)	5420	..\Sr3Ru2O7
	(b)	5466	..\Sr3Ru2O7
	(c)	6432	..\Sr3Ru2O7
	(d)	6420	..\Sr3Ru2O7

List of Tables

3.1	Defect concentrations in mass fractions (ppm) and % ML measured by ICP-MS and ICP-OEM	30
4.1	Coverage and sticking coefficient of CO on Sr_2RuO_4 and $\text{Sr}_3\text{Ru}_2\text{O}_7$	52
A.1	List of all STM images	93

List of Figures

1.1	Different ways to distort the ideal perovskite ABO_3	2
1.2	Phase diagram of $La_{1-x}Ca_xMnO_3$ and sketch illustrating the splitting of the d orbital due to the crystal field and the Jahn-Teller effect.	4
1.3	STM images of thin $SrRuO_3$ grown $SrTiO_3(001)$	6
1.4	Ruthenate Ruddlesden-Popper series $Sr_{n+1}Ru_nO_{3n+1}$	7
1.5	Fermi surfaces of Sr_2RuO_4 and $Sr_3Ru_2O_7$	9
2.1	Gluing gadget	14
2.2	(a) Schematic drawing of a Scanning Tunneling Microscope. (b) Tip/sample geometry in the Tersoff-Hamann Model	15
3.1	Point defects on Sr_2RuO_4 and $Sr_3Ir_2O_7$	24
3.2	Crystal structure of $Sr_3Ru_2O_7$	26
3.3	Large-scale STM image of $Sr_3Ru_2O_7$	27
3.4	As-cleaved surfaces of four different $Sr_3Ru_2O_7$ single crystals .	28
3.5	As-cleaved surface of one of our Sr_2RuO_4 crystals	31
3.6	STM images of the cleaved $(Sr_{0.95}Ca_{0.05})_3Ru_2O_7(001)$ surface .	32
3.7	STM images of intentionally doped Sr_2RuO_4 single crystals . .	34
3.8	Oxygen vacancies on $Sr_3Ru_2O_7(001)$	35
3.9	Influence of the cleaving temperature	36
3.10	Domain boundary between different rotations of the RuO_6 octahedra	37
3.11	Unidentified defects	39
4.1	Initial CO adsorption on the $Sr_3Ru_2O_7(001)$ surface at 78 K. .	44
4.2	CO-precursor adsorbed on the $Sr_3Ru_2O_7(001)$ surface	45

4.3	CO-cross adsorbed on the $\text{Sr}_3\text{Ru}_2\text{O}_7$ and $\text{Sr}_2\text{RuO}_4(001)$ surface.	47
4.4	Transition from the CO-precursor to the CO-cross	49
4.5	Reaction of CO_2 molecules with oxygen vacancies (V_{Os}) . . .	49
4.6	Different CO-coverages on Sr_2RuO_4 and $\text{Sr}_3\text{Ru}_2\text{O}_7$	51
4.7	Saturation Coverage of CO	53
4.8	CO interacting with defects	54
4.9	Interaction of CO with water on Sr_2RuO_4	55
4.10	Tip-induced desorption of the CO-precursor from $\text{Sr}_3\text{Ru}_2\text{O}_7$. .	56
4.11	Tip-induced desorption of the CO-cross from Sr_2RuO_4 and $\text{Sr}_3\text{Ru}_2\text{O}_7$	57
4.12	Saturation coverage of CO – tip-induced desorption.	58
5.1	Water adsorption on earth alkali oxides.	62
5.2	Water adsorption on SrO terminated $\text{Sr}_3\text{Ru}_2\text{O}_7$	64
5.3	Dimer formation on $\text{Sr}_3\text{Ru}_2\text{O}_7$ and Sr_2RuO_4	66
5.4	Water multimer formation on $\text{Sr}_3\text{Ru}_2\text{O}_7$ and Sr_2RuO_4	68
5.5	Saturation layer of water on $\text{Sr}_3\text{Ru}_2\text{O}_7$ and Sr_2RuO_4	70
5.6	Three ways to desorb water from $\text{Sr}_3\text{Ru}_2\text{O}_7$ and Sr_2RuO_4 . . .	71
5.7	Interaction of H_2O with oxygen vacancies.	73
6.1	Characterization of standing waves on $\text{Sr}_2\text{Ru}_{0.97}\text{Mn}_{0.03}\text{O}_4$	78
6.2	12 cuts through the band structure of Sr_2RuO_4	80
6.3	Analysis of the scattering vectors.	81
7.1	Adsorption of O_2 on $\text{Sr}_3\text{Ru}_2\text{O}_7$	84
7.2	Adsorption of CO_2 on $\text{Sr}_3\text{Ru}_2\text{O}_7$	85

Bibliography

- [1] E. Dagotto, “Complexity in Strongly Correlated Electronic Systems,” *Science*, vol. 309, no. 5732, pp. 257–262, 2005.
- [2] J. B. Goodenough, “JAHN-TELLER PHENOMENA IN SOLIDS,” *Annual Review of Materials Science*, vol. 28, no. 1, pp. 1–27, 1998.
- [3] J. M. Rondinelli and N. A. Spaldin, “Structure and properties of functional oxide thin films: Insights from electronic-structure calculations,” *Advanced Materials*, vol. 23, no. 30, pp. 3363–3381, 2011.
- [4] J. He, A. Borisevich, S. V. Kalinin, S. J. Pennycook, and S. T. Pantelides, “Control of octahedral tilts and magnetic properties of perovskite oxide heterostructures by substrate symmetry,” *Phys. Rev. Lett.*, vol. 105, p. 227203, 2010.
- [5] A. M. Glazer, “The classification of tilted octahedra in perovskites,” *Acta Crystallographica Section B*, vol. 28, no. 11, pp. 3384–3392, 1972.
- [6] M. W. Lufaso and P. M. Woodward, “Jahn–Teller distortions, cation ordering and octahedral tilting in perovskites,” *Acta Crystallographica Section B*, vol. 60, no. 1, pp. 10–20, 2004.
- [7] R. Shannon, “Revised effective ionic radii and systematic studies of interatomic distances in halides and chalcogenides,” *Acta Crystallographica Section A*, vol. 32, no. 5, pp. 751–767, 1976.
- [8] Y. Takeda, F. Kanamura, M. Shimada, and M. Koizumi, “The crystal structure of BaNiO_3 ,” *Acta Crystallographica Section B*, vol. 32, no. 8, pp. 2464–2466, 1976.

- [9] M. A. Carpenter and C. J. Howard, "Symmetry rules and strain/order-parameter relationships for coupling between octahedral tilting and cooperative Jahn-Teller transitions in ABX_3 perovskites. I. Theory," *Acta Crystallographica Section B*, vol. 65, no. 2, pp. 134–146, 2009.
- [10] M. A. Carpenter and C. J. Howard, "Symmetry rules and strain/order-parameter relationships for coupling between octahedral tilting and cooperative Jahn-Teller transitions in ABX_3 perovskites. II. Application," *Acta Crystallographica Section B*, vol. 65, no. 2, pp. 147–159, 2009.
- [11] A. J. Millis, "Lattice effects in magnetoresistive manganese perovskites," *Nature*, vol. 392, no. 6672, pp. 147–150, 1998.
- [12] A. Tselev, P. Ganesh, L. Qiao, W. Siemons, Z. Gai, M. D. Biegalski, A. P. Baddorf, and S. V. Kalinin, "Oxygen Control of Atomic Structure and Physical Properties of $SrRuO_3$ Surfaces," *ACS Nano*, vol. 7, no. 5, pp. 4403–4413, 2013.
- [13] T. Vogt and D. J. Buttrey, "Low-temperature structural behavior of Sr_2RuO_4 ," *Phys. Rev. B*, vol. 52, pp. R9843–R9846, 1995.
- [14] R. Kiyonagi, K. Tsuda, N. Aso, H. Kimura, Y. Noda, Y. Yoshida, S.-I. Ikeda, and Y. Uwatoko, "Investigation of the Structure of Single Crystal $Sr_3Ru_2O_7$ by Neutron and Convergent Beam Electron Diffractions," *Journal of the Physical Society of Japan*, vol. 73, no. 3, pp. 639–642, 2004.
- [15] M. K. Crawford, R. L. Harlow, W. Marshall, Z. Li, G. Cao, R. L. Lindstrom, Q. Huang, and J. W. Lynn, "Structure and magnetism of single crystal $Sr_4Ru_3O_{10}$: A ferromagnetic triple-layer ruthenate," *Phys. Rev. B*, vol. 65, p. 214412, 2002.
- [16] J. S. Gardner, G. Balakrishnan, and D. Paul, "Neutron powder diffraction studies of Sr_2RuO_4 and $SrRuO_3$," *Physica C: Superconductivity*, vol. 252, no. 3-4, pp. 303–307, 1995.
- [17] Y. Maeno, H. Hashimoto, K. Yoshida, S. Nishizaki, T. Fujita, J. G. Bednorz, and F. Lichtenberg, "Superconductivity in a layered perovskite without copper," *Nature*, vol. 372, no. 6506, pp. 532–534, 1994.

- [18] A. P. Mackenzie and Y. Maeno, “The superconductivity of Sr_2RuO_4 and the physics of spin-triplet pairing,” *Rev. Mod. Phys.*, vol. 75, pp. 657–712, 2003.
- [19] A. Tamai, M. P. Allan, J. F. Mercure, W. Meevasana, R. Dunkel, D. H. Lu, R. S. Perry, A. P. Mackenzie, D. J. Singh, Z.-X. Shen, and F. Baumberger, “Fermi surface and van hove singularities in the itinerant metamagnet $\text{Sr}_3\text{Ru}_2\text{O}_7$,” *Phys. Rev. Lett.*, vol. 101, p. 026407, 2008.
- [20] S.-I. Ikeda, Y. Maeno, S. Nakatsuji, M. Kosaka, and Y. Uwatoko, “Ground state in $\text{Sr}_3\text{Ru}_2\text{O}_7$: Fermi liquid close to a ferromagnetic instability,” *Phys. Rev. B*, vol. 62, pp. R6089–R6092, 2000.
- [21] R. A. Borzi, S. A. Grigera, J. Farrell, R. S. Perry, S. J. S. Lister, S. L. Lee, D. A. Tennant, Y. Maeno, and A. P. Mackenzie, “Formation of a Nematic Fluid at High Fields in $\text{Sr}_3\text{Ru}_2\text{O}_7$,” *Science*, vol. 315, no. 5809, pp. 214–217, 2007.
- [22] P. B. Allen, H. Berger, O. Chauvet, L. Forro, T. Jarlborg, A. Junod, B. Revaz, and G. Santi, “Transport properties, thermodynamic properties, and electronic structure of SrRuO_3 ,” *Phys. Rev. B*, vol. 53, pp. 4393–4398, 1996.
- [23] L. Klein, J. S. Dodge, C. H. Ahn, G. J. Snyder, T. H. Geballe, M. R. Beasley, and A. Kapitulnik, “Anomalous spin scattering effects in the badly metallic itinerant ferromagnet SrRuO_3 ,” *Phys. Rev. Lett.*, vol. 77, pp. 2774–2777, 1996.
- [24] S. Liu, H. Weng, D. Mou, W. Zhang, Q. Wu, J. He, G. Liu, L. Zhao, H. Liu, X. Jia, Y. Peng, S. He, X. Dong, J. Zhang, Z. Q. Mao, C. Chen, Z. Xu, X. Dai, Z. Fang, and X. J. Zhou, “Fermi surface sheet-dependent band splitting in Sr_2RuO_4 revealed by high-resolution angle-resolved photoemission spectroscopy,” *Phys. Rev. B*, vol. 86, p. 165112, 2012.
- [25] R. Matzdorf, Ismail, T. Kimura, Y. Tokura, and E. W. Plummer, “Surface structural analysis of the layered perovskite Sr_2RuO_4 by LEED I(V),” *Phys. Rev. B*, vol. 65, p. 085404, 2002.

- [26] R. Matzdorf, Z. Fang, Ismail, J. Zhang, T. Kimura, Y. Tokura, K. Terakura, and E. W. Plummer, “Ferromagnetism stabilized by lattice distortion at the surface of the p-wave superconductor Sr_2RuO_4 ,” *Science*, vol. 289, no. 5480, pp. 746–748, 2000.
- [27] H. Müller-Buschbaum and J. Wilkens, “Ein Beitrag über Sr_2RuO_4 und $\text{Sr}_3\text{Ru}_2\text{O}_7$ Zur Oktaederstreckung von M^{4+} in K_2NiF_4^- und $\text{Sr}_3\text{Ti}_2\text{O}_7$ -Typ-Verbindungen,” *Zeitschrift für anorganische und allgemeine Chemie*, vol. 591, no. 1, pp. 161–166, 1990.
- [28] Q. Huang, J. W. Lynn, R. W. Erwin, J. Jarupatrakorn, and R. J. Cava, “Oxygen displacements and search for magnetic order in $\text{Sr}_3\text{Ru}_2\text{O}_7$,” *Phys. Rev. B*, vol. 58, pp. 8515–8521, 1998.
- [29] B. Hu, G. T. McCandless, M. Menard, V. B. Nascimento, J. Y. Chan, E. W. Plummer, and R. Jin, “Surface and bulk structural properties of single-crystalline $\text{Sr}_3\text{Ru}_2\text{O}_7$,” *Phys. Rev. B*, vol. 81, p. 184104, 2010.
- [30] R. S. Perry, K. Kitagawa, S. A. Grigera, R. A. Borzi, A. P. Mackenzie, K. Ishida, and Y. Maeno, “Multiple first-order metamagnetic transitions and quantum oscillations in ultrapure $\text{Sr}_3\text{Ru}_2\text{O}_7$,” *Phys. Rev. Lett.*, vol. 92, p. 166602, 2004.
- [31] Z. Q. Mao, Y. Maenoab, and H. Fukazawa, “Crystal growth of Sr_2RuO_4 ,” *Materials Research Bulletin*, vol. 35, no. 11, pp. 1813–1824, 2000.
- [32] S. M. Koohpayeh, D. Fort, and J. S. Abell, “The optical floating zone technique: A review of experimental procedures with special reference to oxides,” *Progress in Crystal Growth and Characterization of Materials*, vol. 54, no. 3-4, pp. 121–137, 2008.
- [33] M. Menhard, “Analysis of $\text{Ca}_3\text{Ru}_2\text{O}_7$ with scanning tunneling microscopy,” *Projektarbeit TU Wien*, 2011.
- [34] J. Tersoff and D. R. Hamann, “Theory and application for the scanning tunneling microscope,” *Phys. Rev. Lett.*, vol. 50, pp. 1998–2001, 1983.
- [35] J. Tersoff and D. R. Hamann, “Theory of the scanning tunneling microscope,” *Phys. Rev. B*, vol. 31, pp. 805–813, 1985.

-
- [36] J. Bardeen, “Tunnelling from a many-particle point of view,” *Phys. Rev. Lett.*, vol. 6, pp. 57–59, 1961.
- [37] L. Petersen, P. Hofmann, E. W. Plummer, and F. Besenbacher, “Fourier Transform-STM: determining the surface Fermi contour,” *Journal of Electron Spectroscopy and Related Phenomena*, vol. 109, no. 1-2, pp. 97–115, 2000.
- [38] L. Simon, C. Bena, F. Vonau, M. Cranney, and D. Aubel, “Fourier-transform scanning tunnelling spectroscopy: the possibility to obtain constant-energy maps and band dispersion using a local measurement,” *Journal of Physics D: Applied Physics*, vol. 44, no. 46, p. 464010, 2011.
- [39] P. Hofmann, B. G. Briner, M. Doering, H.-P. Rust, E. W. Plummer, and A. M. Bradshaw, “Anisotropic two-dimensional friedel oscillations,” *Phys. Rev. Lett.*, vol. 79, pp. 265–268, 1997.
- [40] P. T. Sprunger, L. Petersen, E. W. Plummer, E. Lægsgaard, and F. Besenbacher, “Giant Friedel Oscillations on the Beryllium(0001) Surface,” *Science*, vol. 275, no. 5307, pp. 1764–1767, 1997.
- [41] Y. Hasegawa and P. Avouris, “Direct observation of standing wave formation at surface steps using scanning tunneling spectroscopy,” *Phys. Rev. Lett.*, vol. 71, pp. 1071–1074, 1993.
- [42] G. Hörmandinger, “Comment on ”direct observation of standing wave formation at surface steps using scanning tunneling spectroscopy”,” *Phys. Rev. Lett.*, vol. 73, pp. 910–910, 1994.
- [43] D. M. Eigler and E. K. Schweizer, “Positioning single atoms with a scanning tunnelling microscope,” *Nature*, vol. 344, no. 6266, pp. 524–526, 1990.
- [44] S.-W. Hla, “Scanning tunneling microscopy single atom/molecule manipulation and its application to nanoscience and technology,” *Journal of Vacuum Science & Technology B*, vol. 23, no. 4, 2005.
- [45] K. Morgenstern, N. Lorente, and K.-H. Rieder, “Controlled manipulation of single atoms and small molecules using the scanning tunnelling

- microscope,” *physica status solidi (b)*, vol. 250, no. 9, pp. 1671–1751, 2013.
- [46] S.-W. Hla, K.-F. Braun, and K.-H. Rieder, “Single-atom manipulation mechanisms during a quantum corral construction,” *Phys. Rev. B*, vol. 67, p. 201402, 2003.
- [47] L. Bartels, G. Meyer, K.-H. Rieder, D. Velic, E. Knoesel, A. Hotzel, M. Wolf, and G. Ertl, “Dynamics of electron-induced manipulation of individual CO molecules on Cu(111),” *Phys. Rev. Lett.*, vol. 80, pp. 2004–2007, 1998.
- [48] B. Stöger, M. Hieckel, F. Mittendorfer, Z. Wang, M. Schmid, G. S. Parkinson, D. Fobes, J. Peng, J. E. Ortmann, A. Limbeck, Z. Mao, J. Redinger, and U. Diebold, “Point defects at cleaved $\text{Sr}_{n+1}\text{Ru}_n\text{O}_{3n+1}(001)$ surfaces,” *Phys. Rev. B*, vol. 90, p. 165438, 2014.
- [49] M. A. Peña and J. L. G. Fierro, “Chemical Structures and Performance of Perovskite Oxides,” *Chemical Reviews*, vol. 101, no. 7, pp. 1981–2018, 2001.
- [50] C. H. Kim, G. Qi, K. Dahlberg, and W. Li, “Strontium-doped perovskites rival platinum catalysts for treating NO_x in simulated diesel exhaust,” *Science*, vol. 327, no. 5973, pp. 1624–1627, 2010.
- [51] A. J. Jacobson, “Materials for solid oxide fuel cells,” *Chemistry of Materials*, vol. 22, no. 3, pp. 660–674, 2009.
- [52] J. Suntivich, H. A. Gasteiger, N. Yabuuchi, H. Nakanishi, J. B. Goodenough, and Y. Shao-Horn, “Design principles for oxygen-reduction activity on perovskite oxide catalysts for fuel cells and metal-air batteries,” *Nat. Chem.*, vol. 3, no. 7, pp. 546–550, 2011.
- [53] Y. Pennec, N. J. C. Ingle, I. S. Elfimov, E. Varene, Y. Maeno, A. Damascelli, and J. V. Barth, “Cleaving-temperature dependence of layered-oxide surfaces,” *Phys. Rev. Lett.*, vol. 101, p. 216103, 2008.
- [54] B. I. Barker, S. K. Dutta, C. Lupien, P. L. McEuen, N. Kikugawa, Y. Maeno, and J. C. Davis, “STM studies of individual Ti impurity

- atoms in Sr_2RuO_4 ,” *Physica B: Condensed Matter*, vol. 329, no. 0, pp. 1334–1335, 2003.
- [55] H. Kambara, Y. Niimi, K. Takizawa, H. Yaguchi, Y. Maeno, and H. Fukuyama, “Scanning tunneling-microscopy and spectroscopy of Sr_2RuO_4 ,” *AIP conference proceedings*, vol. 850, pp. 539–540, 2006.
- [56] I. A. Firmo, S. Lederer, C. Lupien, A. P. Mackenzie, J. C. Davis, and S. A. Kivelson, “Evidence from tunneling spectroscopy for a quasi-one-dimensional origin of superconductivity in Sr_2RuO_4 ,” *Phys. Rev. B*, vol. 88, p. 134521, 2013.
- [57] J. Lee, M. P. Allan, M. A. Wang, J. Farrell, S. A. Grigera, F. Baumberger, J. C. Davis, and A. P. Mackenzie, “Heavy d-electron quasiparticle interference and real-space electronic structure of $\text{Sr}_3\text{Ru}_2\text{O}_7$,” *Nat. Phys.*, vol. 5, no. 11, pp. 800–804, 2009.
- [58] G. Li, Q. Li, M. Pan, B. Hu, C. Chen, J. Teng, Z. Diao, J. Zhang, R. Jin, and E. W. Plummer, “Atomic-scale fingerprint of Mn dopant at the surface of $\text{Sr}_3(\text{Ru}_{1-x}\text{Mn}_x)_2\text{O}_7$,” *Scientific Reports*, vol. 3, p. 2882, 2013.
- [59] T. Hanaguri, “Development of high-field STM and its application to the study on magnetically-tuned criticality in $\text{Sr}_3\text{Ru}_2\text{O}_7$,” *Journal of Physics: Conference Series*, vol. 51, no. 1, p. 514, 2006.
- [60] Y. Okada, D. Walkup, H. Lin, C. Dhital, T.-R. Chang, S. Khadka, W. Zhou, H.-T. Jeng, M. Paranjape, A. Bansil, Z. Wang, S. D. Wilson, and V. Madhavan, “Imaging the evolution of metallic states in a correlated iridate,” *Nat. Mater.*, vol. 12, no. 8, pp. 707–713, 2013.
- [61] A. Damascelli, D. H. Lu, K. M. Shen, N. P. Armitage, F. Ronning, D. L. Feng, C. Kim, Z.-X. Shen, T. Kimura, Y. Tokura, Z. Q. Mao, and Y. Maeno, “Fermi surface, surface states, and surface reconstruction in Sr_2RuO_4 ,” *Phys. Rev. Lett.*, vol. 85, pp. 5194–5197, 2000.
- [62] K. M. Shen, A. Damascelli, D. H. Lu, N. P. Armitage, F. Ronning, D. L. Feng, C. Kim, Z.-X. Shen, D. J. Singh, I. I. Mazin, S. Nakatsuji, Z. Q. Mao, Y. Maeno, T. Kimura, and Y. Tokura, “Surface electronic structure of Sr_2RuO_4 ,” *Phys. Rev. B*, vol. 64, p. R180502, 2001.

- [63] S. Y. Liu, W. T. Zhang, H. M. Weng, L. Zhao, H. Y. Liu, X. W. Jia, G. D. Liu, X. L. Dong, J. Zhang, Z. Q. Mao, C. T. Chen, Z. Y. Xu, X. Dai, Z. Fang, and X. J. Zhou, “Effect of cleaving temperature on the surface and bulk fermi surface of Sr_2RuO_4 investigated by high resolution angle-resolved photoemission,” *Chinese Physics Letters*, vol. 29, no. 6, p. 067401, 2012.
- [64] J. Redinger, F. Mittendorfer, M. Hieckel, and W. Mayr-Schmölzer, “All DFT calculations were performed by our collaborators at the Center for Computational Materials Science, Vienna University of Technology, Gußhausstraße 25-25a, A-1040 Vienna, Austria ,”
- [65] M. Setvín, C. Franchini, X. Hao, M. Schmid, A. Janotti, M. Kaltak, C. G. Van de Walle, G. Kresse, and U. Diebold, “Direct view at excess electrons in TiO_2 rutile and anatase,” *Phys. Rev. Lett.*, vol. 113, p. 086402, 2014.
- [66] R. Schaub, P. Thostrup, N. Lopez, E. Lægsgaard, I. Stensgaard, J. K. Nørskov, and F. Besenbacher, “Oxygen vacancies as active sites for water dissociation on rutile $\text{TiO}_2(110)$,” *Phys. Rev. Lett.*, vol. 87, p. 266104, 2001.
- [67] P. Scheiber, M. Fidler, O. Dulub, M. Schmid, U. Diebold, W. Hou, U. Aschauer, and A. Selloni, “(sub)surface mobility of oxygen vacancies at the TiO_2 anatase (101) surface,” *Phys. Rev. Lett.*, vol. 109, p. 136103, 2012.
- [68] O. Dulub, M. Batzilln, S. Solovev, E. Loginova, A. Alchagirov, T. E. Madey, and U. Diebold, “Electron-induced oxygen desorption from the $\text{TiO}_2(011)\text{-}2\times 1$ surface leads to self-organized vacancies,” *Science*, vol. 317, no. 5841, pp. 1052–1056, 2007.
- [69] Y. Maeno, T. Ando, Y. Mori, E. Ohmichi, S. Ikeda, S. Nishizaki, and S. Nakatsuji, “Enhancement of superconductivity of Sr_2RuO_4 to 3 K by embedded metallic microdomains,” *Phys. Rev. Lett.*, vol. 81, pp. 3765–3768, 1998.
- [70] W. Meevasana, P. D. C. King, R. H. He, S.-K. Mo, M. Hashimoto, A. Tamai, P. Songsiriritthigul, F. Baumberger, and Z.-X. Shen, “Creation

- and control of a two-dimensional electron liquid at the bare SrTiO₃ surface,” *Nat. Mater.*, vol. 10, no. 2, pp. 114–118, 2011.
- [71] Z. Wang, Z. Zhong, X. Hao, S. Gerhold, B. Stöger, M. Schmid, J. Sánchez-Barriga, A. Varykhalov, C. Franchini, K. Held, and U. Diebold, “Anisotropic two-dimensional electron gas at SrTiO₃(110),” *Proceedings of the National Academy of Sciences*, vol. 111, no. 11, pp. 3933–3937, 2014.
- [72] B. Stöger, M. Hieckel, F. Mittendorfer, Z. Wang, D. Fobes, J. Peng, Z. Mao, M. Schmid, J. Redinger, and U. Diebold, “High chemical activity of a perovskite surface: Reaction of CO with Sr₃Ru₂O₇,” *Phys. Rev. Lett.*, vol. 113, p. 116101, 2014.
- [73] E. Escalona Platero, S. Coluccia, and A. Zecchina, “Carbon monoxide and nitrogen oxide (NO) adsorption on nickel oxide (NiO): a spectroscopic investigation,” *Langmuir*, vol. 1, no. 4, pp. 407–414, 1985.
- [74] M. Setvín, U. Aschauer, P. Scheiber, Y.-F. Li, W. Hou, M. Schmid, A. Selloni, and U. Diebold, “Reaction of O₂ with Subsurface Oxygen Vacancies on TiO₂ Anatase (101),” *Science*, vol. 341, no. 6149, pp. 988–991, 2013.
- [75] G. Spoto, E. N. Gribov, G. Ricchiardi, A. Damin, D. Scarano, S. Bordiga, C. Lamberti, and A. Zecchina, “Carbon monoxide MgO from dispersed solids to single crystals: a review and new advances,” *Progress in Surface Science*, vol. 76, no. 3-5, pp. 71–146, 2004.
- [76] H. Over, M. Knapp, E. Lundgren, A. P. Seitsonen, M. Schmid, and P. Varga, “Visualization of atomic processes on ruthenium dioxide using scanning tunneling microscopy,” *ChemPhysChem*, vol. 5, no. 2, pp. 167–174, 2004.
- [77] A. Linsebigler, G. Lu, and J. T. Yates, “CO chemisorption on TiO₂(110): Oxygen vacancy site influence on CO adsorption,” *The Journal of Chemical Physics*, vol. 103, no. 21, pp. 9438–9443, 1995.

- [78] S. Azad, M. H. Engelhard, and L.-Q. Wang, “Adsorption and reaction of CO and CO₂ on oxidized and reduced SrTiO₃(100) surfaces,” *The Journal of Physical Chemistry B*, vol. 109, no. 20, pp. 10327–10331, 2005.
- [79] Z.-X. Shen, D. S. Dessau, B. O. Wells, D. M. King, W. E. Spicer, A. J. Arko, D. Marshall, L. W. Lombardo, A. Kapitulnik, P. Dickinson, S. Doniach, J. DiCarlo, T. Loeser, and C. H. Park, “Anomalously large gap anisotropy in the a-b plane of Bi₂Sr₂CaCu₂O_{8+δ},” *Phys. Rev. Lett.*, vol. 70, pp. 1553–1556, 1993.
- [80] P. A. P. Lindberg, Z.-X. Shen, W. E. Spicer, and I. Lindau, “Photoemission studies of high-temperature superconductors,” *Surface Science Reports*, vol. 11, no. 1-4, pp. 1–137, 1990.
- [81] X. L. Hu, J. Carrasco, J. Klimes, and A. Michaelides, “Trends in water monomer adsorption and dissociation on flat insulating surfaces,” *Phys. Chem. Chem. Phys.*, vol. 13, pp. 12447–12453, 2011.
- [82] J. Carrasco, F. Illas, and N. Lopez, “Dynamic ion pairs in the adsorption of isolated water molecules on alkaline-earth oxide (001) surfaces,” *Phys. Rev. Lett.*, vol. 100, p. 016101, 2008.
- [83] M. A. Henderson, “The interaction of water with solid surfaces: fundamental aspects revisited,” *Surface Science Reports*, vol. 46, no. 1-8, pp. 1–308, 2002.
- [84] A. Hodgson and S. Haq, “Water adsorption and the wetting of metal surfaces,” *Surface Science Reports*, vol. 64, no. 9, pp. 381–451, 2009.
- [85] P. A. Thiel and T. E. Madey, “The interaction of water with solid surfaces: Fundamental aspects,” *Surface Science Reports*, vol. 7, no. 6-8, pp. 211–385, 1987.
- [86] A. Fujishima and K. Honda, “Electrochemical Photolysis of Water at a Semiconductor Electrode,” *Nature*, vol. 238, no. 5358, pp. 37–38, 1972.
- [87] H.-J. Shin, J. Jung, K. Motobayashi, S. Yanagisawa, Y. Morikawa, Y. Kim, and M. Kawai, “State-selective dissociation of a single water

- molecule on an ultrathin MgO film,” *Nat. Mater.*, vol. 9, no. 5, pp. 442–447, 2010.
- [88] X. L. Hu, “First principles studies of water and ice on oxide surfaces,” *PhD thesis, University College London*, 2010.
- [89] H. Grönbeck and I. Panas, “Ab *initio* molecular dynamics calculations of H₂O on BaO(001),” *Phys. Rev. B*, vol. 77, p. 245419, 2008.
- [90] S. Maier, P. Cabrera-Sanfeliix, I. Stass, D. Sánchez-Portal, A. Arnau, and M. Salmeron, “Water-induced surface reconstruction of oxygen (2×1) covered Ru(0001),” *Phys. Rev. B*, vol. 82, p. 075421, 2010.
- [91] J. Lee, D. C. Sorescu, X. Deng, and K. D. Jordan, “Water Chain Formation on TiO₂(110),” *The Journal of Physical Chemistry Letters*, vol. 4, no. 1, pp. 53–57, 2012.
- [92] B. Meyer, D. Marx, O. Dulub, U. Diebold, M. Kunat, D. Langenberg, and C. Wöll, “Partial dissociation of water leads to stable superstructures on the surface of zinc oxide,” *Angewandte Chemie International Edition*, vol. 43, no. 48, pp. 6641–6645, 2004.
- [93] R. Włodarczyk, M. Sierka, K. Kwapien, J. Sauer, E. Carrasco, A. Aumer, J. F. Gomes, M. Sterrer, and H.-J. Freund, “Structures of the ordered water monolayer on MgO(001),” *The Journal of Physical Chemistry C*, vol. 115, no. 14, pp. 6764–6774, 2011.
- [94] J. E. Hoffman, K. McElroy, D.-H. Lee, K. M. Lang, H. Eisaki, S. Uchida, and J. C. Davis, “Imaging quasiparticle interference in Bi₂Sr₂CaCu₂O_{8+δ},” *Science*, no. 5584, pp. 1148–1151, 2002.
- [95] K. McElroy, R. W. Simmonds, J. E. Hoffman, D.-H. Lee, J. Orenstein, H. Eisaki, S. Uchida, and J. C. Davis, “Relating atomic-scale electronic phenomena to wave-like quasiparticle states in superconducting Bi₂Sr₂CaCu₂O_{8+δ},” *Nature*, vol. 422, no. 6932, pp. 592–596, 2003.
- [96] K. Fuchigami, Z. Gai, T. Z. Ward, L. F. Yin, P. C. Snijders, E. W. Plummer, and J. Shen, “Tunable metallicity of the La_{5/8}Ca_{3/8}MnO₃(001)

surface by an oxygen overlayer," *Phys. Rev. Lett.*, vol. 102, p. 066104, 2009.

CURRICULUM VITAE

BERNHARD STÖGER

PERSONAL INFORMATION

Born in Dornbirn, Austria, 25 May 1986

email stoeger.bernhard@gmail.com

EDUCATION

PhD Studies Vienna University of Technology, Vienna, Austria

2011-2014

PhD thesis: “Surface Defects and Adsorption on Strontium Ruthenates”

Supervisor: Prof. Ulrike Diebold

Undergraduate Vienna University of Technology, Vienna, Austria

Studies

2005-2011

Master thesis: “Graphene Grown on Ni(111)”

Supervisor: Prof. Ulrike Diebold

Secondary School BG Gallusstraße, Bregenz, Austria

1996-2004

PUBLICATIONS

as first author

- “Point defects at cleaved $Sr_{n+1}Ru_nO_{3n+1}(001)$ surfaces”,
Phys. Rev. B 90 (2014) 165438
- “High Chemical Activity of a Perovskite Surface: Reaction of CO with
 $Sr_3Ru_2O_7$ ”, Phys. Rev. Lett. 113 (2014) 116101

as co-author

- “Anisotropic two-dimensional electron gas at $SrTiO_3(110)$ ”,
Proc. Natl. Acad. Sci. USA 111 (2014) 3933-3937
- “Nickel Carbide as a Source of Grain Rotation in Epitaxial Graphene”,
ACS Nano 6 (2012) 3564-3572
- “Disorder and Defect Healing in Graphene on Ni(111)”,
J. Phys. Chem. Lett. 3 (2012) 136-139